Studies of the decays $D^0 \to K^{\mp}\pi^{\pm}\pi^{\pm}\pi^{\mp}$ at CLEO-c and LHCb

Tim Evans

St. Cross

University of Oxford

A thesis submitted for the degree of

Doctor of Philosophy

Trinity 2017

Studies of the decays $D^0 \to K^{\mp}\pi^{\pm}\pi^{\pm}\pi^{\mp}$ at CLEO-c and LHCb

Tim Evans

St. Cross

University of Oxford

A thesis submitted for the degree of

Doctor of Philosophy

Trinity 2017

Abstract

This thesis describes two studies of the four-body decays of the neutral charm meson, $D^0 \to K^-\pi^+\pi^+\pi^-$ and its doubly Cabibbo-suppressed counterpart $D^0 \to K^+\pi^-\pi^-\pi^+$. The first analysis is a model-independent determination of parameters that characterise the phase space averaged interference between the two amplitudes associated with each of these decay modes. The analysis exploits quantum correlations in $D\overline{D}$ pairs produced from the $\psi(3770)$ resonance in data collected with the CLEO-c detector.

The second half of this thesis describes studies of the resonant structure of these decay modes using proton-proton collision data corresponding to an integrated luminosity of $3.0\,\mathrm{fb}^{-1}$ collected by the LHCb experiment. Studies of the favoured mode, $D^0 \to K^-\pi^+\pi^+\pi^-$, are the most precise studies of the amplitude to date and this data set is one of the largest samples of any decay mode to be studied using an amplitude analysis. The study of the suppressed mode, $D^0 \to K^+\pi^-\pi^-\pi^+$, is the first study of resonance structure of this decay mode, and is also one of the few existing studies of the sub-structure of a doubly Cabibbo-suppressed amplitude. The largest contributions to both decay amplitudes are found to come from axial resonances, with decay modes $D^0 \to a_1(1260)^+K^-$ and $D^0 \to K_1(1270/1400)^+\pi^-$ being prominent in $D^0 \to K^-\pi^+\pi^+\pi^-$ and $D^0 \to K^+\pi^-\pi^-\pi^+$, respectively.

Abstract

This thesis describes two studies of the four-body decays of the neutral charm meson, $D^0 \to K^-\pi^+\pi^+\pi^-$ and its doubly Cabibbo-suppressed counterpart $D^0 \to K^+\pi^-\pi^-\pi^+$. The first analysis is a model-independent determination of parameters that characterise the phase space averaged interference between the two amplitudes associated with each of these decay modes. The analysis exploits quantum correlations in $D\overline{D}$ pairs produced from the $\psi(3770)$ resonance in data collected with the CLEO-c detector.

The second half of this thesis describes studies of the resonant structure of these decay modes using proton-proton collision data corresponding to an integrated luminosity of $3.0\,\mathrm{fb}^{-1}$ collected by the LHCb experiment. Studies of the favoured mode, $D^0 \to K^-\pi^+\pi^+\pi^-$, are the most precise studies of the amplitude to date and this data set is one of the largest samples of any decay mode to be studied using an amplitude analysis. The study of the suppressed mode, $D^0 \to K^+\pi^-\pi^-\pi^+$, is the first study of resonance structure of this decay mode, and is also one of the few existing studies of the sub-structure of a doubly Cabibbo-suppressed amplitude. The largest contributions to both decay amplitudes are found to come from axial resonances, with decay modes $D^0 \to a_1(1260)^+K^-$ and $D^0 \to K_1(1270/1400)^+\pi^-$ being prominent in $D^0 \to K^-\pi^+\pi^+\pi^-$ and $D^0 \to K^+\pi^-\pi^-\pi^+$, respectively.

Contents

1 Introduction

In 1947, Rochester and Butler observed signs of strangely long lived particles in cosmic ray experiments [1]. These long lived particles had lifetimes comparable to the π-meson, but with a mass roughly three times greater. The π-meson had been predicted by Yukawa in 1935 as the mediator of the strong interaction [2] and had also been discovered in 1947 in photographic emulsions [3]. Further study revealed an entire family of particles with peculiar properties: they could be produced by strong interactions but only in certain pairings, while given their long lifetimes it was presumed that they could only decay via the weak interaction. These observations led A. Pais and M. Gell-Mann to invent a new quantum number called *strangeness*, which was conserved in strong but not in weak interactions. Together with the isospin quantum number, introduced by W. Heisenberg and E. Wigner to explain the properties of the nucleons, strangeness formed the basis of *flavour physics*.

The first great insight provided by studying the properties of these strange particles was the solution of the so-called $\tau - \theta$ puzzle. Charged particles with an identical mass and lifetime were observed decaying to both two pions, a state that is symmetric under spatial inversion (parity), and to three pions, a state that is anti-symmetric under spatial inversion. It had been believed that the rules of the universe were entirely symmetric under spatial inversion, which would forbid a particle decaying to states with differing parity. Hence, it was presumed there were two particles, the τ and θ with differing parity but with otherwise puzzlingly identical properties. A drastic resolution to this puzzle was proposed by T.D. Lee and C.N. Yang in 1956: the τ and θ mesons are one and the same, and the weak interaction was not symmetric under parity transformations [4]. This theory was experimentally confirmed by C.S. Wu in the same year by the examination of the β-decay spectrum of polarised cobalt-60 [5]. The τ, θ are therefore truly the same particle, and together with their electrically neutral brethren became known as the kaons.

The decay rates of the different hadrons could be related by transformations between isospin and strangeness. In 1961 Gell-Mann [6] and Zweig [7] noticed that this could be explained by the hadrons being composed of combinations of three fractionally charged particles, up, down and strange, that were collectively named quarks. The quarks interact with each other via the strong-nuclear force, which at low energies is sufficiently strong that the quarks can only exist in bound states with other quarks. The integer spin mesons were identified as consisting of a quark anti-quark pair, while the half-integer spin baryons were identified as bound states of three quarks. Further possibilities, such as bound states of two quarks and two anti-quarks (tetraquarks) and four quarks and an anti-quark (pentaquarks) were also theorised. Examples of these exotic hadrons were only found relatively recently, with the first tetraquark and pentaquark identified by the Belle [8] and LHCb [9] collaborations, respectively.

Further great accomplishments in the flavour sector included the prediction in 1970 of a fourth quark, charm, to explain the suppression of certain decays of the neutral kaons by the Glashow-Illiopoulous-Maiani (GIM) mechanism [10]. The charm quark was later discovered by B. Richter and S. Ting in 1974 in a bound state with a charm anti-quark, named the J/ψ meson [11, 12]. Perhaps the most surprising discovery however was the decay of the longer lived neutral kaon into a pair of pions by J. Cronin and V. Fitch in 1964 [13], as such a process was thought to be forbidden by the symmetry that relates matter to anti-matter, known as CP-symmetry. The violation of this symmetry has profound implications for particle physics and cosmology, and remains a central area of study in modern flavour physics. The discovery of the violation of CP-symmetry led to the prediction of two additional quarks by M. Kobayashi and T. Maskawa in 1973 [14]. This extended the work of N. Cabibbo on the universality of weak interactions [15] to include a third generation of quarks such that CP-symmetry could be violated. Experimentally, the bottom quark was first found by L. Lederman in 1977 [16] with the discovery of the Υ-meson, which consisted of a bound state of the bottom quark and bottom anti-quark. The top quark was found in 1995 at the Tevatron by the

CDF and D0 collaborations [17, 18], which with a mass of about $170\,\mathrm{GeV}/c^2$ is the heaviest known particle, and decays so rapidly that it does not form bound states.

Studies of flavour phenomena successfully predicted a state over 300 times heavier than the kaon itself, and thus the potential for such measurements to indirectly probe energy scales far higher than the masses of the involved particles cannot be overstated. One such area continues to be studies of *CP*-symmetry violation, with a multitude of measurements made to over-constrain and perhaps break the current description of this phenomenon. However, an understanding of these weak effects necessitates a description of the hadronic states in which the underlying quarks find themselves bound.

This thesis describes studies of two multi-body hadronic decays of the neutral charm meson, $D^0 \to K^-\pi^+\pi^+\pi^-$ [1] and $D^0 \to K^+\pi^-\pi^-\pi^+$, and is structured as follows. Chapter 2 gives a broad theoretical introduction, with discussions on the importance of *CP*-violation to particle physics and cosmology and the relevance of the two decays that are the subject of the thesis to studies of *CP*-violating phenomena. Chapter 3 describes an analysis performed using data from the CLEO-c experiment to provide a model-independent parametrisation of hadronic effects in the $D^0 \to K^\mp\pi^\pm\pi^\pm\pi^\mp$ system. The subject of the majority of this thesis is the development of models to describe these multi-body decays. These models are constructed using data from the LHCb experiment, which is introduced in Ch. 4, while Ch. 5 describes how clean samples of the two decays are obtained. Chapter 6 introduces a formalism for describing multi-body hadronic systems known as the isobar model, and in Ch. 7 models for these two decay modes are developed and discussed.

[1] The inclusion of charge-conjugate processes is implied throughout, unless otherwise stated.

2

Theoretical Background

Contents

The Standard Model (SM) of Particle Physics provides a remarkably simple description of the interactions between an elemental set of particles and three of the fundamental forces of nature. In Sect. 2.1, these elemental particles and the fundamental forces are introduced. These fundamental forces have symmetry properties under three discrete operators. The combined effect of two of these operators, charge-conjugation (C) and parity (P), is to convert matter states into anti-matter states and vice versa. Therefore, the violation of symmetries under the *CP*-operation (*CP*-violation) is closely related to the dominance of matter over anti-matter in the early universe. The discrete symmetries, and their role in cosmology is discussed in Sect. 2.2.

Section 2.3 introduces the *CP*-violation in the quark sector, and how it originates in the mixing between mass and flavour eigenstates. This is described by the Cabibbo–Kobayashi–Maskawa (CKM) matrix, with the *CP*-violating effects described by a single complex phase. Precision measurements of the CKM matrix are therefore critical in understanding both the *CP*-violation within the Standard Model and searching for physics beyond it. The measurement of the unitarity angle γ, closely related to the *CP*-violating phase of the CKM matrix, is one of the key aims of modern flavour physics. Two methods for extracting this angle in the decays of B mesons are proposed by Gronau-London-Wyler (GLW) and Atwood-Dunietz-Soni (ADS). These are outlined in Sect. 2.4. The two decays of the neutral D-meson, $D^0 \to K^-\pi^+\pi^+\pi^-$ and $D^0 \to K^+\pi^-\pi^-\pi^+$, that are the principal concern of this thesis, play an important role in the determination of γ, and will be briefly introduced in Sect. 2.5. These two decay modes will be referred to as $D \to K\pi\pi\pi$ collectively. An extended discussion on the formalism for describing these systems is deferred to Ch. 6. Finally, the intermediate resonant states that dominate multi-body processes such as those described in this thesis will be briefly described in Sect. 2.6.

2.1 Introduction to the Standard Model

The Standard Model of particle physics provides a description of the interactions of all known fundamental particles in terms of three interactions: electromagnetic, the weak force and the strong force. The particle content of the Standard Model can be divided into two categories. The fermions, particles with half-integer spin, can be categorised in three generations, which are essentially replicas of each other with higher masses. Within each generation, there are two quarks with fractional electrical charge that also interact under the strong nuclear force, and a pair of leptons, one electrically charged and the other neutral. All of the known fermions also interact with the weak force. For each of the fermions, there is also an anti-particle partner with the same mass but opposite charges. In addition to the fermions, the bosons are integer spin excitations of the fields that describe the fundamental interactions. The photon and gluons are massless, while the bosons associated with the weak interaction gain a mass dynamically by interacting with the final piece of the Standard Model, the Higgs field. The Higgs boson is the excitation of this field, and was the last remaining particle in the Standard Model to be discovered. The particle content of the Standard Model is summarised in Fig. 2.1.

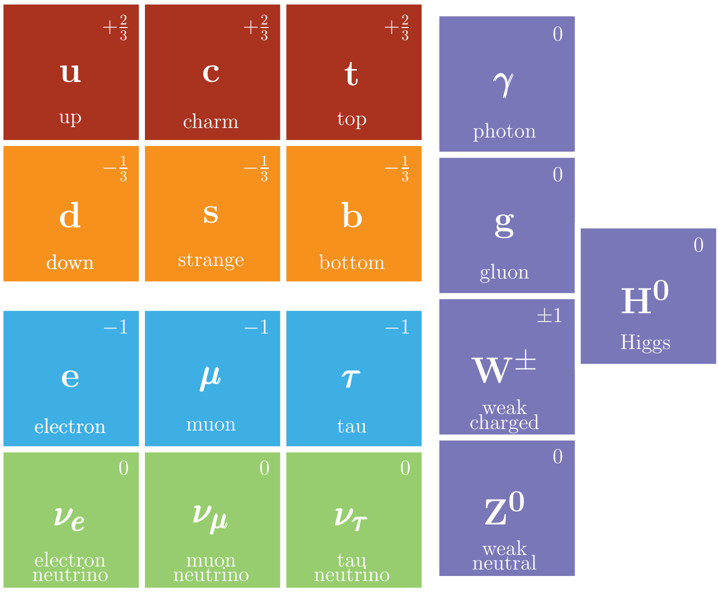

Figure 2.1: Particle content of the Standard Model, showing the three generations of fermions and gauge bosons, with the electrical charge of each of the particles inset.

2.2 *CP* violation

There are three discrete operators in the Standard Model that were long believed to be closely associated with the fundamental symmetries of nature. When applied to a single particle, these three operators are:

1. Charge-conjugation (C): Change the signs of all the additive quantum numbers of the particle. This includes the electrical charge, the quantum numbers related to both lepton and quark-flavour, and the baryon number. Charge-conjugation has the effect of transforming particles into their antiparticle partners.

2. Parity (P): Spatially inverts a particle, so a state described by $(t, \mathbf{x})$ is transformed to $(t, -\mathbf{x})$.

3. Time inversion (T): Reverses time such that $(t, \mathbf{x})$ is transformed to $(-t, \mathbf{x})$.

Any Lorentz-invariant quantum field theory should be symmetric under the combined operation CPT [19]. The eigenvalue associated with each operator is ±1, with the eigenstates therefore sometimes described as being even or odd under each operator. The electromagnetic and strong interactions are invariant under each operator individually. However, it is observed that C and P are not symmetries of weak interactions: the weak charged currents couple exclusively to left-handed fermions and right-handed anti-fermions, and hence maximally violate C and P symmetries individually. The combined CP operation transforms a left-handed fermion into a right-handed anti-fermion, and hence it may be expected that the weak interaction is CP symmetric, but this also turns out not to be the case.

Although the Standard Model provides a relatively complete description of the observed universe, there are many reasons to expect that it is incomplete. One of the most compelling reasons to expect this is the relative excess of matter over anti-matter, specifically that an excess of baryons was produced at some point in the history of the early universe. There are three independent conditions for such an excess, known as the Sakharov conditions [20], which are:

1. Baryon number violation. All known perturbative processes in the SM result in equal numbers of baryons and anti-baryons. However, there are non-perturbative electroweak processes that can produce baryons without anti-baryons [21].

2. Violation of C and CP symmetries is required even if there were a process that could generate excess baryons, as otherwise an equal and opposing process would generate an excess of anti-baryons, and hence the net baryon number of the system would not increase.

3. Baryogenesis cannot occur at thermal equilibrium, otherwise the inverse of the baryogenesis process (a process that net annihilates baryogenesis) will occur at the same rate and a net asymmetry will not be generated.

Violation of CP symmetry in weak interactions is well established in the quark sector. The known CP violation in the quark sector is about 10 orders of magnitude too small to explain baryogenesis, and therefore it is likely that this additional CP-violation originates in physics beyond the Standard Model. Therefore, precise comparisons of CP-violating observables and the predictions from the Standard Model provide an invaluable probe of new physics.

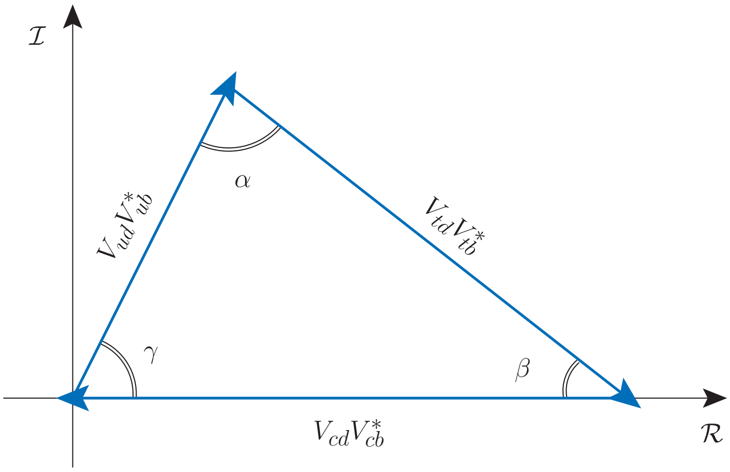

Figure 2.2: One of the unitarity triangles of the CKM matrix, showing the definition of angles α, β, γ.

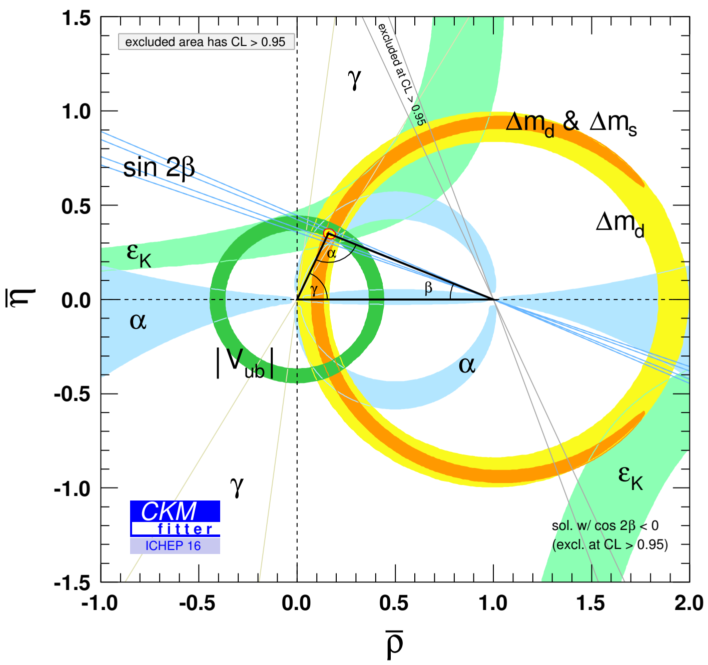

Figure 2.3: The unitarity triangle as determined by the CKMFitter collaboration, reproduced from Ref. [22]

2.3 The CKM matrix

The coupling between a particle and one of the fields is entirely prescribed by a universal coupling constant and the particle's charge with respect to that field. In the context of the weak interaction this is known as weak universality, and predicts that the coupling between the weak current and quarks should be identical between the different generations and also identical to the couplings to the different generations of leptons. This is not quite the case, as the quark mass eigenstates are not the same as the weak eigenstates. The Cabibbo-Kobayashi-Maskawa (CKM) matrix relates the weak eigenstates, (d', s', b'), with the mass eigenstates, (d, s, b), and is written as:

$$\begin{pmatrix} d' \\ s' \\ b' \end{pmatrix} = \begin{pmatrix} V_{ud} & V_{us} & V_{ub} \\ V_{cd} & V_{cs} & V_{cb} \\ V_{td} & V_{ts} & V_{tb} \end{pmatrix} \begin{pmatrix} d \\ s \\ b \end{pmatrix}. \tag{2.1}$$

In the Standard Model, weak universality implies that the CKM matrix is unitary, conversely, if the CKM matrix is not unitary it implies physics beyond the Standard Model. Formally, the interaction Lagrangian between the weak charged current, W^+ and the quark spinor states (u_i, d_i) is

$$\mathcal{L}_{\text{int}} \propto \sum_{ij} V_{ij} \bar{u}_i \gamma^\mu \left(1 - \gamma^5\right) d_j W^+_\mu, \tag{2.2}$$

where the sum is over the different quark states. The structure of this interaction is a coupling between the left-handed component of a quark field, and the spin-1 vector current of the electroweak interaction. The Lagrangian for the interaction between the anti-quarks and the weak charged current is given by the hermitian conjugate of $\mathcal{L}_{\text{int}}$. Therefore, if the elements of the CKM matrix are complex, there is the potential for *CP* violation in any process that is sensitive to the phase of a CKM matrix element. Applying the unitarity constraints allows the CKM matrix to be parametrised in terms of three mixing angles $(\theta_{12}, \theta_{23}, \theta_{13})$ and the KM phase δ, which describes the *CP*-violation:

$$V_{\text{CKM}} = \begin{pmatrix} c_{12}c_{13} & s_{12}c_{13} & s_{13}e^{-i\delta} \\ -s_{12}c_{23} - c_{12}s_{23}s_{13}e^{i\delta} & c_{12}c_{23} - s_{12}s_{23}s_{13}e^{i\delta} & s_{23}c_{13} \\ s_{12}s_{23} - c_{12}c_{23}s_{13}e^{i\delta} & -c_{12}s_{23} - s_{12}c_{23}s_{13}e^{i\delta} & c_{23}c_{13} \end{pmatrix}, \tag{2.3}$$

where $c_{ij}, s_{ij} = \cos(\theta_{ij}), \sin(\theta_{ij})$. Experimentally, it is found that the mixing between mass and weak eigenstates is relatively small in the the quark sector, therefore each of the mixing angles is small and the CKM matrix is approximately diagonal. Therefore, processes that involve off-diagonal elements of the CKM matrix, those that change the generation of the quarks are *Cabibbo-suppressed* with respect to those on the diagonal, which are referred to as *Cabibbo-favoured.*

Unitarity gives a series of constraints between the different elements of the CKM matrix that can be tested experimentally. One such constraint is:

$$V_{ud}V_{ub}^* + V_{cd}V_{cb}^* + V_{td}V_{tb}^* = 0, \tag{2.4}$$

which in the complex plane has the form of a triangle. Figure 2.2 shows a diagram of this triangle, and shows the definition of the three unitarity angles α, β and γ. The unitarity triangle can be overconstrained by performing independent measurements that are sensitive to different combinations of CKM matrix elements. An unambiguous sign of new physics would be the CKM matrix not obeying the unitarity constraints, an example of which might be that the "triangle" turns out not to be closed, with $\alpha+\beta+\gamma \neq 180^{\mathrm{o}}$. As the CKM matrix is intimately related to *CP*-violation, searches for new physics in this area are well motivated by the cosmological concerns discussed in the previous section. Figure 2.3 shows the complex plane of the unitarity constraint, with constraints on the different components of the unitarity triangle shown. The current world averages of three of the angles are:

$$\begin{aligned} \alpha &:= \arg(-V_{td}V_{tb}^*/V_{ud}V_{ub}^*) = \left(88.8^{+2.3}_{-2.3}\right)^{\mathrm{o}} \\ \beta &:= \arg(-V_{cd}V_{cb}^*/V_{td}V_{tb}^*) = \left(21.9^{+0.7}_{-0.7}\right)^{\mathrm{o}} \\ \gamma &:= \arg(-V_{ud}V_{ub}^*/V_{cd}V_{cb}^*) = \left(76.2^{+4.7}_{-5.0}\right)^{\mathrm{o}}, \end{aligned} \tag{2.5}$$

where the averages for angles β, γ are obtained by the Heavy Flavour Averaging Group (HFLAV) [23], and α by the CKM Fitter group [22]. Knowledge on α largely comes from studies of charmless decays of B mesons such as $B \to \pi\pi$ and $\rho\rho$ [24, 22]. The time-dependent *CP*-asymmetry of $B \to J/\psi K^*$ decays gives very stringent constrains on the angle β [25, 26, 27]. The least well-known angle, γ, is measured in $b \to c$ and $b \to u$ transitions [28, 29, 30], with the strongest constraints coming from the studies of *CP* asymmetries in $B \to DK$ decays, which are discussed in the following section.

2.4 Determining γ with $B \to DK$ decays

Consider the process of a charged B-hadron (B^-) decaying to a neutral charm meson (D) and a charged kaon. Two contributions to this process are shown in

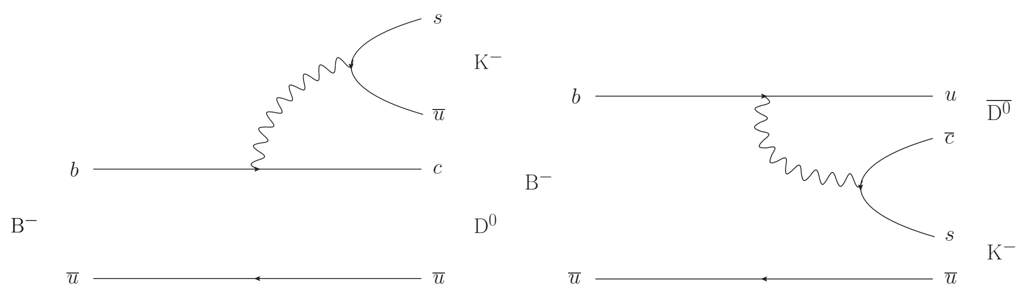

Figure 2.4: Diagrams for $B^{\mp} \to DK^{\mp}$ transitions

Fig. 2.4. As the two contributions produce D mesons of different flavours, D^0 and $\overline{D}^0$, their sum produces the superposition:

$$|D\rangle \propto |D^0\rangle + r'_B e^{i\delta_B} \frac{V_{ub}V_{cs}}{V_{cb}V_{us}} |\overline{D}^0\rangle, \tag{2.6}$$

where r'_B is the relative strong-amplitude and δ_B the *CP*-conserving strong-phase difference between the two diagrams. These parameters account for all QCD effects in the system, and must be determined experimentally. The combination of CKM matrix elements has the *CP*-violating weak-phase $-\gamma$, as *CP*-violating phases in the charm sector can be neglected. The magnitudes of the CKM matrix elements can be absorbed into the definition of r_B, leading to:

$$|D\rangle \propto |D^0\rangle + r_B e^{i(\delta_B - \gamma)} |\overline{D}^0\rangle. \tag{2.7}$$

A similar expression can be written for the *CP*-conjugate process $B^+ \to DK^+$:

$$|D\rangle \propto |\overline{D}^0\rangle + r_B e^{i(\delta_B + \gamma)} |D^0\rangle. \tag{2.8}$$

This suggests a strategy for measuring the phase γ. If the D decays to a final state that is accessible from both D^0 and $\overline{D}^0$ components of the wavefunction, the interference between these terms gives tree level access to γ. Consider a final state F of the D meson. The rates are[1]:

$$\begin{aligned}\Gamma(B^- \to D(F)K^-) &\propto \left|\langle F|D^0\rangle\right|^2 + r_B^2 \left|\langle F|\overline{D}^0\rangle\right|^2 + 2r_B \,\mathrm{Re}\left(e^{i(\delta_B-\gamma)}\langle F|D^0\rangle\langle \overline{D}^0|F\rangle\right)\\ \Gamma(B^+ \to D(F)K^+) &\propto \left|\langle F|\overline{D}^0\rangle\right|^2 + r_B^2 \left|\langle F|D^0\rangle\right|^2 + 2r_B \,\mathrm{Re}\left(e^{i(\delta_B+\gamma)}\langle F|\overline{D}^0\rangle\langle D^0|F\rangle\right).\end{aligned} \tag{2.9}$$

In principle, observables related to the two decay rates of Eq. 2.9 carry information on γ. In practice, decays involving many different choices of D-meson final states are used to provide constraints on γ. Two of the major classes of D decays considered

[1]This section neglects charm mixing as the contributions are small and the discussion is not significantly altered by including these effects.

are discussed here. In the first, proposed by Gronau, London and Wyler (GLW) [31], F is chosen to be a CP eigenstate, such as $D \to K^+K^-$. In this case, $\langle F|D^0\rangle = \langle F|\overline{D}^0\rangle$, and Eq. 2.9 simplifies to:

$$\Gamma(B^{\mp} \to D(F_{CP})K^{\mp}) \propto 1 + r_B^2 + 2r_B\cos(\delta_B \mp \gamma). \tag{2.10}$$

The sensitivity is therefore controlled by r_B, which can be roughly estimated as:

$$r_B = \underbrace{\frac{0.0035 \times 0.97344}{0.0412 \times 0.22534}}_{\hookrightarrow\ \text{CKM}} \underbrace{\frac{1}{N_c}}_{\hookrightarrow\ \text{colour}} \approx 0.12, \tag{2.11}$$

where the first term comes from the relevant combination of CKM matrix elements, and the second term is a colour factor $\frac{1}{N_c}$ that suppresses the second diagram with respect to the first. Experimentally, r_B is measured to be [28]:

$$r_B = 0.1019 \pm 0.0056.$$

Therefore, GLW modes are suppressed or favoured by up to 20% depending on the value of δ_B and γ. In a second, alternative approach proposed by Atwood, Dunietz and Soni (ADS) [32], a non-CP eigenstate is studied, and D's are reconstructed in both the F final state and the CP conjugate $\bar{F}$. The CP violation in the charm sector is small in the SM, and hence can be neglected and therefore the following relationships between amplitudes can be made

$$\begin{aligned} \mathcal{A}_F &:= \langle F|D^0\rangle = \langle \overline{F}|\overline{D}^0\rangle \\ \overline{\mathcal{A}}_F &:= \langle F|\overline{D}^0\rangle = \langle \overline{F}|D^0\rangle, \end{aligned} \tag{2.12}$$

and also the ratio of amplitudes $\mathcal{R}_F e^{-i\delta_F} = \mathcal{A}_F/\overline{\mathcal{A}}_F$ can be defined. The phase δ_F represents the relative strong-phase difference between the F final state and its CP-conjugate. The four rates can be written in terms of these parameters as

$$\begin{aligned} \Gamma(B^- \to D(F)K^-) &\propto \mathcal{R}_F^2 + r_B^2 + 2r_B\mathcal{R}_F\cos(\delta_B - \gamma - \delta_F) \\ \Gamma(B^- \to D(\overline{F})K^-) &\propto 1 + r_B^2\mathcal{R}_F^2 + 2r_B\overline{R}_F\cos(\delta_B - \gamma + \delta_F) \\ \Gamma(B^+ \to D(F)K^+) &\propto 1 + r_B^2\mathcal{R}_F^2 + 2r_B\mathcal{R}_F\cos(\delta_B + \gamma + \delta_F) \\ \Gamma(B^+ \to D(\overline{F})K^+) &\propto \mathcal{R}_F^2 + r_B^2 + 2r_B\mathcal{R}_F\cos(\delta_B + \gamma - \delta_F). \end{aligned} \tag{2.13}$$

Consider the case where F is a doubly Cabibbo-suppressed process. For example, $F = K^+\pi^-$. In this case, the ratio of amplitudes is roughly $\left|\frac{V_{us}V_{cd}}{V_{cs}V_{ud}}\right| = 0.05$. The contributions to the opposite sign observables, $\Gamma(B^{\mp} \to D(K^{\pm}\pi^{\mp})K^{\mp})$, are all of a similar order, and hence large asymmetries can be generated.

This formalism can be generalised to multi-body final states of the D meson [33]. The amplitudes $\mathcal{A}_F$ and $\overline{\mathcal{A}}_F$ are then functions of position ($\mathbf{x}$) in the phase space of the multi-body system. The phase space can be averaged over by introducing the coherence factor, R_F, and average relative strong phase, δ_F:

$$R_F e^{-i\delta_F} = \langle \mathcal{A}_F \overline{\mathcal{A}}_F^* \rangle = \frac{\int d\mathbf{x} \mathcal{A}_F(\mathbf{x}) \overline{\mathcal{A}}_F^*(\mathbf{x})}{A_F A_{\bar{F}}}, \tag{2.14}$$

where A_F / $A_{\bar{F}}$ are the phase-space averaged amplitudes, given by

$$A_F^2 = \int d\mathbf{x} \left| \mathcal{A}_F(\mathbf{x}) \right|^2. \tag{2.15}$$

It is also useful to define the ratio of phase-space averaged amplitudes, $r_F = A_F / A_{\bar{F}}$. Collectively, these parameters are referred to as the hadronic and coherence parameters of the D decay. The coherence factor lies between 0 and 1, depending on the differences between the amplitude and its CP conjugate. A high coherence factor implies there is a roughly constant strong-phase difference between the amplitudes, whereas averaging over large variations in strong-phase differences will result in a lower coherence factor. The integrated decay rate can be written in terms of these parameters as

$$\Gamma(B^{\mp} \to DK^{\mp}) \propto r_F^2 + r_B^2 + 2 r_B r_F R_F \cos(\delta_B \mp \gamma - \delta_F). \tag{2.16}$$

The coherence factor dilutes the interference term, and hence the sensitivity to γ. A small coherence factor results in sub-optimal sensitivity to γ, as a wide range of strong-phase differences are averaged over. It is therefore useful to consider small regions of phase space in which the variation in the difference in strong phases is smaller between the two amplitudes. This allows the measurement to exploit knowledge of these local phase differences in order to improve sensitivity. In particular, these smaller regions of phase space will have differing values of the average strong-phase difference, δ_F, which is extremely powerful in reducing ambiguities due to the trigonometric dependence of decay rates on the unitarity angle γ.

The expressions discussed in this section have a dependence on many nuisance parameters as well as the weak phase γ. Those from the decay of the B-meson, r_B and δ_B, can be overconstrained by combining measurements from many different decays of the D meson. This can be seen in Fig. 2.5, which shows the profile likelihood in the two-dimensional plane of γ vs. r_B [30]. There are other nuisance parameters that are specific to the decays of the D meson, r_F, R_F and δ_F and hence require external inputs. Central to this thesis is the measurement and modelling of these for one multi-body decay of the D meson, $D \to K\pi\pi\pi$.

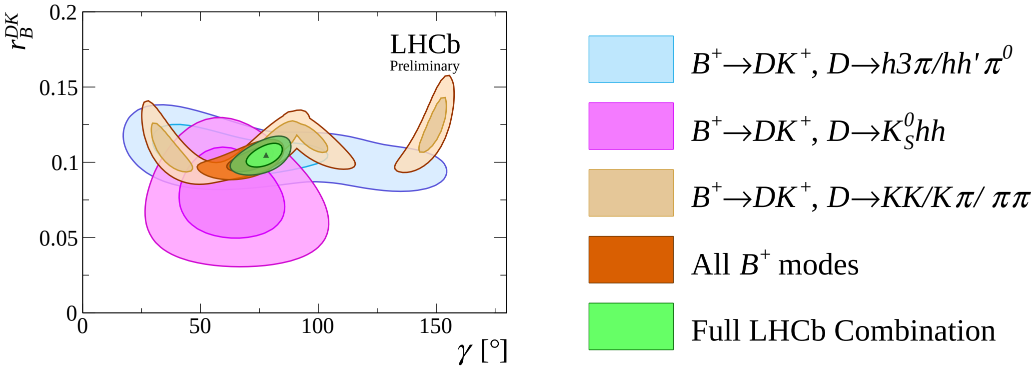

Figure 2.5: Likelihood contours for γ vs. r_B, showing the contributions from $B \to DK$ decays, split by the different D-meson final states. The dark and light regions indicate 68.3% and 95.5% confidence levels respectively. Reproduced from Ref. [30].

2.5 The decays $D^0 \to K^{\pm}\pi^{\mp}\pi^{\mp}\pi^{\pm}$

The decays $D^0 \to K^-\pi^+\pi^+\pi^-$ and $D^0 \to K^+\pi^-\pi^-\pi^+$ have an important role to play in improving knowledge of the unitarity angle γ. The approach to such an analysis so far has considered the D-meson phase space inclusively. As discussed in Sect. 2.4, further sensitivity can be gained by exploiting variations in the behaviour of observables across the phase space of the D-decay. The inclusive approach has also been taken to studies of charm mixing in these decays, which can also benefit from an understanding of how the amplitudes vary locally across the four-body phase space. The decay modes are also a rich laboratory for examining the behaviour of the strong interaction at low energy, through studies of the make-up and nature of the intermediate resonances that contribute to the final states.

These considerations motivate the construction of models that describe the quantum mechanical amplitude associated with each decay as a function of position in the phase-space of the final state particles. Such a study is known as an *amplitude analysis*. This section will give a broad overview of the two decay modes, with an extended discussion on the formalism for describing the amplitude deferred until Ch. 6.

The main diagrams at the level of weak transitions that contribute to $D^0 \to K^{\mp}\pi^{\pm}\pi^{\pm}\pi^{\mp}$ decays are shown in Fig. 2.6. The transitions relevant for $D^0 \to K^-\pi^+\pi^+\pi^-$ decays are shown in Fig. 2.6(a) (b), with the latter diagram colour favoured with respect to the former, and hence should play a more important role in determining the total amplitude. As these diagrams involve the favoured transitions of the weak currents, those within the same generation, the decay $D^0 \to K^-\pi^+\pi^+\pi^-$

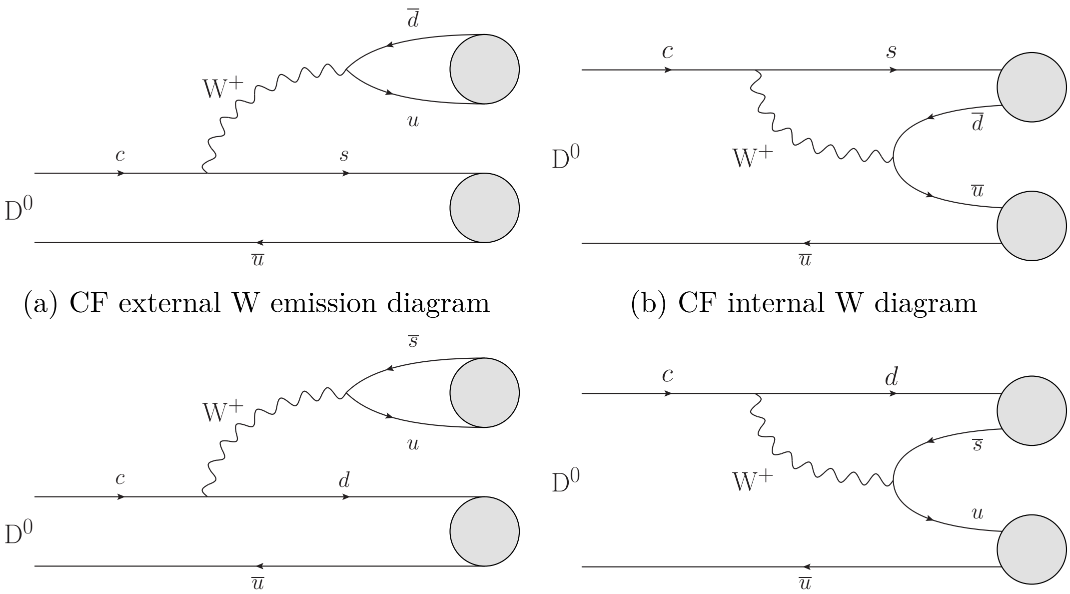

(a) CF external W emission diagram

(b) CF internal W diagram

(c) DCS external W emission diagram

(d) DCS internal W diagram

Figure 2.6: Weak-level diagrams for charm to strange and charm to anti-strange transitions

is referred to as Cabibbo-favoured (CF). The weak-level diagrams that contribute to $D^0 \to K^+\pi^-\pi^-\pi^+$ decays are shown in Fig. 2.6(c) 2.6(d). Both processes involve two off-diagonal elements of the CKM matrix, which are significantly suppressed compared to the charged weak currents with coupling amongst the same generation, and therefore are described as doubly Cabibbo-suppressed (DCS). The ratio of rates of the doubly-Cabibbo suppressed process to the favoured process is roughly

$$\frac{|V_{cd}V_{us}|^2}{|V_{cs}V_{ud}|^2} \approx 3 \times 10^{-3}. \tag{2.17}$$

A smaller contribution to $D^0 \to K^+\pi^-\pi^-\pi^+$ decays comes from charm mixing. During the lifetime of the D^0-meson, there is an amplitude associated with it oscillating into a $\overline{D}^0$ meson. The $\overline{D}^0$ meson can access the $K^+\pi^-\pi^-\pi^+$ final state via the Cabibbo-favoured transition. The total amplitude will therefore always contain a mixing component. However, this will typically be a sub-dominant contribution to the total amplitude as mixing only plays a small role in the charm sector. The mixing contribution will therefore be neglected unless explicitly discussed.

Multi-body processes will typically occur via a sequence of intermediate resonant states. For example, the $s\overline{d}$ quark state in Fig. 2.6(b) may hadronise to an excited state of the kaon, the K^{*0} meson, while the $u\overline{u}$ quark state may become an excited state of the pion, the ρ^0 meson. The four-body final state is then produced by the rapid decay of these resonances into pions and kaons. In this example, the decay chain is[2]

$$D^0 \to \underbrace{\overline{K}^{*0}}_{\to K^-\pi^+}\underbrace{\rho^0}_{\to \pi^+\pi^-}.$$

The DCS decay has a contribution from the $D^0 \to K^{*0}[K^+\pi^-]\rho^0[\pi^+\pi^-]$ decay chain, the weak diagram for which is shown in Fig. 2.6(d). Due to the similarity of the two internal W diagrams, it may be expected that the relative contributions from these neutral resonances to the final state produced via this topology may be comparable between CF and DCS amplitudes. The similarity can be contrasted with the diagrams involving an external W emission which are shown in Fig. 2.6(a)/ 2.6(c). The $u\overline{d}/s\overline{u}$ state can produce a quasi-stable meson, a charged pion and kaon in the CF and DCS cases respectively, while the other state must decay to three bodies in order to make up the charged four-body final state. An example decay chain is

$$D^0 \to \underbrace{a_1(1260)^+}_{\to \rho^0\pi^+ \to \pi^+\pi^-\pi^+} K^-,$$

where the $a_1(1260)$-meson has been produced by the charged-weak current. In the DCS case, the charged weak current produces a $u\overline{s}$ quark state, and hence will produce a kaon or a kaon resonance. Therefore, it may be expected that the charged kaon-like and charged pion-like resonances will have interchanged roles in CF and DCS amplitudes.

The many possible configurations of the final state must be considered in describing a multi-body system. Consider a final state involving N on mass-shell spinless particles. This system has a phase space with $3N$ degrees of freedom. Three degrees of freedom can be removed by an arbitrary boost. A further three degrees of freedom can be removed via an arbitrary rotation, on the condition that the total decay process is rotationally invariant. This property holds for a spinless particle decaying to N spinless particles, but not in generality if either the

[2]It is useful to have a compact notation for these decay chains. The convention adopted in this thesis is for square brackets to indicate the decay products of a given resonance, so the above example is written as

$$D^0 \to \overline{K}^{*0}\left[K^-\pi^+\right]\rho^0\left[\pi^+\pi^-\right]$$

initial or final state particles have intrinsic spin. One further degree of freedom is then removed by requiring that the parent is also on-shell. The dimensionality of the N body phase-space is therefore:

$$d = 3N - 6 - 1. \tag{2.18}$$

The best known examples of multi-body systems are the three body decays. In this case, there are two degrees of freedom. The phase-space density is constant when describing the space in terms of a pair of invariant masses, leading to the well known Dalitz plot. Four-body final states have five degrees of freedom, and the phase-space density is not flat in any choice of coordinates.

2.6 Light resonances

The multi-body processes that are described in the latter half of this thesis are expected to have dominant contributions from intermediate resonant states. These intermediate hadronic resonances rapidly decay to combinations of the quasi-stable ground state hadrons. For the decays considered in this thesis, there are contributions from the relatively light resonances containing u, d, s-quarks. These resonances have isospin $0, 1/2, 1$, with $I = 0$ and $I = 1$ resonances sometimes referred to as isoscalars and isovectors respectively. Figures 2.7 and 2.8 show the mass spectrum and spin-parity of the $I = 1, I = 1/2$ systems up to about $2\,\mathrm{GeV}/c^2$. A quasi-classical description of the meson is of a bound state of a quark (q) and an anti-quark ($\overline{q}$). The physical meson states will generally be superpositions of quark states that have the same quantum numbers. This section gives a brief introduction to this description, with a focus on those resonances which are potentially relevant to $D \to K\pi\pi\pi$ decays.

The spectrum of meson excitations can be described by the relativistic quark model of Godfrey and Isgur [35]. This model considers the degrees of freedom of a bound state of a fermion anti-fermion pair:

1. The spins of the fermions can either be aligned or anti-aligned, hence there is a quantum number associated with the total spin S, that takes values $0, 1$.

2. The two fermions can also have relative orbital angular momentum $L = 0, 1, 2..$, which can be partially inferred by measuring the intrinsic parity of the resonance, which is related to the orbital angular momentum via $P = (-1)^{L+1}$.

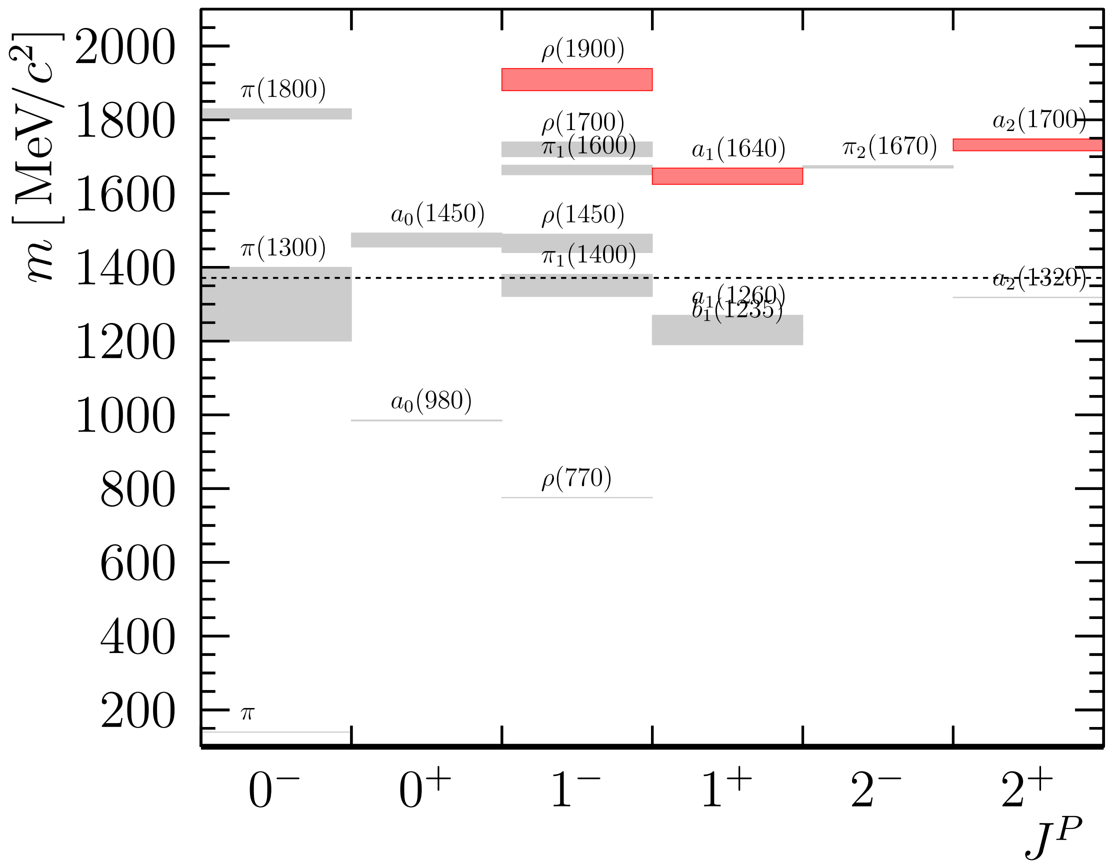

Figure 2.7: The low mass spectrum of the $I = 1$ system up to the tensors. The dashed line shows the maximum energy of the three pion system in $D \to K\pi\pi\pi$ decays. Bands show the uncertainties on masses from Ref. [34].

3. The spin and orbital angular momentum combine to form the total angular momentum J, which can take values from $|L - S|$ to $L + S$. Of the quantum-numbers pertaining to the spin-orbit configuration of the two quarks, only the total angular momentum can be directly observed.

4. The two fermions can also be radially excited, which is denoted by the quantum number N. A radial excitation is distinguished from states with the same spin-orbit configuration by being of higher mass. The radially excited mesons are also often referred to as the radial recurrences of a given state.

In spectroscopic notation, these quantum numbers are written as

$$N^{2S+1}L_J.$$

The lowest energy configuration of the $q\bar{q}$ system therefore has $J = L = S = 0$, and hence has odd parity and is thus referred to as a pseudo-scalar, or 1^1S_0 in

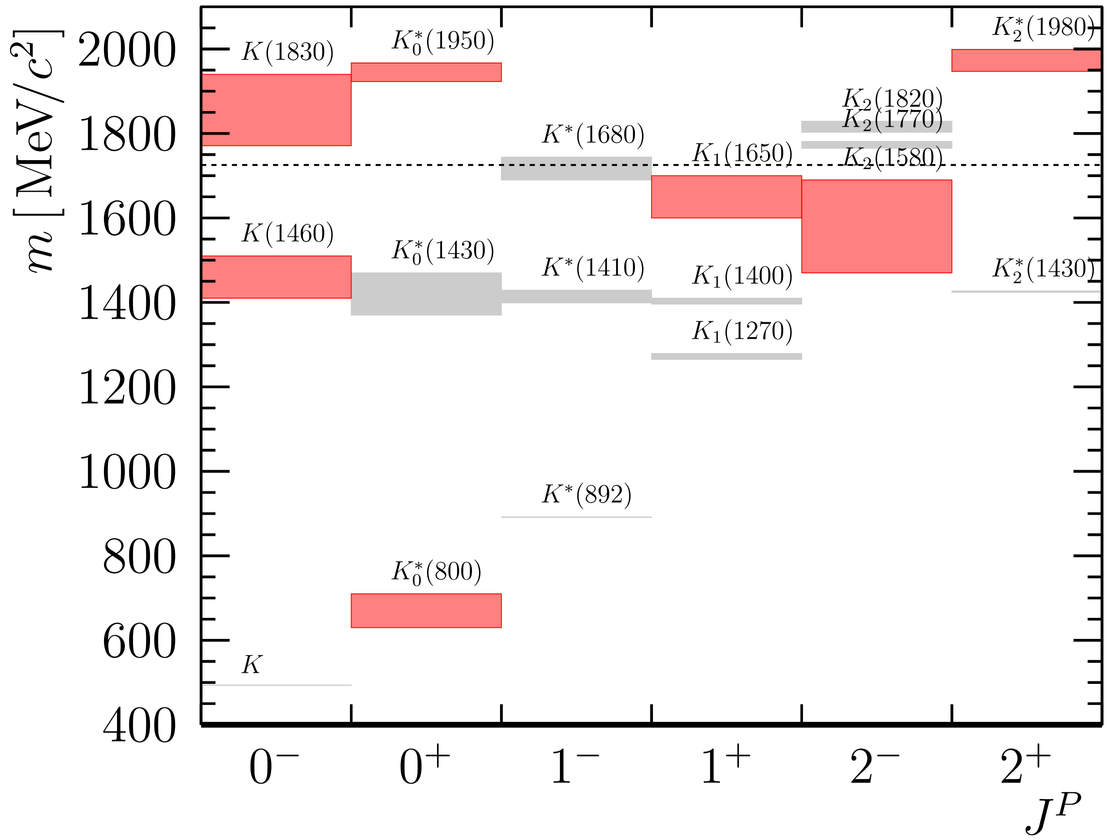

Figure 2.8: The low mass spectrum of the $I = 1/2$ system up to the tensors. The dashed line shows the maximum energy of the $K\pi\pi$ system in $D \to K\pi\pi\pi$ decays. Bands show the uncertainties on the masses of resonances from Ref. [34], with red boxes indicating resonances that are not well established.

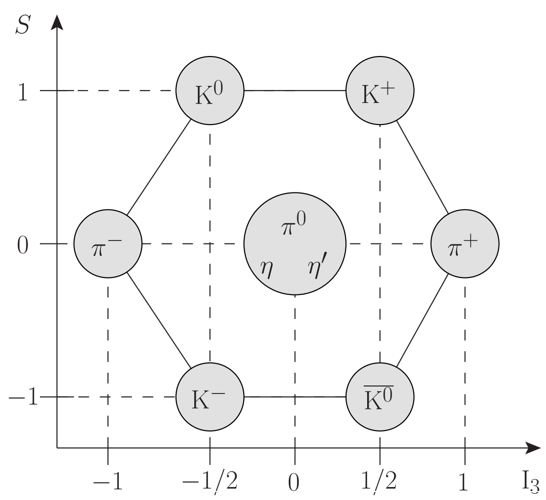

Figure 2.9: The ground state pseudo-scalar mesons with the associated strangeness and isospin quantum numbers.

spectroscopic notation. As this is the ground state of the diquark, these mesons are the quasi-stable particles, such as the lowest mass pions and kaons. The ground states with their isospin and strangeness quantum numbers are shown in Fig. 2.9.

$\mathbf{S = 1, L = 0}$

The meson excitations that are best understood are those associated with aligning the spins of the two fermions, but with the other quantum numbers as in their ground states, or 1^3S_1 in spectroscopic notation. As such, these states form an excited multiplet that has $J = 1$ and are parity odd, and therefore are known as the vector mesons. These are also sometimes referred to as being states of *natural* parity. Well-known resonances such as the $\rho(770)$ and $K^*(892)$ populate this multiplet, and have been extensively studied with precision measurements of masses, widths and couplings. These lowest energy vector resonances will occasionally be referred to without explicitly stating their masses, so $\rho(770) \to \rho$ and $K^*(892) \to K^*$.

$\mathbf{L = 1}$

If the two fermions have the lowest excitation of orbital angular momentum, $L = 1$, they must also have $+1$ intrinsic parity. It might be expected that the lowest mass parity-even states should therefore be 1^1P_1, and be an axial vector (1^+) state; contrasting with the vector mesons, these are sometimes referred to as being of *unnatural* parity. The axial vector mesons can be distinguished from the vector mesons by considering the minimum number of quasi-stable decay products. From the requirement to simultaneously conserve angular momentum and parity in the strong decays, the axial vector mesons must decay to a minimum of three final-state particles, while the vector mesons have a minimum of two final-state particles. The axial vectors therefore do not play a role in describing the usual three-body Dalitz plots, as these only involve resonances that can decay to two final-state particles. The axial vectors are also not produced in the $2 \to 2$ scattering processes that provide input for the understanding of the natural parity states. The majority of the information about these resonances has therefore historically come from studies of diffractive processes such as $\pi p \to p\pi\pi\pi$. The axial resonances play a critical role in describing the amplitudes associated with the four-body processes described in the latter half of this thesis, and hence these final states provide an excellent laboratory for studying these resonant states that are usually experimentally difficult to access.

The association between the quark states and the physical mesons is more complicated for the axial-vector resonances than for the vector resonances, as the

1^3P_1 quark states also manifest themselves as axial-vectors, and thus the quark state associated with a meson cannot be uniquely identified using only spin parity. This relationship can sometimes be inferred from how the different states act under charge-conjugation, or C-parity. The associated eigenvalue, λ_C, is a good quantum number for the quark and meson states that are electrically neutral and do not carry strangeness, with the eigenvalue given by $\lambda_C = (-1)^{L+S}$ under these conditions. As C-parity is a conserved quantity in strong interactions, additional information on the quark states of a decaying meson can be inferred from its decay channels. It is useful to generalise the C-parity to states that carry electrical charge: $\mathcal{G}$-parity is defined such that the different states within an isospin multiplet have the same $\mathcal{G}$-parity as each other, and equal to the C-parity of the state within the multiplet for which this is a good quantum number. For example, the isovector ground-state multiplet consists of (π^+, π^0, π^-), in which the π^0-meson has a well defined C-parity with eigenvalue $\lambda_C = +1$, and thus the multiplet has $\lambda_{\mathcal{G}} = +1$. Considerations of $\mathcal{G}$-parity are thus equivalent to considerations of C-parity on the electrically neutral member of an isospin multiplet, and then applying isospin symmetry to the result to describe its electrically charged partners. The quantum numbers of the 1^+ isovectors, the $b_1(1235)$ and the $a_1(1260)$, can be inferred using $\mathcal{G}$-parity. The $a_1(1260)$ decays predominately to $\rho\pi$, a state with odd $\mathcal{G}$-parity, implying $a_1(1260)$ has odd $\mathcal{G}$ parity, and hence immediately may be identified as the 1^3P_1 quark state. The $b_1(1235)$ decays predominately to $\omega\pi$ ($\lambda_{\mathcal{G}} = +1$) and hence is inferred to have even $\mathcal{G}$-parity, and therefore is identified with the 1^1P_1 quark state.

In contrast to the axial isovector states, the 1^1P_1 and 1^3P_1 excitations of the kaon do not have well-defined $\mathcal{G}$-parity as the electrically neutral members of the multiplets do not have well-defined C-parity. Therefore, there is no quantum number that distinguishes the states and thus they can mix to produce the physical meson states, the $K_1(1270)$ and $K_1(1400)$. The mixing can be parametrised in terms of a mixing angle θ_K, with the mass eigenstates written in terms of the quark eigenstates as

$$\begin{aligned} |K_1(1400)\rangle &= \cos(\theta_K)|^3P_1\rangle - \sin(\theta_K)|^1P_1\rangle \\ |K_1(1270)\rangle &= \sin(\theta_K)|^3P_1\rangle + \cos(\theta_K)|^1P_1\rangle. \end{aligned} \tag{2.19}$$

This mixing turns out to be almost maximal, with $\theta_K = \left(33^{+6}_{-2}\right)^{\mathrm{o}}$ reported by Ref. [36], and has important consequences for both four-body charm decays discussed in this thesis.

There are two other possible spin-orbit configurations of a quark state with $L = 1, S = 1$. The first are the (0^+) scalar states, which have an anti-aligned spin and orbit. These states minimally decay to two particles and can be produced in $2 \to 2$ scattering processes. For both $I = 0$ and $I = 1/2$ scalar sectors, unique identification of the resonant content of each system is made difficult by resonances with large widths and significant non-resonant scattering amplitudes that also contribute to all final states with the same quantum numbers. The first scalar excitation of the pion, the $a_0(980)$, is forbidden from decaying to two (or three) pions by $\mathcal{G}$-parity conservation, and therefore does not play a role in describing $D \to K^-\pi^+\pi^+\pi^-$ decays. Four-body decays do not provide particularly useful additional insight into the scalar sector, as these resonances can also be produced in scattering experiments and play a role in three-body amplitude analyses. In particular, three-body decays will often have a unique production mechanism for a given scalar state, which is a significant advantage compared to the multiple production mechanisms that are present in the four-body decays.

The other configuration of $L = 1, S = 1$ has the spin-orbits aligned, and hence these states are (2^+) tensors. As these states have natural parity they can be studied in both scattering processes and three-body decays, and therefore are relatively well understood, with examples of states with this spin-parity including the isoscalar excitation $f_2(1270)$ and the kaon excitation $K_2^*(1430)$. The tensor resonances play a relatively minor role in $D \to K\pi\pi\pi$ decays due to the relatively small phase-space available.

$\mathbf{N = 2, L = 0, S = 0}$

The excitations of exclusively the radial quantum number are written as 2^1S_0 in spectroscopic notation. They have the same spin-orbit configuration as the ground state and manifest as pseudo-scalar (0^-) resonances with higher masses than the ground state particles. The strong decays of these resonances have a minimal three-body final state due to the requirement of conserving parity in strong decays, and therefore have some of the same experimental difficulties as the axial vectors. Evidence for resonances with these quantum numbers historically comes from diffractive processes such as $\pi^-p \to p\pi\pi\pi^-$, which established the $\pi(1300)$-meson and identified it as the first radial excitation of the pion [37]. Despite being well-established, the mass, width and couplings of this state are not well known. The diffractive process $K^-p \to K^-\pi^+\pi^-p$ also shows some evidence for a radial excitation of the kaon, the $K(1460)$ [38, 39]. This resonance requires experimental confirmation as it has not yet been observed to be produced by mechanisms other than the original diffractive process. Four-body decays can also produce these resonances, via a different mechanism to the diffractive process, and hence can provide useful additional knowledge.

There are also resonances that have multiple quantum numbers excited. The best understood examples of these are the radial excitations of the vector states, the 2^1P_1 resonances. These have the same quantum-numbers as the vector ground state, but have larger masses and much broader widths. Examples of these include the $\rho(1450)$ and $K^*(1410)$ for the $\rho(770)$ and $K^*(892)$. These states are more complicated than the vector ground states, as they typically have enough energy available to decay to multiple final states. For example, the $K^*(1410)$-meson has been observed decaying to both $K\pi$ and $K\pi\pi$ final states. As these resonances are at higher masses, it may be expected that they should play only a minor role in the relatively low-energy regime of $D \to K\pi\pi\pi$ decays.

3

Determination of $D \to K^-\pi^+\pi^+\pi^-$ coherence factor and associated hadronic parameters at CLEO-c

Contents

As outlined in Sect. 2.4, knowledge of the variations in the amplitude and phase differences between Cabibbo favoured and suppressed amplitudes for the process $D \to K\pi\pi\pi$ is essential for extracting the unitarity angle γ in $B \to DK$ decays. By averaging over the entire four body phase-space, the dependence can be expressed in terms of a set of parameters that can be measured experimentally. The definitions of these parameters, and their relevance to $B \to DK$ transitions have been outlined in the previous chapter. This chapter describes a measurement of these parameters, exploiting quantum-correlations in the decays of the $\psi(3770)$ resonance. Section 3.1 introduces the observables at this resonance that can be used to constrain the hadronic parameters of charm decays. The analysis presented in this chapter exploits the copious production of the $\psi(3770)$ resonance at the Cornell Electron Storage Ring (CESR), the decays of which were measured by the CLEO-c experiment. These are briefly described in Sect. 3.2. Section 3.3 describes the extraction of various yields from the CLEO-c data-set, with the construction of the quantum-correlated observables from these yields discussed in Sect. 3.4.1. The methods for selecting candidates, the determination of various sources of background contamination and normalisation of the yields are based on previous analyses of this channel [40, 41], with the analysis presented in this thesis improving on these previous studies by the inclusion of additional final states and utilising an updated simulation to improve estimates of various sources of background. The constraints from these observables are combined with additional constraints from a charm mixing study performed by the LHCb collaboration [42] to provide a global fit to the coherence factor and the associated hadronic parameters. This is described in Sect. 3.5.

The analysis described in this Chapter was published in Ref. [43].

3.1 Quantum-correlated observables

The hadronic parameters essentially depend on the interference between Cabibbo favoured and suppressed amplitudes, and as such can be accessed experimentally in processes where both amplitudes contribute in a known way. Generically, this involves studying the decays of a D-meson that is in a known superposition of the flavour eigenstates. One such system is neutral charm mesons that are produced via $c\bar{c}$ resonances such as the $\psi(3770)$, as the decays of these resonances result in

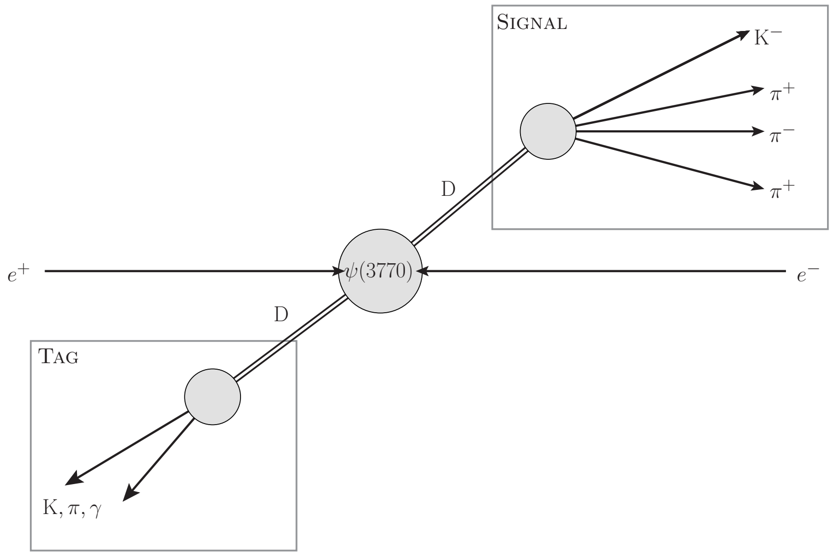

Figure 3.1: Schematic of the double-tag reconstruction of $e^+e^- \to \psi(3770) \to D\overline{D}$. The signal side of the decay is typically $K^-\pi^+\pi^+\pi^-$, while a variety of tags are reconstructed.

mesons that are quantum-mechanically entangled. Information about the flavour wavefunction can therefore be inferred by reconstructing both D-mesons. This is shown schematically in Fig. 3.1 for a $\psi(3770)$-resonance produced via an electron-positron collision. The *signal* side of the decay in the current analysis will typically be $K^-\pi^+\pi^+\pi^-$, but the following discussion will generally refer to it as F as it is often useful to reconstruct other signal decays as a normalisation channel. The *tag* side of the decay is reconstructed in a variety of final states, generically referred to as G, and provides a probe of the wavefunction of the signal decay. This is referred to as the *double-tag* method, as both neutral charm mesons from the decay of the $\psi(3770)$ resonance are reconstructed.

In order to determine how the inclusive rate of a given double-tag, $\Gamma(F|G)$, depends on the hadronic parameters of the $K^-\pi^+\pi^+\pi^-$ system, the wave function that describes the entangled $D\overline{D}$ system must first be considered. As the $\psi(3770)$ resonance is a $J^{PC} = 1^{--}$ state, the wavefunction that describes the two D-mesons must be odd under charge conjugation. This implies that the entangled state of the D-mesons can be described by the anti-symmetric wavefunction:

$$|\psi\rangle = \frac{1}{\sqrt{2}}\left(|D^0\rangle|\overline{D}^0\rangle - |\overline{D}^0\rangle|D^0\rangle\right). \tag{3.1}$$

This immediately gives an expression for the double-tag rate in terms of the coherence factors and associated hadronic parameters that are defined in Eq. 2.14. In terms of these parameters, the rate is given by

$$\Gamma_{FG} = |\langle FG|\psi\rangle|^2 = \Gamma_0 A_{\bar{F}}^2 A_{\bar{G}}^2 \left(r_F^2 + r_G^2 - 2R_F R_G r_F r_G \cos(\delta_G - \delta_F)\right), \tag{3.2}$$

Table 3.1: D-meson final-states considered in this analysis.

Type	Final state
Flavour specific	$K^-\pi^+$, $K^-\pi^+\pi^+\pi^-$, $K^-\pi^+\pi^0$
CP even	K^-K^+, $\pi^-\pi^+$, $K^0_S\pi^0\pi^0$, $K^0_L\pi^0$, $K^0_L\omega$, $\pi^+\pi^-\pi^0$
CP odd	$K^0_S\pi^0$, $K^0_S\omega$, $K^0_S\phi$, $K^0_S\eta$, $K^0_S\eta'$
Self conjugate	$K^0_S\pi^+\pi^-$

where Γ_0 is an overall normalisation that is independent of the tags considered. The parameters (r, δ, R) are the average amplitude ratio, average strong phase difference and coherence factor for each decay mode, and are defined in Eq. 2.14. It is more straightforward to construct the ratio of the measured yield to the expected yield under the no quantum-correlations hypothesis for most of the tags considered. These are referred to as the ρ set of observables, and can be written as:

$$\rho^F_G = 1 - \frac{2R_F R_G r_F r_G \cos(\delta_G - \delta_F)}{r_F^2 + r_G^2}, \tag{3.3}$$

which by definition are unity in the absence of quantum-correlations $(R_F, R_G = 0)$.

The double-tag decay rates are largely free of mixing effects due to the quantum entanglement of the two D mesons. However, mixing plays a non-negligible role in determining the ρ-observables as the expected rate in the absence of quantum-correlations is affected by charm mixing, and as such Eq. 3.3 is inexact. Full expressions for the observables including mixing effects can be found in Ref. [40]. These corrections are used in the final determination of the hadronic parameters, but do not significantly alter the discussion and hence are neglected in the following text.

For the remainder of this section, the various different classes of double tags that are reconstructed and their dependence on the coherence factor and associated hadronic parameters will be discussed. A complete list of the final states that are reconstructed is given in Table 3.1.

3.1.1 *CP* eigenstates

Consider reconstruction of a CP eigenstate such as $D^0 \to K^-K^+$ or $D^0 \to K^0_L\pi^0$ as the tag G. The coherence factor and ratio of average amplitudes for the CP eigenstate are 1, and the average strong-phase difference is 0 or 180° depending on whether the state is CP even or odd. Therefore, the ρ observable is

$$\rho^F_{CP} = 1 - \lambda \frac{2R_F r_F \cos(\delta_F)}{1 + r_F^2}, \tag{3.4}$$

where λ is the *CP* eigenvalue of the tag. The rate is maximally altered when the coherence is 1 and there is no strong-phase difference. In this case, the double tag rates are altered by $\approx \mp 2r_F$ due to quantum correlations. The amplitude ratio r_F is of a doubly Cabibbo-suppressed process to a Cabibbo-favoured process. Hence r_F is approximately given by $\tan^2(\theta_c) \approx 0.05$, and the rates can be altered by up to $\approx 10\%$ by quantum correlations. It is useful to also define the *CP*-even observable

$$\Delta^F_{CP} = \lambda \left(\rho^F_{CP} - 1\right), \tag{3.5}$$

which allows the *CP*-even and *CP*-odd tags to be combined. In addition to the decays that are either *CP*-even or *CP*-odd, the decay $D \to \pi^+\pi^-\pi^0$ has both a dominant *CP*-even contribution and a small contamination from *CP*-odd amplitudes. For a general state that includes *CP*-even fraction F^G_+ and *CP*-odd fraction F^G_-, the ρ observable can be written as

$$\rho^F_{CP} = 1 - (F^G_+ - F^G_-)\frac{2R_F r_F \cos(\delta_F)}{1 + r_F^2}. \tag{3.6}$$

3.1.2 Flavour specific tags

Three flavour specific double-tags are considered, $K^-\pi^+\pi^+\pi^-$, $K^-\pi^+$ and $K^-\pi^+\pi^0$. For each double-tag, the charged kaons can either have the same or opposite charges. Therefore, there is a *like-sign* double-tag, which in general has high sensitivity to quantum correlations, and an *opposite-sign* double-tag which has very low sensitivity, and therefore provides a useful normalisation channel. The tags considered are:

1. $K\pi\pi\pi$ vs $K\pi\pi\pi$. In this case, the like-sign ρ observable is given by

$$\rho_{K3\pi} = 1 - R^2_{K3\pi}, \tag{3.7}$$

and hence quantum correlations can have a large effect on the rate when the two decay modes have high coherence. The opposite-sign ρ-observable is

$$\rho^{OS}_{K3\pi} = 1 - \frac{2r^2_{K3\pi}}{1 + r^4_{K3\pi}} R^2_{K3\pi} \cos\left(2\delta_{K3\pi}\right). \tag{3.8}$$

Therefore, as $r^2_{K3\pi} \approx 3 \times 10^{-3}$, quantum correlations have a negligible effect on the opposite sign yield. This is generally true of the opposite sign yields, and hence they can be used for normalisation purposes.

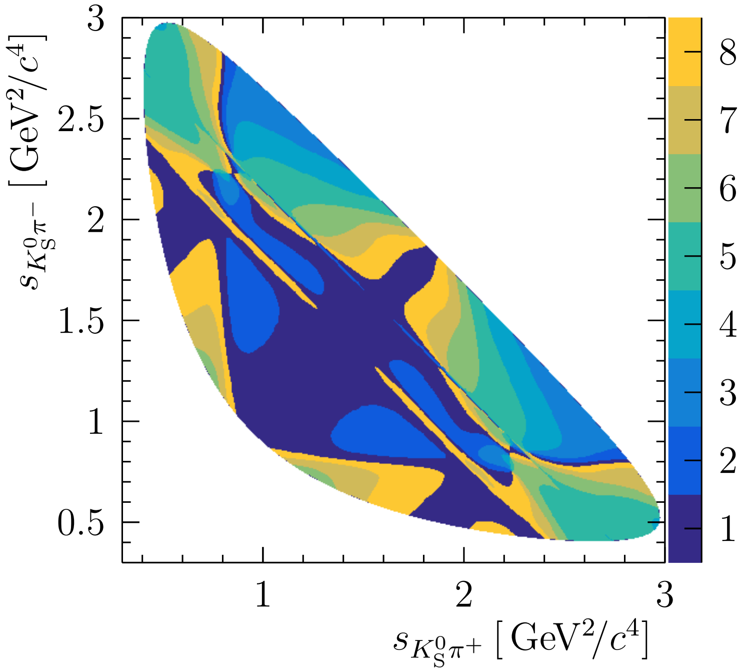

Figure 3.2: Equal average strong-phase difference binning for $D^0 \to K_S^0\pi^+\pi^-$ decays, reproduced from Ref. [45]. The colour scale indicates the absolute bin number as a function $s_{K_S^0\pi^+} : s_{K_S^0\pi^-}$ of the invariant mass-squared combinations of the K_S^0 meson with each charged pion.

2. $K\pi\pi\pi$ vs $K\pi$. The like-sign ρ observables are given by:

$$\rho_{K\pi} = 1 - \frac{2r_{K3\pi}r_{K\pi}R_{K3\pi}\cos(\delta_{K3\pi} - \delta_{K\pi})}{r_{K\pi}^2 + r_{K3\pi}^2}, \tag{3.9}$$

where the hadronic parameters for the $D \to K\pi$ decay can be taken from charm mixing measurements and dedicated quantum-correlated studies [44].

3. $K\pi\pi\pi$ vs $K\pi\pi^0$. The like-sign ρ observable is given by

$$\rho_{K\pi\pi^0} = 1 - 2\frac{r_{K3\pi}r_{K\pi\pi^0}}{r_{K3\pi}^2 + r_{K\pi\pi^0}^2}R_{K3\pi}R_{K\pi\pi^0}\cos(\delta_{K3\pi} - \delta_{K\pi\pi^0}). \tag{3.10}$$

In the current analysis the coherence factor and average relative strong-phase difference of the $K\pi\pi^0$ final state are determined simultaneously with those for the $K\pi\pi\pi$ state, taking the double-tag yields for $K\pi\pi^0$ vs CP, $K\pi$ and $K_S^0\pi\pi$ tags from Ref. [41] to provide constraints on these parameters.

3.1.3 $K_S^0\pi^+\pi^-$

The decay $D \to K_S^0\pi^+\pi^-$ has been extensively studied due to its important role in determining the unitarity angle γ, in particular both model-dependent and independent studies have been performed of the amplitude and strong phase-differences between $D^0 \to K^0_S\pi^+\pi^-$ and $\overline{D}^0 \to K^0_S\pi^+\pi^-$ amplitudes across the Dalitz plot [46, 45]. This local knowledge makes this a very useful tag mode, as the double-tag yields can be examined as a function of position in the $D \to K^0_S\pi\pi$ phase space. In practice, the double-tag yields are studied in bins of the $D \to K^0_S\pi\pi$ phase space. The binning scheme is inspired by the amplitude model for this mode developed by the BaBar collaboration in Ref. [46], and follows the scheme in Ref. [45] to give 16 bins of equal strong-phase differences between $D^0 \to K^0_S\pi^+\pi^-$ and $\overline{D}^0 \to K^0_S\pi^+\pi^-$ amplitudes. A binned method is used as a model independent determination of the hadronic properties of the $D \to K^0_S\pi\pi$ decay from Ref. [45] can then be used.

As this is a three-body decay, the amplitude can be described in terms of a pair of coordinates, the invariant mass-squared combinations $s_+ = s_{K^0_S\pi^+}$ and $s_- = s_{K^0_S\pi^-}$ by convention. The amplitude is related to its *CP*-conjugate via,

$$\mathcal{A}_{D^0}(s_+, s_-) = \mathcal{A}_{\overline{D}^0}(s_-, s_+), \tag{3.11}$$

and therefore the average strong-phase differences and binning are anti-symmetric about the $s^+ = s^-$ plane. The binning is shown in Fig. 3.2 by the Dalitz-plot of $s_+ : s_-$, where the entry at each position is the absolute bin-number. By convention, bins above the $s_+ = s_-$ plane are given negative bin numbers, while those below positive. The total rate for the D^0 decay in the ith bin is therefore equal to the rate into the -ith bin in the $\overline{D}^0$ decay, and hence this decay mode is sometimes referred to as *self conjugate*. The average strong-phase differences in each bin are parametrised using the c_i, s_i parameters, defined by:

$$c_i - is_i = \left(\sqrt{K_i K_{-i}}\right)^{-1} \int_i d\mathbf{x} \mathcal{A}_{D^0}\mathcal{A}^*_{\overline{D}^0}, \tag{3.12}$$

where the phase-space integral is over the ith bin, and K_i is the amplitude integrated over this bin. The c_i, s_i parameters can be considered as the amplitude-weighted averages of the cosine and sine of the average strong-phase difference between the two amplitudes, while the K_i parameter is the fractional yield of flavour-specific decays into the ith bin. The expected double-tag yield in the ith bin can then be expressed in terms of these parameters and the hadronic parameters of the $D \to K\pi\pi\pi$ system as

$$Y_i = H_{K3\pi}\left(K_i + \left(r^{K3\pi}\right)^2 K_{-i} - 2r^{K3\pi}\sqrt{K_i K_{-i}} R_{K3\pi}\left(c_i \cos(\delta_{K3\pi}) - s_i \sin(\delta_{K3\pi})\right)\right), \tag{3.13}$$

where $H_{K3\pi}$ is an overall normalisation constant.

3.2 The CLEO experiment

The CLEO-c detector was the final stage of the CLEO detector on the Cornell Electron Storage Ring (CESR) accelerator in New York. The CLEO experiment ran for almost thirty years between 1979 and 2008, with the CLEO-c detector taking data between 2003 and 2008. In the earlier years of the experiment, the accelerator ran at a centre-of-mass energy at and around the Υ-resonances to produce B mesons. The final phase of the experiment was focused on charm physics, producing charm mesons from the $c\bar{c}$ resonances. The analysis presented in this thesis exploits the data taken at the $\psi(3770)$-resonance, which is closest to the open-charm threshold and produces charm-meson pairs in a quantum-mechanically entangled state. This section gives a very brief introduction to CESR and CLEO, with Ref. [47] providing a detailed description of these systems.

3.2.1 The Cornell Electron Storage Ring

The Cornell Electron Storage Ring (CESR) was an electron-positron accelerator in Ithaca, New York, consisting of three systems. Electrons and positrons were accelerated from a linear accelerator to an inner 10 GeV synchrotron. This then fed the electron storage ring, which provided electron-positron collisions with a centre-of-mass energy between 3 and 10 GeV at the CLEO-c detector. During CLEO-c operations, the centre-of-mass energy of collisions was reduced in the synchrotron using wiggler magnets. Electron-positron collisions at a centre-of-mass energy of about 4 GeV result in copious production of the charmonium resonances, which can then be exploited to make measurements of the quantum-correlated observables discussed in the previous section.

3.2.2 The CLEO-c detector

The CLEO-c detector was designed to be close to hermetic, with a coverage up to about 20° from the beam line. A schematic diagram showing the different sub-systems of the detector is shown in Fig. 3.3. The CLEO-c tracking system consisted of a pair of cylindrical drift chambers inside a 1T magnetic field parallel to the beam direction, provided by a superconducting solenoid magnet. The inner drift chamber replaced the silicon vertex detector of CLEO-III, and was instrumented from about $4 \to 12$ cm with a gas wire detector. The outer gas drift chamber covered

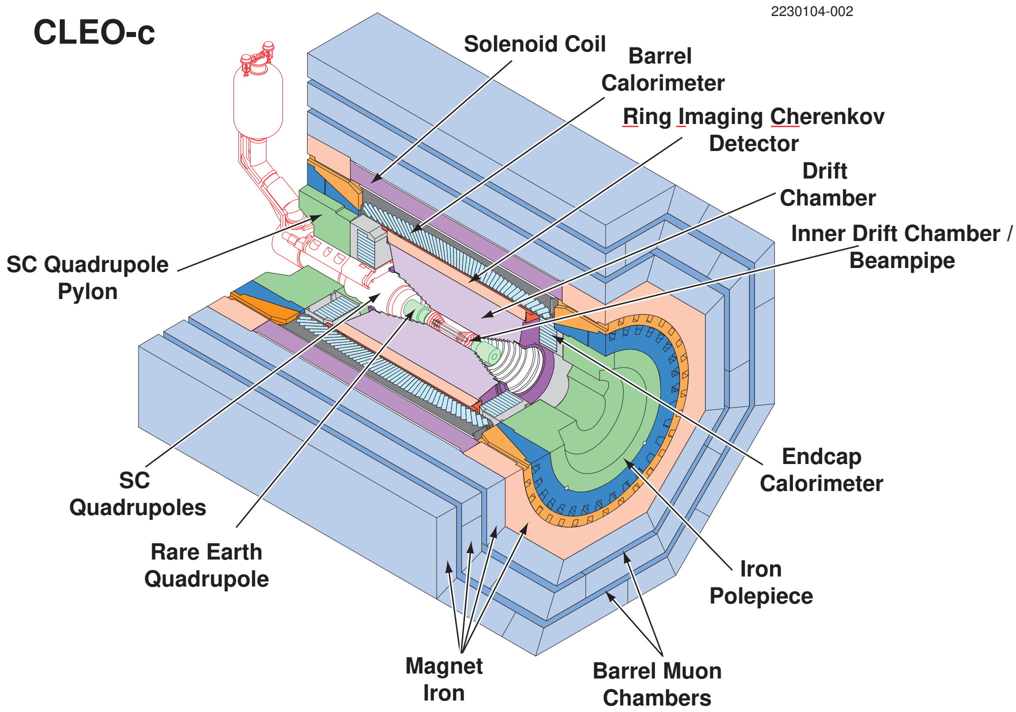

Figure 3.3: Schematic of the CLEO-c detector.

from about $12 \to 82$ cm radially from the interaction point. Each drift chamber consisted of about 1 cm square cells with an instrumented inner wire at a potential of 2.1kV with respect to eight outer wires. As charm mesons are produced with low momentum due to the relatively low Q-value of $\psi(3770)$ decays, the D-meson decay vertices cannot typically be resolved using the vertex detector. A source of background is therefore due to events where the tracks from the two D mesons are swapped. The vertex system however provides powerful discrimination between K^0_S mesons, from which a secondary vertex can normally be identified, and pion pairs directly produced by the decay of a D meson.

Charged particle identification was provided by several different sub-detectors. Firstly, the drift chambers provide some measurement of the ionisation per unit length of a track. This can be used to infer its velocity via the Bethe-Bloch formula. This provided good separation between kaons and pions up to about 0.6 GeV/c. Above this energy, separation was provided by a Ring Imaging CHerenkov (RICH) detector, positioned outside of the tracking system, which achieved excellent separation of different charged particle species at higher energies. Separation of kaons and pions is critical for identifying different charge combinations of $D \to K\pi\pi\pi$ decays.

Table 3.2: Summary of the CLEO-c data samples taken at the $\psi(3770)$ resonance with the integrated luminosity of each of the data sets.

Dataset	Integrated luminosity [pb^{-1}]
31	19.1
32	30.5
33	6.2
35	47.7
36	68.6
37	109.3
43	116.6
44	174.0
45	108.2
46	137.1
Total	818.3

Measurement of the energy of electromagnetic showers was provided by a Crystal Calorimeter (CC). The calorimeter consisted of 7,800 caesium iodide scintillating crystals. For the analysis presented in this chapter, several tags rely on the reconstruction of π^0 and η mesons. The resultant photons from the decays of these mesons are reconstructed by clustering the energy deposits in adjacent cells of the calorimeter. A key variable in identifying the electromagnetic shower from a photon is the ratio of the total energy in the 3×3 cells around the central cell of a cluster to the energy deposited in the 5×5 cells about a cluster, which is known as the E9/E25 variable. An electromagnetic shower is considered to be well identified as coming from a photon if 99% of the energy of the shower is deposited in the inner 9 cells.

3.2.3 Data samples

The analysis described in this thesis exploits the full CLEO-c data sample taken at $\sqrt{s} = 3.770\,\mathrm{GeV}/c^2$ with a total integrated luminosity of $818.3 \pm 8\,\mathrm{pb}^{-1}$. This consists of six samples taken between the years 2003 and 2005, and a second larger set of four samples taken between 2006 and 2007. The production cross-section of the $\psi(3770)$ resonance at this energy is about 6.3 nb [48]. Approximately 50% of $\psi(3770)$ resonances decay to pairs of neutral charm mesons, and hence about five million $D^0\overline{D}^0$ pairs were produced. The data samples used are summarised in Table. 3.2.

3.2.4 Simulation

There are two different types of simulation used in the following analysis. Specific samples are generated with only certain decays of interest. These are used to compute the efficiencies of some double-tags, and in some cases to make corrections to the yields. Large samples are also generated using all known production and decay channels in order to assess contributions from peaking backgrounds. Both types of sample are generated and processed in the same way, with the underlying e^+e^- interaction and decays of resultant particles handled by the EvtGen package [49]. The interaction between these decay products and the detector is then simulated using the GEANT3 package [50]. The simulated events are then digitised and passed through the same analysis chain as real data.

3.3 Yield determination

This section describes the determination of the yields of the different doubly-tagged final states introduced in Sect. 3.1, with a complete list of these final states given in Table 3.1. The selection requirements on these different final states are discussed, followed by the method for estimating the residual contamination from various sources of background. Finally, the yields for the different double-tags are given in Sect. 3.3.3.

3.3.1 Selection

The D-meson candidates that are then combined in a double tag are centrally reconstructed according to a common set of selection criteria. Additional selection criteria are applied to the two D-meson candidates that constitute the double-tag, and are as follows:

- Mode specific requirements are placed on the energy difference, ΔE, the difference between the total energy of the particles composing the D candidate and the energy of each beam. The window applied in this variable depends on the energy resolution of the mode required, so modes that have neutral particles will generally require a broader window than those only including charged tracks. Examples of this are shown in Fig. 3.4, which compares the distributions for the tags $K\pi\pi\pi$ and $K^0_S\pi^0\pi^0$. The ΔE requirements for each of the decay modes considered are detailed in Table 3.3.

Table 3.3: Criteria on the energy difference, ΔE, for the different fully reconstructed tags

	ΔE [MeV] Min.	Max.
$K\pi\pi\pi$	-20.0	20.0
$K\pi$	-29.4	29.4
KK	-20.0	20.0
$\pi\pi$	-30.0	30.0
$K^0_S\pi^0$	-71.0	45.0
$K^0_S\eta$	-55.0	35.0
$K^0_S\phi$	-18.0	18.0
$K^0_S\omega$	-25.0	25.0
$K^0_S\pi^0\pi^0$	-55.0	45.0
$K^0_S\eta'$	-30.0	20.0
$\pi\pi\pi^0$	-58.3	35.0

Table 3.4: Criteria on the invariant mass of intermediate particle candidates, and the final states used to reconstruct these particles.

	Final state	Mass [MeV/c^2] Min.	Max.
K^0_S	$\pi^+\pi^-$	490.1	505.1
ω	$\pi^+\pi^-\pi^0$	762.0	802.0
η	$\gamma\gamma$	506.0	590.0
η	$\pi^+\pi^-\pi^0$	506.0	590.0
ϕ	K^-K^+	1009.0	1033.0
η'	$\eta\pi^+\pi^-$	950.0	964.0

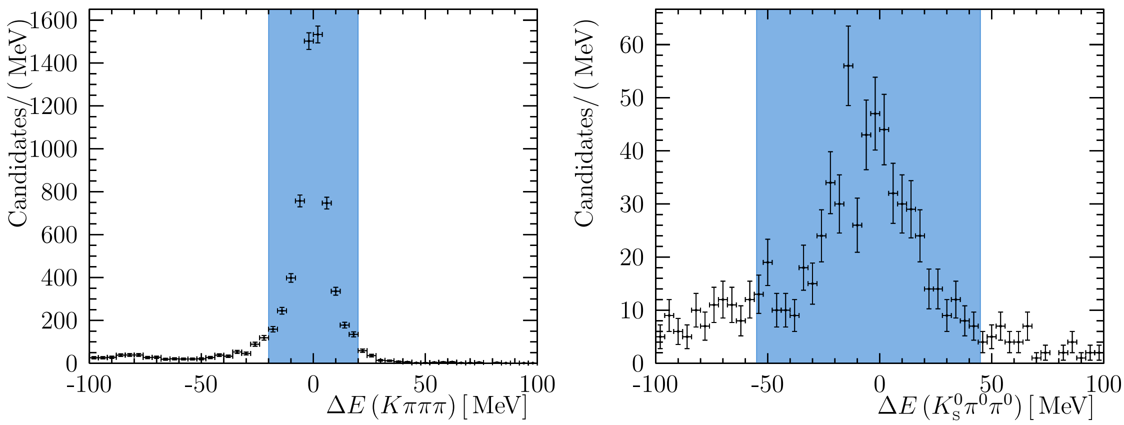

Figure 3.4: Energy difference distribution for the tags $K\pi\pi\pi$ and $K^0_S\pi^0\pi^0$, showing a considerably broader distribution in the latter due to the presence of neutral particles in the final state. The filled region indicates the requirements placed on ΔE for each tag.

- The electromagnetic showers from π^0, η candidates must both satisfy the E9/E25 criteria described in Sect. 3.2.2.

- Short lived intermediate resonances such as ϕ or ω have windows placed on the total invariant mass of their constituent particles. The size of this window is indicative of the mass resolution rather than the physical width of these states and is listed for the different resonances in Table 3.4. For tags that reconstructed the η'-meson, the resultant η-meson is only reconstructed in the $\gamma\gamma$ final state.

- The K^0_S-meson candidates are required to have travelled a significant distance from the e^+e^- vertex, with a flight significance of greater than two. The invariant mass of the dipion system must also be within 7.5 MeV/c^2 of the nominal K^0_S mass.
- Pairs of pions that originate from K^0_S mesons that are misidentified as coming directly from a D meson are a considerable source of peaking background for many of the double tags considered. This background is reduced for these tags by requiring that if a secondary vertex is constructed from dipions that fall within 7.5 MeV/c^2 of the nominal K^0_S-mass, it has a flight significance of less than 2.
- The relatively high Q-value of the decay mode $D \to K^-\pi^+$ means that either of the daughters can be outside of the geometrical acceptance of the RICH detector. Hence, at least one of the daughters is required to be within the acceptance.

Only a small percentage of K^0_L mesons decay within the fiducial volume of the detector, hence rather than fully reconstructing these modes, the constrained kinematics of electron-positron machines are instead exploited in order to reconstruct these tags. These tags are susceptible to significant contamination from partially reconstructed backgrounds, and therefore additional requirements are placed on these tags. Firstly, events that contain any additional charged tracks or neutral particle candidates that are not a part of either of the single tags are vetoed. This is critical in removing background from tags that would leave additional tracks in the detector, such as $K^0_S\pi^0$, but are otherwise identical to the tag. Additional requirements are placed on the kinematics of the visible decay products of the two partially reconstructed tags.

3.3.2 Background subtraction

Fully reconstructed tags

The number of signal candidates for the fully reconstructed modes is determined using a two-dimensional sideband subtraction technique in the plane consisting of the two beam constrained masses of the D-meson candidates. This two-dimensional plane is shown in Fig. 3.5 for the $D \to K^-\pi^+\pi^+\pi^-$ opposite sign double-tag. Four different regions are defined in this two-dimensional plane, with each region giving a handle on either the signal or a different source of background.

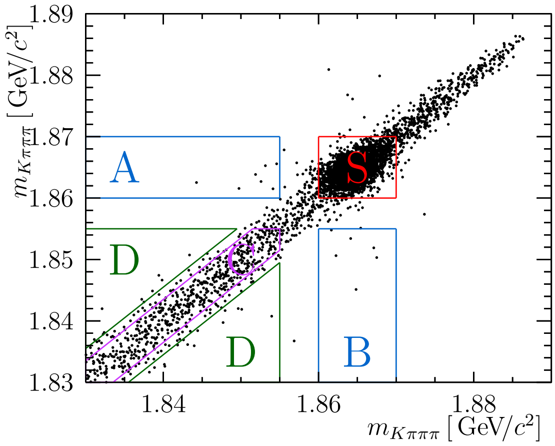

Figure 3.5: The invariant mass of one D-meson candidate against the mass of the other candidate for the $D \to K^-\pi^+\pi^+\pi^-$ opposite sign double-tag. In each case the invariant mass is calculated using constraints from the beam energy.

1. Signal (S): The signal box is where both D mesons are close to the nominal D-meson mass ($1.86 \to 1.87\,\mathrm{GeV}/c^2$). The signal yield is defined by the number of signal candidates in this region.

2. Partially reconstructed (A,B): One D meson is correctly reconstructed but the other is not, for example one of the decay products may be mis-identified or an additional decay product such as a π^0 may be missed in the reconstruction.

3. Track swapped (C): Neither of the D mesons is correctly reconstructed but the total final state particle content does originate in a true $\psi(3770)$ decay, thus the invariant masses of the two D-meson candidates are correlated, and appear on the diagonal of the plane.

4. Flat (D): Neither of the D mesons is correctly reconstructed, and the total particle content is not from a true $\psi(3770)$ decay, and hence this background is flat on the mass plane. This source of background covers the entire plane, not just this region, and therefore is subtracted from the other regions before determining the yield of a given background.

The signal yield is determined by subtracting the various sources of backgrounds inferred from the yields within the different sideband regions from the yield within the signal box. Small additional corrections are applied to correct for limitations in this technique for several of the tags, and are described in Ref. [40]. For example, there is some spillover of signal candidates in the tags $K^0_\mathrm{S}\pi^0\pi^0$, $K^0_\mathrm{S}\eta$ into the low mass sideband, and hence small additional factors are taken from

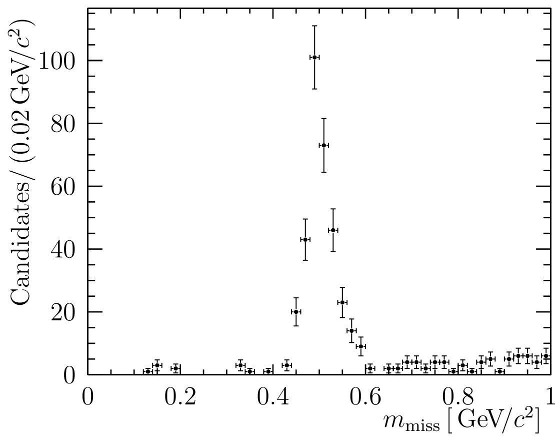

Figure 3.6: Missing mass distribution for the $K^0_{\mathrm{L}}\omega$ tag, showing a clear peak at the nominal kaon mass with a width of about 30 MeV/c.

simulation in order to correct for this effect. The details of these additional corrections do not alter the discussion, and are included within the calculation of the background subtracted yields.

Partially reconstructed tags

Two tags containing K^0_{L} mesons are utilised in this analysis, $K^0_{\mathrm{L}}\omega$ and $K^0_{\mathrm{L}}\pi^0$, however only a few percent of K^0_{L} mesons will decay inside the fiducial acceptance of the detector. Therefore, knowledge of the initial electron-positron state is used to exploit these tags without attempting to reconstruct any detector signal from the K^0_{L} meson. The missing mass, m_{miss}, is constructed from the four-momenta of the visible signals in the detector that is part of the double-tag and the known kinematics of the initial electron-positron state. Double tags that are correctly reconstructed with only a K^0_{L} missed will therefore be peaked in missing mass about the nominal mass of the K^0_{L} meson, while various sources of background will have other shapes in the missing-mass distribution. The distributions of the different sources of double-tag candidates in missing mass are taken from simulated events, with sidebands then used to determine the overall yields of the various components in order to subtract background from the signal region. The missing mass distribution for the $K^0_{\mathrm{L}}\omega$ tag is shown in data in Fig. 3.6, which shows a clean peak about the nominal kaon mass with remarkably low background contamination and a relatively narrow width of about 30 MeV/c^2.

Peaking backgrounds

In addition to the flat backgrounds, there are several sources of peaking background. The yield of this contamination within the signal region is determined using large samples of simulated events. The largest source of peaking background is from decays that contain a K^0_S, the decay products of which have been incorrectly identified as coming from one of the D mesons. This is particularly problematic for the low yield like-sign flavour tags: $K^-\pi^+$, $K^-\pi^+\pi^+\pi^-$ and $K^-\pi^+\pi^0$, as the decay $D^0 \to K^0_S K^-\pi^+$ is a singly Cabibbo-suppressed process and yields final state particles with the same charge-configuration as the signal. Therefore, without accounting for quantum correlations, events involving this decay will have a rate of roughly $20\times$ that of the correctly reconstructed double tag. This source of background is suppressed by the K^0_S veto described in Sect. 3.3. The residual contamination from this background, as well as other sources of peaking background, is estimated from simulation.

3.3.3 Yield results

The yields for the double tags where the signal decay is $D \to K^-\pi^+\pi^+\pi^-$ are shown in Table 3.5. Background contributions are estimated using the sidebands of the two-dimensional beam-constrained mass distribution and large samples of simulated events. The largest source of peaking background in the like-sign tags is from $D^0 \to K^0_S K^\mp\pi^\pm$ decays, where the $K^0_S \to \pi^+\pi^-$ vertex has not been reconstructed. The peaking background yields are taken from simulation, with corrections applied for quantum correlations where relevant. In order to reduce systematic uncertainties in the interpretation, the double-tag yields of most of the *CP*-tagged modes are normalised by the yield of $K^-\pi^+$ vs. the *CP*-tag. The details of this normalisation procedure are given in Sect. 3.4.1. The procedure for selecting $K^-\pi^+$ vs tag events and subtracting backgrounds are equivalent to those for the $K^-\pi^+\pi^+\pi^-$ double-tags, and the yields for these double-tags are presented in Table 3.6.

Yields of $D \to K^0_S\pi^+\pi^-$ tag

The $K^-\pi^+\pi^+\pi^-$ vs $K^0_S\pi^+\pi^-$ double-tag is considered in bins of the $K^0_S\pi^+\pi^-$ phase-space, with the binning described in Sect. 3.1.3. A kinematic fit is applied to the $K^0_S\pi^+\pi^-$ final state to constrain the D-meson candidate mass to its true value,

Table 3.5: Yields for tags vs $K^-\pi^+\pi^+\pi^-$, showing estimates for signal and background yields in the signal region. Raw refers to the unsubtracted number of events within the signal region. The peaking background estimates are taken from simulation and are corrected for quantum correlations. Signal refers to the background-subtracted signal yield, with additional small corrections applied to some tags to account for limitations of the background subtraction method, and the quoted uncertainties are statistical only.

		Background		
	Raw	Flat	Peaked	Signal
$K^+\pi^-\pi^-\pi^+$	4210	125.2	51.9	4006.3 ± 65.0
$K^-\pi^+\pi^+\pi^-$	37	3.5	13.5	19.7 ± 6.2
$K^+\pi^-$	5259	42.2	13.1	5203.7 ± 72.7
$K^-\pi^+$	38	0	11.4	26.6 ± 6.2
$K^+\pi^-\pi^0$	10866	208	60	$10\,598 \pm 104.8$
$K^-\pi^+\pi^0$	81	3.5	24.4	53.1 ± 9.1
$\pi^+\pi^-$	250	5.2	0.6	244.2 ± 15.9
K^+K^-	546	5.9	0	542 ± 23.4
$K^0_S\pi^0$	719	9.6	8.1	701.3 ± 26.9
$K^0_S\omega$	386	8.8	35.6	340.7 ± 19.8
$K^0_S\pi^0\pi^0$	316	22.2	4.9	299.5 ± 18.3
$K^0_S\phi$	63	0.6	4.9	57.5 ± 8.0
$K^0_S\eta\,[\gamma\gamma]$	143	5.6	2.6	135 ± 12.1
$K^0_S\eta\,[\pi^+\pi^-\pi^0]$	49	3.5	8	37.5 ± 7.2
$K^0_S\eta'\,[\eta\pi^+\pi^-]$	41	0	0.9	40.1 ± 6.4
$K^0_L\pi^0$	891	31.9	28.6	839.4 ± 30.6
$K^0_L\omega$	329	5.3	22.3	302.8 ± 19.0
$\pi^+\pi^-\pi^0$	1355	40.5	34.5	1280 ± 37.2

allowing the momenta of the D-meson decay product to vary within according to their uncertainties. This improves the resolution of the Dalitz plot, and hence mitigates the effect of events migrating to a different bin due to resolution effects to a negligible level. The yields in the 16 'equal-δ_D' bins are shown in Table 3.7, including the raw signal yield, the total background (flat and peaking), and the final background subtracted yields.

Table 3.6: Yields for tags vs $K^-\pi^+$, showing estimates for signal and background yields in the signal region. The peaking background estimates are taken from simulation and are corrected for quantum correlations. The uncertainty on the background-subtracted signal yield is statistical only.

		Background		
	Raw	Flat	Peaked	Signal
$K^+\pi^-$	1736	12.7	0.1	1723.1 ± 41.8
$\pi^+\pi^-$	160	0.8	0.2	159 ± 12.7
K^+K^-	399	4.4	0	394.7 ± 20.0
$K^0_S\pi^0$	475	0.9	1.6	472.5 ± 21.8
$K^0_S\omega$	231	5.3	23.7	202 ± 15.3
$K^0_S\pi^0\pi^0$	234	8	2.5	223.5 ± 15.5
$K^0_S\phi$	52	1.2	3	47.8 ± 7.3
$K^0_S\eta\,[\gamma\gamma]$	69	1.8	0	67.2 ± 8.4
$K^0_S\eta\,[\pi^+\pi^-\pi^0]$	33	0.4	5.4	27.2 ± 5.8
$K^0_S\eta'\,[\eta\pi^+\pi^-]$	32	0	0.3	31.7 ± 5.7
$K^0_L\pi^0$	741	28.9	16.7	703 ± 27.9
$K^0_L\omega$	267	0.9	19.7	247.3 ± 17.0
$\pi^+\pi^-\pi^0$	983	6.9	24.2	951.9 ± 31.4

Table 3.7: Yields for $K^-\pi^+\pi^+\pi^-$ vs $K^0_S\pi^+\pi^-$ in bins of the $K^0_S\pi^+\pi^-$ phase-space.

Bin	Raw	Bkg.	Signal	Bin	Raw	Bkg.	Signal
1	357	16.8	340.2 ± 18.9	-1	190	16.8	173.2 ± 13.8
2	213	5.8	207.2 ± 14.6	-2	60	5.8	54.2 ± 7.7
3	187	3.2	183.8 ± 13.7	-3	49	3.2	45.8 ± 7.0
4	64	3.0	61.0 ± 8.0	-4	44	3.0	41.0 ± 6.6
5	181	6.8	174.2 ± 13.5	-5	101	6.8	94.2 ± 10.0
6	112	4.1	107.9 ± 10.6	-6	37	4.1	32.9 ± 6.1
7	287	4.3	282.7 ± 16.9	-7	39	4.3	34.7 ± 6.2
8	290	6.8	283.2 ± 17.0	-8	80	6.8	73.2 ± 8.9

3.4 Measurement of observables

3.4.1 Normalisation

The ρ observables are the ratio of the measured yield to the yield expected in the absence of quantum correlations. For the double-tag F vs G, the expected yield in the absence of quantum correlations is

$$N(F,G) = N\varepsilon(F,G)\left(\mathcal{B}_F\mathcal{B}_{\bar{G}} + \mathcal{B}_{\bar{F}}\mathcal{B}_G\right), \tag{3.14}$$

where $\varepsilon(F,G)$ is the double-tag efficiency and $\mathcal{B}_X$ the branching ratio of $D^0 \to X$. The normalisation constant, N, is independent of the double-tag considered. The ρ observable is then written in terms of the background subtracted yield, $Y(F,G)$ as

$$\rho^F_G = \frac{Y(F,G)}{N(F,G)} = \frac{Y(F,G)}{N\varepsilon(F,G)} \left(\mathcal{B}_F \mathcal{B}_{\bar{G}} + \mathcal{B}_{\bar{F}} \mathcal{B}_G\right)^{-1}. \tag{3.15}$$

For the flavour-specific tags, quantum correlations have negligible impact on the opposite sign yields and hence these can be used as a normalisation channel for the yields in order to extract the ρ-observables. Labelling the opposite sign double-tag yield as $Y(F,\overline{G})$, the same-sign observables can be written as:

$$\rho^F_G = \frac{Y(F,G)}{Y(F,\overline{G})} \left(\frac{\mathcal{B}_F}{\mathcal{B}_{\bar{F}}} + \frac{\mathcal{B}_G}{\mathcal{B}_{\bar{G}}}\right)^{-1}, \tag{3.16}$$

where the implicit assumption is that the double-tag efficiencies factorise into their single-tag equivalents, and the efficiency for a single-tag and the conjugate tag are identical. The ρ-observable for the $K^-3\pi$ vs $K^-3\pi$ double-tag can be written as:

$$\rho_{K3\pi} = \frac{Y(K^-3\pi, K^-3\pi)}{Y(K^-3\pi, K^+3\pi)} \frac{\mathcal{B}_{K^+3\pi}}{2\mathcal{B}_{K^-3\pi}}, \tag{3.17}$$

with similar expressions for the other flavour specific double-tags.

For the *CP*-tags, the background-subtracted yields can be normalised using the total number of $D^0\overline{D}^0$ events, $N_{D^0\overline{D}^0}$, determined using the opposite-sign double-tag yields, and the branching ratio of the tag mode if this is known with sufficient accuracy, as is the case for the tags K^-K^+ and $\pi^+\pi^-$, with relative uncertainties of about 1.7% each. However, the other *CP*-tags have relative uncertainties in their branching fractions of between $3.4 \to 12\%$ [34]. As the maximum deviation in the *CP*-tagged yields is $2r_D$, which corresponds to about 11%, knowledge of the branching ratios becomes a limiting factor. Therefore, these tags are normalised with respect to the double-tag yield where the signal side of the decay is $K^-\pi^+$ rather than $K^-\pi^+\pi^+\pi^-$. The yield of this double-tag can be written as:

$$Y(K\pi, CP) = N\varepsilon(K\pi, CP)\mathcal{B}_{K\pi}\mathcal{B}_{CP}\left(1 + r^2_{K\pi}\right)\rho^{K\pi}_{CP}, \tag{3.18}$$

which can be rearranged to give an expression for the normalisation constant and *CP* branching ratio. This is substituted into the ρ observable for $K3\pi$:

$$\rho^{K3\pi}_{CP} = \frac{Y(K3\pi, CP)}{Y(K\pi, CP)} \frac{\varepsilon(K\pi, CP)}{\varepsilon(K3\pi, CP)} \frac{\mathcal{B}_{K\pi}}{\mathcal{B}_{K3\pi}} \frac{1 + r^2_{K\pi}}{1 + r^2_{K3\pi}} \rho^{K\pi}_{CP}. \tag{3.19}$$

Table 3.8: Values of external parameters used in the determination of the ρ-observables and subsequent fit to coherence and hadronic parameters.

Parameter	Value	Reference
$\mathcal{B}(D^0 \to K^-\pi^+\pi^+\pi^-)$	$(8.29 \pm 0.20)\%$	[51]
$\frac{\mathcal{B}(D^0\to K^+\pi^-\pi^-\pi^+)}{\mathcal{B}(D^0\to K^-\pi^+\pi^+\pi^-)}$	$(3.25 \pm 0.11) \times 10^{-3}$	[34]
$\frac{\mathcal{B}(K^+\pi^-\pi^0)}{\mathcal{B}(K^-\pi^+\pi^0)}$	$(2.20 \pm 0.10) \times 10^{-3}$	[34]
$r^2_{K\pi}$	$(3.49 \pm 0.04) \times 10^{-3}$	[44]
$\delta_{K\pi}$	$\left(191.8^{+9.5}_{-14.7}\right)^{\circ}$	[44]
x	$(0.37 \pm 0.16)\%$	[44]
y	$(0.66^{+0.07}_{-0.10})\%$	[44]
$\mathcal{B}(D^0 \to K^+K^-)$	$(3.96 \pm 0.08) \times 10^{-3}$	[34]
$\mathcal{B}(D^0 \to \pi^+\pi^-)$	$(1.402 \pm 0.026) \times 10^{-3}$	[34]
$F_+^{\pi\pi\pi^0}$	0.973 ± 0.017	[52]

This method therefore relies on the good knowledge of the $K\pi$ hadronic parameters from Ref. [44] to determine how the $D \to K^-\pi^+$ vs *CP* tags are altered due to quantum correlations. A further simplification can be made on the assumption that the efficiency factorises into the product of efficiencies for the single-tags. The dependence on the efficiency of the *CP*-tag then cancels, and the ratio of signal-tag efficiencies can be written in terms of the flavour-specific opposite-sign yields. After these manipulations, the ρ observable for the double-tag is written as:

$$\rho^{K3\pi}_{CP} = \frac{Y(K3\pi, CP)}{Y(K\pi, CP)} \sqrt{\frac{Y(K\pi, K\pi)}{Y(K3\pi, K\pi)}} \frac{1 + r^2_{K\pi}}{1 + r^2_{K3\pi}} \rho^{K\pi}_{CP}. \tag{3.20}$$

3.4.2 Systematic uncertainties

Several sources of systematic uncertainty are considered in the measurement of the ρ-observables. These can be roughly divided into four categories:

Normalisation procedure(s): The flavour-specific tags and most of the *CP*-tags are determined using normalisation channels, and the statistical uncertainties associated with these normalisation channels are propagated as a source of systematic uncertainty. For the modes that used the $K\pi$ normalisation procedure, there are small corrections taken from simulation to account for possible non-factorisation of efficiencies, which have corresponding systematic uncertainties.

External parameters: Various external inputs, such as the $D \to K\pi$ hadronic parameters, are required to calculate the ρ observables. The values and uncertainties of these parameters are given in Table 3.8. The uncertainties on these parameters are propagated onto the ρ-observables as a source of systematic uncertainty.

Background: There are additional uncertainties on the residual contamination from various sources of background: corrections are applied to the peaking background estimates to account for quantum correlations, which have corresponding uncertainties. An additional $\pm 20\%$ uncertainty is assigned to the estimate of $D \to K^0_\mathrm{S} K^\mp \pi^\pm$ in the like-sign tags to account for any mis-modelling of this decay mode in the simulation. Lastly, there is a potential *CP*-even contribution to $D \to \phi K^0_\mathrm{S}$ from an S-wave contribution lying under the ϕ, therefore the *CP*-odd fraction for this tag is allowed to vary in the range $[0.85, 1.0]$.

Efficiencies: There are corrections to simulated efficiencies to account for discrepancies between data and simulation, which have corresponding systematic uncertainties. These are standard corrections for the different particle types [53]. Lastly, there is a small systematic uncertainty to account for any non-uniformity of the acceptance of the $D \to K\pi\pi\pi$ phase-space.

3.4.3 Results

The ρ-observables are determined using the double-tag yields in Tables 3.5, 3.6 and external parameters detailed in Table. 3.8. The different *CP*-tags are combined by an error-weighted average, with the values for individual tags shown in Fig. 3.7. The values for the ρ observables are:

$$\begin{aligned}
\rho_{CP+} &= 1.061 \pm 0.019 \pm 0.028 \\
\rho_{CP-} &= 0.926 \pm 0.027 \pm 0.042 \\
\rho_{K3\pi} &= 0.757 \pm 0.239 \pm 0.122 \\
\rho_{K\pi} &= 0.719 \pm 0.168 \pm 0.077 \\
\rho_{K\pi\pi^0} &= 0.919 \pm 0.158 \pm 0.098,
\end{aligned} \tag{3.21}$$

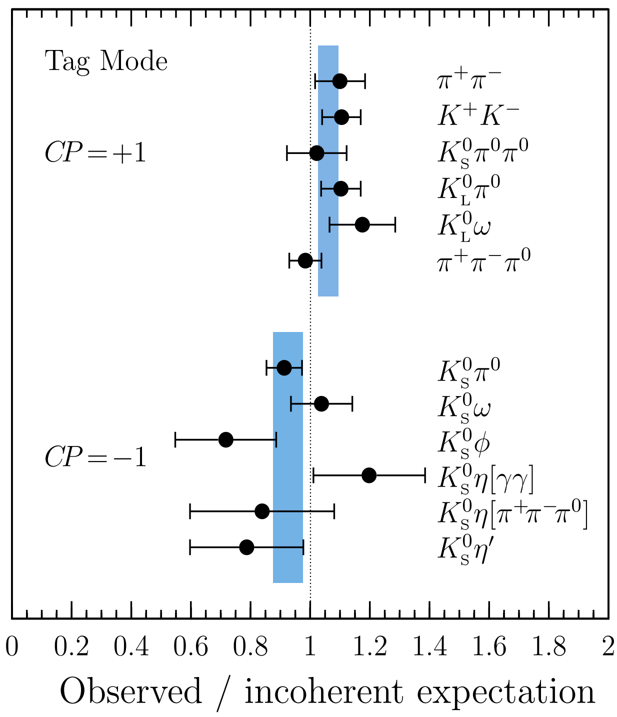

Figure 3.7: Results for the individual CP tagged observables. The error bars show both systematic and statistical uncertainties, and blue bands indicate the average ρ observable for CP^+ and CP^- tags.

where the first uncertainty is statistical and the second systematic. The ρ-observables differ significantly from unity, and hence quantum correlations are playing a role in these processes. The pattern of CP observables, with $\rho_{CP+} > 1$ and $\rho_{CP-} < 1$, implies an average strong-phase difference in the domain $[90, 270]^{\circ}$. The flavour-specific observables are all statistically limited, with the largest systematic uncertainties for these tags originating in the modelling of the $D \to K^0_S K^{\mp}\pi^{\pm}$ background.

The CP-tag results are systematically limited, with the largest uncertainties originating in the finite size of the $K^-\pi^+$ normalisation samples. Finally, the average CP-even observable Δ_{CP} as defined in Eq. 3.5 can be constructed from $\rho_{CP\pm}$ observables,

$$\Delta_{CP} = 0.063 \pm 0.015 \pm 0.021. \tag{3.22}$$

The $\pi^+\pi^-\pi^0$ tag is included in this average, with an appropriate correction for the small CP-odd component in this decay mode taken from Ref. [52]. The reduced χ^2 of the combination of CP-observables is 10.3/11, indicating a good compatibility between the different observables.

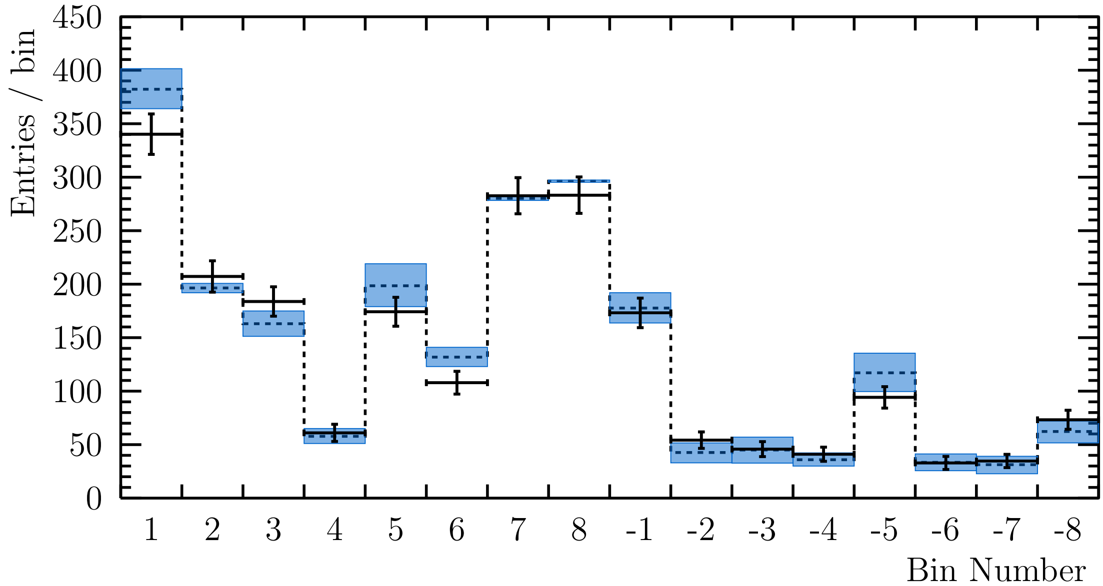

Figure 3.8: Bin-to-bin yields of $K^-\pi^+\pi^+\pi^-$ vs $K^0_S\pi^+\pi^-$ double-tag. The expected yields neglecting quantum correlations are shown by the dashed line, and the filled blue area shows the extent to which quantum correlations can alter the yield.

Results for the $K^0_S\pi^+\pi^-$ tag

The observables for the $K^0_S\pi^+\pi^-$ tag are the efficiency-corrected bin-to-bin yields. Efficiency corrections are taken from a sample of 250,000 simulated signal decays. The efficiencies are normalised by the efficiency in the highest bin. The efficiency-corrected bin-to-bin yields are shown in Fig. 3.8, where the efficiencies have been normalised to the most efficient bin. The expected values neglecting quantum-correlations per bin are calculated using the values of (c_i, s_i) obtained by a model-independent study of $D \to K^0_S\pi^+\pi^-$ reported in Ref. [45], and the values of K_i reported in Ref. [41]. The maximal deviations in the yields that can be induced by quantum correlations are also indicated by the filled area.

3.5 Interpretation

Constraints on the coherence factor and average strong-phase difference for $D \to K\pi\pi\pi$ decays are determined from the ρ-observables and $K^0_S\pi^+\pi^-$ bin-to-bin yields using a χ^2 fit. The χ^2 includes the full covariance matrix of the measurements including systematic uncertainties. The different observables are approximately related to the hadronic parameters by Eq. 3.3, with full expressions including the effects

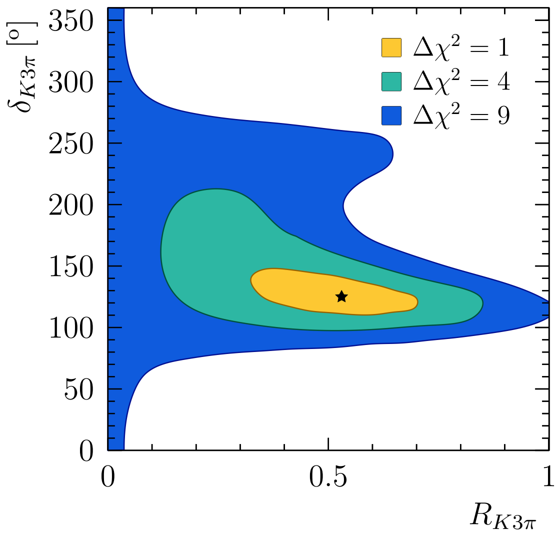

Figure 3.9: Scans of $\Delta\chi^2$ in the $R_{K3\pi} : \delta_{K3\pi}$ plane, using only observables from CLEO-c. The $\Delta\chi^2 = 1, 4, 9$ intervals are shown.

1113 of mixing given in Ref. [40]. The parameters that require external input, such as the charm-mixing parameters, x and y, are allowed to vary in the fit with gaussian constraints to their values found in external measurements. The hadronic parameters for $D \to K\pi\pi^0$ are also determined, taking double-tag yields for this decay mode from Ref. [41]. The coherence factor and average strong phase difference found by the fit are

$$\begin{aligned} R_{K3\pi} &= 0.53^{+0.18}_{-0.21} \\ \delta_{K3\pi} &= \left(125^{+22}_{-14}\right)^{\mathrm{o}}, \end{aligned} \tag{3.23}$$

where the uncertainties are a combination of statistical and systematic uncertainties. The χ^2 is scanned in the two-dimensional plane of $R_{K3\pi} : \delta_{K3\pi}$ to determine the confidence levels for the different parameters, with the $\Delta\chi^2$ shown in this plane in Fig. 3.9. The intervals are distinctly non-gaussian as the sensitivity to the average strong phase difference degrades at lower values of the coherence factor.

3.5.1 Constraints from charm mixing

Measurements of charm mixing also provide constraints on the hadronic parameters. The LHCb collaboration performed a time-dependent study [42] of the ratio of $D^0 \to K^+\pi^-\pi^-\pi^+$ to $D^0 \to K^-\pi^+\pi^+\pi^-$ decay rates, $R(t)$, which up to second order in time can be expressed as:

$$R(t) = (r_{K3\pi})^2 - R_{K3\pi} r_{K3\pi} \left(y \cos\left(\delta_{K3\pi}\right) - x \sin\left(\delta_{K3\pi}\right)\right) \frac{t}{\tau} + (x^2 + y^2) \frac{t^2}{\tau^2}, \tag{3.24}$$

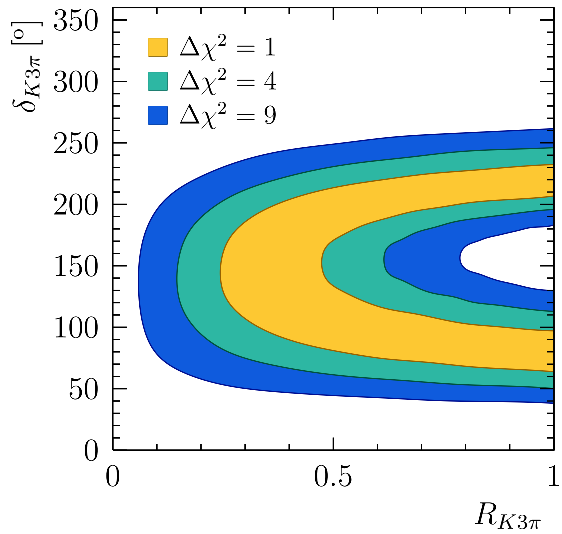

Figure 3.10: Scans of $\Delta\chi^2$ in the $R_{K3\pi} : \delta_{K3\pi}$ plane, using only constraints from charm mixing, showing the $\Delta\chi^2 = 1, 4, 9$ intervals.

where t is the proper decay time, τ is the mean lifetime of neutral D-mesons. The parameters x and y describe charm mixing. The mass splitting between the mass eigenstates, normalised by the average width of the two states is given by x, while y is the width splitting between the two states, normalised by twice the average width. The first term is associated with the pure doubly-Cabibbo suppressed amplitude and the last with the pure Cabibbo-favoured amplitude after mixing. The middle term is due to interference between these two processes, and therefore will vanish in the limit of small coherence ($R_{K3\pi} \to 0$). The coherence factor plays an analogous role in charm mixing as it does to the determination of γ in $B \to DK$ decays (Eq. 2.16), by diluting interference terms and hence reducing the sensitivity.

This time-dependent ratio can be used in two ways: either the mixing parameters can be constrained using external knowledge of the hadronic parameters, or the hadronic parameters can be constrained using knowledge of the mixing parameters, with Ref. [42] providing both interpretations. A scan of $\Delta\chi^2$ in the two-dimensional plane of $R_{K3\pi}, \delta_{K3\pi}$ is shown in Fig. 3.10. This analysis does not provide a strong constraint on the coherence factor, but provides constraints on the relative strong phase at higher values of the coherence factor. The likelihood contours from mixing have considerably different shapes to those from the CLEO-c observables, and therefore are very useful in improving the total constraint.

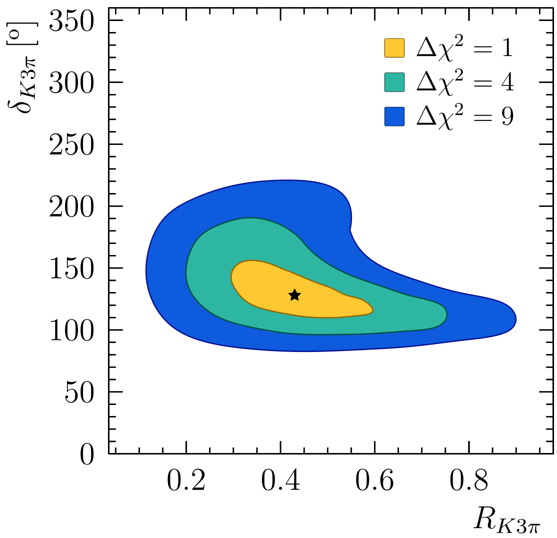

Figure 3.11: Scans of $\Delta\chi^2$ in the $R_{K3\pi} : \delta_{K3\pi}$ plane, showing the $\Delta\chi^2 = 1, 4, 9$ intervals.

3.5.2 Combined fit

The CLEO-c observables and LHCb charm mixing results are combined using the same procedure as described for only fitting the CLEO-c observables. The coherence factor and average strong phase found by the fit are

$$\begin{aligned} R_{K3\pi} &= 0.43^{+0.17}_{-0.13} \\ \delta_{K3\pi} &= \left(128^{+28}_{-17}\right)^{\mathrm{o}}, \end{aligned} \tag{3.25}$$

where the uncertainties are a combination of statistical and systematic uncertainties. The reduced χ^2 of the combined fit is 33.5/36, indicating that there are consistent values amongst the different observables for the coherence factor and associated parameters. The central value of the coherence factor is slightly lower, but still entirely statistically consistent with the CLEO-c only result. As a consequence, the sensitivity to the average strong-phase difference is slightly lower. However, the confidence intervals are significantly better behaved at lower values of the coherence than the CLEO-c only results, as is demonstrated by the $\Delta\chi^2$-scan in the two-dimensional plane shown in Fig. 3.11.

3.6 Conclusions

A measurement of the hadronic parameters for the decay $D \to K^-\pi^+\pi^+\pi^-$ has been presented in this chapter using a combination of observables measured from the CLEO-c $\psi(3770)$ data set and from a $D^0\overline{D}^0$ mixing analysis performed by the LHCb collaboration. These parameters will be useful in future measurements of the unitarity triangle angle γ using $B^- \to DK^-$ decays. The relatively low coherence factor observed for these decays indicates that there is potential for benefit in dividing the phase space of the D decay into a set of bins. It is critical to have models of the two amplitudes in order to decide how regions should be defined, the construction of which is the subject of the remainder of this thesis.

4

The LHCb detector

Contents

The Large Hadron Collider beauty (LHCb) experiment is one of the four major experiments in the Large Hadron Collider (LHC) programme. The first period of operations (Run-I) ran from 2011 until 2013, during which roughly $3\,\mathrm{fb}^{-1}$ of proton-proton collisions were recorded by the LHCb detector. The analysis discussed in the latter part of the thesis exploits this data set. The second period of operations began in 2015 (Run-II), and data taking will continue until the end of 2018. The experiments will then shut down for two years, during which time the accelerator and LHCb will be upgraded for higher luminosity conditions.

The LHCb detector is optimised to study the decays of hadrons containing beauty and charm quarks. These quarks are preferentially produced at low angles to the beamline, as shown in Fig. 4.1. Hence, LHCb is optimised in the forward region, instrumenting pseudorapidities between 2 and 5, which corresponds to an

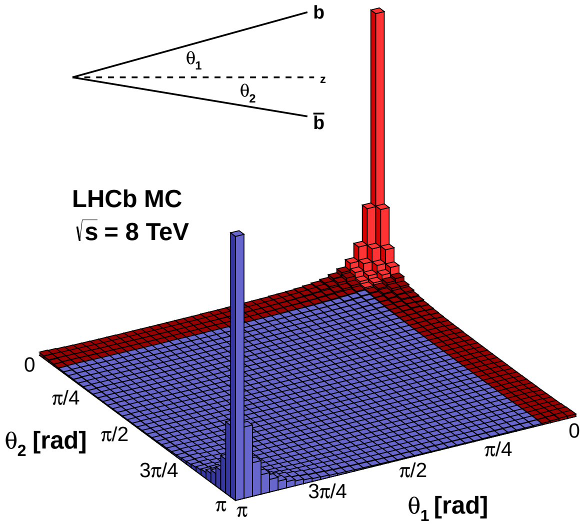

Figure 4.1: Expected production cross-section of $b\bar{b}$ quarks as a function of the angle between each quark and the beam axis. The coverage of the LHCb detector is indicated in red. Figure taken from Ref. [54].

angular coverage of about 14.5°, or 4% of the full solid angle. Despite this small angular acceptance, roughly a quarter of heavy quarks produced result in decay products inside the fiducial volume of the detector.

This chapter describes the different LHCb sub-detectors in Sect. 4.1- 4.5, which provide vertexing, tracking, particle identification and energy measurements. These different sub-systems are illusrated in Fig. 4.2. In addition to these sub-systems, it is critical to be able to quickly identify events that might contain interesting physics, which is the role of the trigger system that is briefly introduced in Sect. 4.6. Events that are deemed sufficiently interesting by the trigger are saved for further offline reconstruction and analysis, which is described in Sect. 4.7. Finally, it is important to understand the detector response in order to extract the underlying physics observables, which is typically achieved using a mixture of data-driven techniques and large samples of simulated events, with the LHCb simulation, described in Sect. 4.8. A full description of the LHCb detector and detailed discussion on the detector performance is given in Ref. [55].

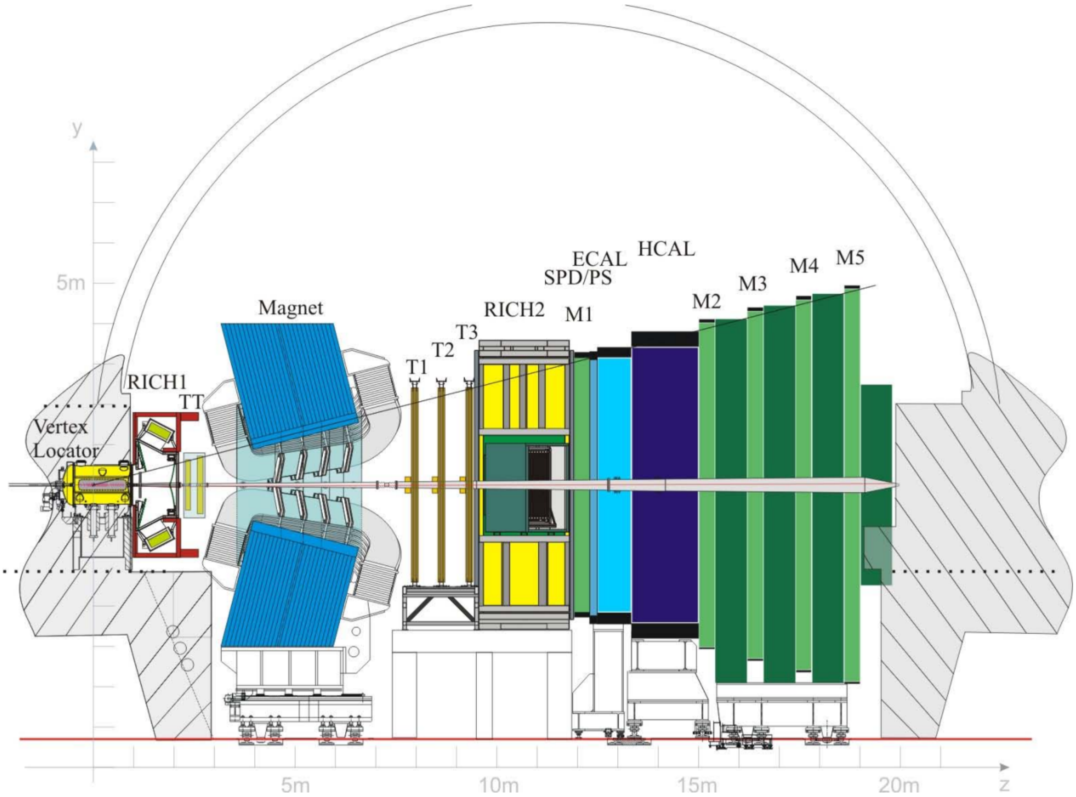

Figure 4.2: Diagram of the LHCb detector, showing the different sub-detector systems.

4.1 Vertex Locator

The VErtex LOcator (VELO) is the closest detector to the interaction region, and is designed to provide precision measurements of the positions of both the primary proton-proton collisions and the displaced vertices that are characteristic of the decays of hadrons containing b and c quarks. The VELO consists of 21 pairs of

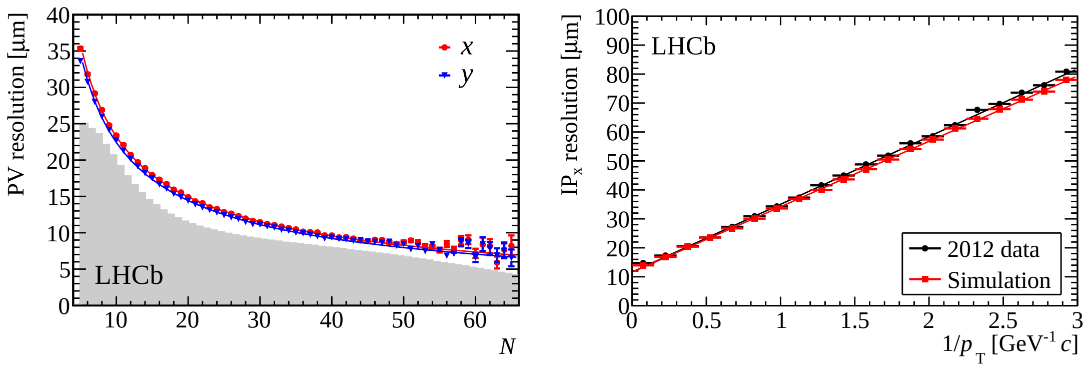

Figure 4.3: Performance plots for the VELO. Right: Impact parameter resolution in the x direction. Left: Position resolution as a function of the number of tracks included in fitting the vertex. Both figures are reproduced from Ref. [55].

silicon strip modules placed around the interaction region. Each module has two silicon strip sensors, one with strips in the radial direction and the other in the ϕ direction. While the beams are being injected and stabilised, the inner edge of the VELO modules are about 35 mm from the interaction region. Once the beams are stable, the VELO is mechanically closed around the interaction region until the inner edge is about 5 mm from where the beams collide. The positions of vertices are fitted using tracks reconstructed by the VELO. The performance of the VELO is discussed in detail in Ref. [56]. The transverse position resolution of primary vertices is shown in Fig. 4.3 as a function of the number of tracks, which demonstrates an extremely precise measurement of the position of the underlying proton-proton interaction. This in turn allows for a precise measurement of the impact parameter (IP), the distance of closest approach between a track and a vertex. The precision of the IP measurement is critical in separating tracks that come from secondary vertices from those originating in the primary vertex. The IP resolution is $(15 + 29/p_T)\,\mu\text{m}$ and is shown in Fig. 4.3, with the resolution degrading for low momentum tracks due to multiple scattering. The VELO therefore provides excellent identification of tracks coming from secondary vertices, as is characteristic of the decay products of hadrons containing the heavy quarks which typically fly $\mathcal{O}(1)$ cm in LHCb before decaying.

4.2 Tracking system

The tracking system consists of four different detectors and a conventional dipole magnet with approximately 4Tm of bending power in the horizontal plane. An important attribute of LHCb is the ability to change the polarity of the magnet, which is typically done several times during a year of data taking. As positively and negatively charged particles will bend in opposite directions for a given polarity, changing the polarity of the magnet mitigates systematic uncertainties from the detector having an asymmetrical tracking efficiency.

The first tracking station, the Tracker Turicensis (TT) is placed upstream of the magnet, and instruments the full LHCb acceptance with four layers of silicon strip sensors. The three stations placed downstream of the magnet consist of an inner region instrumented with silicon strips (collectively referred to as the Inner Tracker or IT), and a larger outer region instrumented with drift-tube detectors (referred to as the Outer Tracker or OT). Tracks are measured by these sub-detectors with a momentum resolution of between 0.5% and 1%, depending on the track

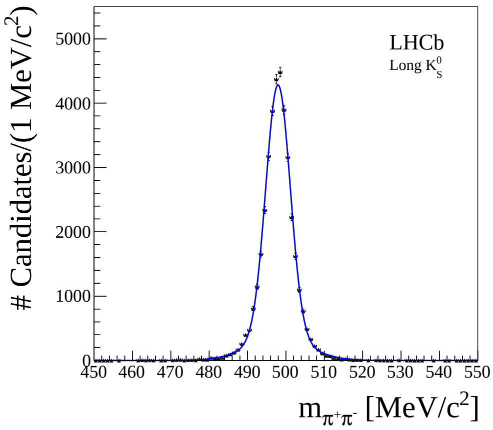

Figure 4.4: Invariant mass of $K_S^0 \to \pi^+\pi^-$ candidates, where both of the charged pions have left tracks in the VELO detector and the K_S^0 vertex is well separated from the PV. Reproduced from Ref. [55]

momentum. The momentum resolution is crucial in providing an excellent invariant-mass resolution. The invariant-mass distribution for $K_S^0 \to \pi^+\pi^-$ candidates is shown in Fig. 4.4, with a mass resolution of about 3.5 MeV/c^2. Momentum resolution plays an additional role in amplitude analyses: a good resolution is required for such a study as the amplitude is a (Lorentz-invariant) function of the four-momenta, and hence will be difficult to describe if the momentum resolution is not considerably better than the smallest features of the amplitude.

4.3 Particle identification

The separation of different species of long-lived charged particles is crucial in performing flavour physics measurements. For example, it is essential to be able to distinguish between kaons and pions in order to perform the analysis described in the latter chapters of this thesis. The principal component of the particle identification (PID) system at LHCb is a pair of Ring Imaging CHerenkov (RICH) detectors. A ring of photons is produced when a charged particle traverses a medium at a velocity greater than the speed of light in that medium. The opening angle of this ring, sometimes referred to as the Cherenkov angle, can be used to infer the velocities of particles, which combined with momentum information from the tracking system can be used to form a likelihood that a track was left by a particle of a given species. Information from the calorimeters and muon system is also combined into forming a global likelihood that a track is from a given species. RICH detectors

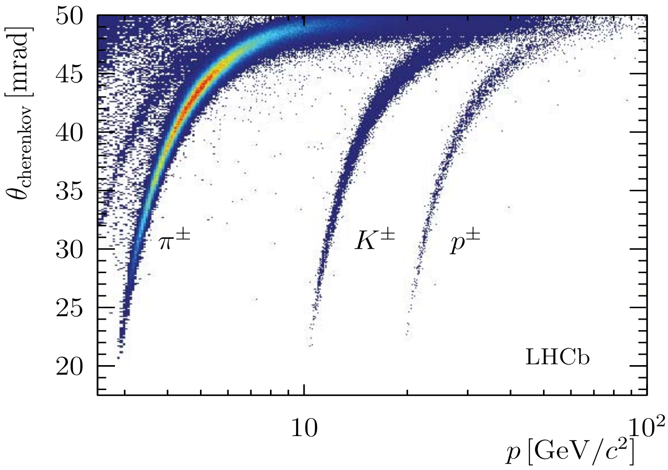

Figure 4.5: Cherenkov angle reconstructed for different species of particles as a function of momentum in RICH-I. Reproduced from Ref. [55].

are optimised for a specific range of track momentum by selection of the radiator medium. A medium with higher refractive index has a reduced energy threshold at which Cherenkov radiation is emitted, but the dependence on velocity also saturates at lower energies, while the converse is true for a medium with a lower refractive index. Therefore, LHCb has two RICH detectors and three radiator media to cover the full momentum range. The first RICH detector (RICH-I) is placed directly after the VELO, before the magnetic field and tracking system, and is optimised for low momentum particles. RICH-I has two radiators, aerogel[1] and C_4F_{10}. The Cherenkov angle for different species of particles in this detector is shown in Fig. 4.5 as a function of track momentum, and provides good separation of pions and kaons up to about $20\,\text{GeV}/c$. The second RICH detector is placed downstream of the magnet, and is designed to give separation of tracks with momentum between $15\,\text{GeV}/c \rightarrow 100\,\text{GeV}/c$, and as such uses CF_{10} as a radiator medium, which has a considerably lower refractive index than that used in RICH-I.

4.4 Calorimeters

The calorimeter system provides a fast trigger signal on non-muon tracks with high transverse energy, which is crucial for selecting purely hadronic final states. The calorimeters are also used to identify electrons, photons and hadrons, and provide a measurement of their energy. The calorimeter system consists of four

[1] The aerogel was removed for Run-II due to a degradation of performance at higher occupancies

sub-detectors. The calorimeters have the same basic design: particles traversing the detector produce scintillation light, which is collected by photo-multiplier tubes. The furthest sub-detector upstream is a scintillating pad detector (SPD). The SPD has no radiating material upstream, and hence energy is only deposited by charged particles, therefore providing separation between photons and electrons. The SPD is separated from the preshower (PS) detector by a thin lead converter of about 15 mm. The next detector is the electromagnetic calorimeter (ECAL), which has interleaved layers of lead absorbers and scintillating layers. The ECAL is sufficiently thick that showers from high energy photons are fully contained, and hence $1\% \oplus \frac{10\%}{\sqrt{E(\,\mathrm{GeV})}}$ is the nominal resolution [57].

The furthest calorimeter sub-system downstream is the hadron calorimeter (HCAL), which has the same design as the ECAL but with much thicker absorbers made of iron. The HCAL is too thin to fully absorb hadronic showers, and hence has a limited energy resolution of $\frac{\sigma_E}{E} = \frac{69\%}{\sqrt{E(\,\mathrm{GeV})}} \oplus 9\%$ [57]. The limited energy resolution is not a critical concern as the main purpose of the HCAL is to provide a trigger signal for purely hadronic final states, which can require less stringent energy requirements on particles.

4.5 Muon system

The muon system consists of five different stations. The first is placed upstream of the calorimeter system, and the other four downstream. The first station consists of both gas multiplier foils in the inner region where the particle flux is highest, and an outer region instrumented with multi-wire proportional chambers (MWPCs). The four downstream stations consist of MWPCs, with 80 cm thick iron plates placed in between the active areas to select only highly penetrating particles, i.e. muons. The muon system performs several important functions: firstly, it provides positive identification of muons, as there is only a small probability any other species of particle will be able to traverse the entire detector. Conversely, it provides some negative identification of the other species of particle: if a track does not have hits in the muon system associated with it, it is more likely to be of one of the other species. Information from the muon system is therefore combined with information from the RICH detectors and calorimeter system in forming the likelihood associated with assigning a given particle species to a track. A second important function of the muon system is to provide a rough estimate of the transverse momentum of the muon. The first three stations are segmented enough in the bending plane of the magnet to give a first estimate of the muon transverse momentum with roughly 20% precision. This is used in the hardware trigger to identify muons with high transverse momentum, which is a clean trigger signal used in many analyses, including those presented in the latter half of this thesis.

4.6 Trigger system

The LHCb trigger [58] system consists of three separate levels of triggers. At each stage, more of the detector is read out and more sophisticated selections applied. A summary of the data flow through the trigger system is shown in Fig. 4.6. The Level-0 (L0) trigger is designed to reduce the data-rate to a manageable level for the latter stages of the triggering system. The bunch crossing rate during Run-I was 20 MHz, and increased to 40 MHz for Run-II. Only parts of the detector are read out in making the L0 decision. The L0 trigger reduces the rate to about 1 MHz, such that the higher levels of the trigger can use the full detector information. The L0 trigger relies on the calorimeter system to provide a fast signal on tracks with large transverse energy, which is typical of events that contain interesting physics, as opposed to the relatively soft and dominant spectrum from pure QCD events. The muon system also provides a first measurement of the transverse momentum of highly penetrating particles, i.e. muons, and provides a clean trigger for many analyses.

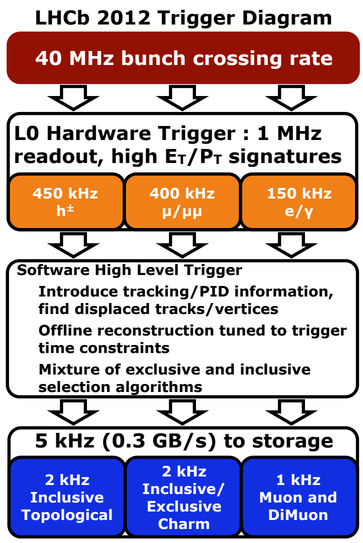

Figure 4.6: The trigger scheme used by LHCb during Run-I.

The second stage of the trigger system is the High Level Trigger or HLT, and reduces the 1 MHz rate from the L0 trigger to about a few kHz. The HLT is split into two stages. The first stage, HLT1, reads out information from the VELO and TT stations in addition to those detectors used in L0. Primary vertices are reconstructed using a minimum of 5 VELO tracks, then the impact parameter of other tracks with respect to each vertex is measured. Tracks with large impact parameters, those that are likely to come from secondary vertices, are matched with hits in the tracking stations. If a track can be matched with hits in the muon chambers, it is also extrapolated onto the tracking stations. HLT1 reduces the rate to about 40 kHz. This allows the second stage of the HLT, HLT2, to perform a more complete reconstruction of the event. This stage of the trigger contains both exclusive selections that make particular requirements for a given analysis, and inclusive selections that use the broad characteristics of decays of interest. The analysis presented in this thesis uses a set of inclusive trigger signals that rely on reconstructing the topology of a B-meson decay: Two, three or four high quality tracks with low distances of closest approach to each other are combined to form a secondary vertex. Various quantities related to this group of tracks, such as their total transverse momentum or the significance of the separation between this secondary vertex and the primary vertex, are combined using a boosted decision tree [59] to form a single discriminator. Events pass the topological trigger if the value of this discriminator passes some threshold. Events containing a track identified as a lepton are rarer than those where all tracks are identified as hadrons, and hence the threshold on the topological triggers is lowered if one of the tracks is identified as a lepton, by matching hits in the muon chambers or clusters in the ECAL that are identified as coming from electrons. The output rate of HLT2 is about 10 kHz, which is then written to disk to be reconstructed offline using the full detector information and exclusive selections on physics events of interest.

4.7 Offline

Events written to disk by the trigger are processed with full detector alignment and calibration to reconstruct all the tracks and vertices, including calculating the likelihoods of tracks coming from different particle species. A process referred to as *stripping* performs hundreds of different dedicated reconstructions on events to attempt to match them with particular physics channels. For example, the decay $D \to K\pi\pi\pi$ is reconstructed by attempting to form a good vertex from four tracks that is well separated from the PV. Various criteria are applied on the different components of the decay chain, such as thresholds on the momenta of tracks or “windows” on the total invariant-mass of some combination of tracks about the nominal mass of the reconstructed particle. These dedicated selections are referred to as *stripping lines*, and are performed centrally using the Worldwide LHC Computing Grid (WLCG) [60].

4.8 Simulation

Samples of simulated events are utilised to understand the detector response, and are also often used to optimise the selection requirements for a given physics channel. Underlying proton-proton interactions, fragmentation and the hadronisation of the resultant quarks are simulated using PYTHIA [61, 62]. These simulated events are typically required to hadronize to a particle of interest, such as a charged B-meson. The decay of these hadrons is then simulated using the EvtGen [49] package, which is typically configured such that the hadrons are forced to decay into a final state of interest. EvtGen is supplemented by a plug-in system that allows the generation of the specific kinematics of a decay channel. For example, a plug-in has been developed to simulate multi-body decays using the amplitude framework described in Sect. 6.6. The CPU requirements of the simulation are often reduced by placing additional requirements on the generated signal candidate to remove events that would not pass the selection, such as those with tracks of interest outside the fiducial acceptance of the detector or produced at very low momentum. Such events are discarded before simulating the detector response, as this stage normally takes the majority of the processing time.

The generated particles are then propagated through the detector using the GEANT4 framework [63, 64], including material interactions. The response of the front-end electronics and the hardware trigger are then simulated separately. Simulated events then should closely emulate the data events recorded by the detector, and are processed with the same software trigger, reconstruction and stripping selections as the real data. Truth level quantities, such as the relationships between different particles in the decay chain and the four-momentum they had when generated are kept such that these can be compared with the reconstructed quantities.

5

Selection of $D^0 \to K^{\pm}\pi^{\mp}\pi^{\mp}\pi^{\pm}$ decays

Contents

The amplitude analyses of $D^0 \to K^-\pi^+\pi^+\pi^-$ and $D^0 \to K^+\pi^-\pi^-\pi^+$ are based on $3\,\mathrm{fb}^{-1}$ of Run-I LHCb data taken in 2011 and 2012 at 7 TeV and 8 TeV, respectively. The decay chain that is reconstructed to identify neutral charm mesons is discussed in Sect. 5.1. The loose offline selection applied in reconstructing this decay is described in Sect.5.2. Further selection is applied offline, using both a multivariate classifier and cuts on certain key discriminators. This is described in Sect.5.3. Various sources of peaking background are considered in Sect.5.4. The signal and background yields for each mode are extracted using a two-dimensional unbinned maximum likelihood fit to the $m_{K\pi\pi\pi} : \Delta m \equiv m_{K\pi\pi\pi\text{slow}} - m_{K\pi\pi\pi}$ plane, as described in Sect. 5.5. Section 5.6 assesses the size of the mixing effects in the selected sample. Finally, the impact of the full reconstruction and selection chain on the phase-space acceptance is estimated using simulated events in Sect. 5.7.

5.1 Secondary charm decays and flavour tagging

The decay chain $B \to D^*(2010)^+\mu^-\nu X$ with $D^*(2010)^+ \to D^0\pi^+$ is reconstructed as a clean source of neutral D mesons. The topology of this decay chain is shown in Fig. 5.1. The hard proton-proton interaction at the primary vertex (PV) produces b-quark(s), as well as numerous other decay products. The b-quarks then hadronize to one of a number of mesons or baryons (B^+, B^0...). The b-hadron then flies about 1 cm in the detector rest frame before decaying. A few percent of b-hadrons will decay to the $D^*(2010)^+\mu^-\nu X$ final state, where state X can be some additional hadrons. For example, the decays of charged B-mesons require a minimum of one additional charged hadron from the B decay in order to decay to this final state. The $D^*(2010)^+$ strongly decays to a charm meson and a pion, which is referred to as *slow* due to the relatively small momentum transfer involved in this decay. The D-meson then flies about 0.5 cm before decaying.

The flavour of the neutral D-meson must be determined in order to distinguish between the $D^0 \to K^-\pi^+\pi^+\pi^-$ and $D^0 \to K^+\pi^-\pi^-\pi^+$ modes. This can be measured at its production by flavour tagging. The charge of the muon and pion from the $D^*(2010)$ decay are used to infer the flavour of the neutral D meson at its production. A negatively charged muon and positively charged pion implies a D^0 was produced, whereas a positively charged muon and negatively charged pion implies a $\overline{D}^0$ was produced. As two different tracks are used to tag the flavour of the D-meson, the sample is referred to as *double-tagged*[1]. Flavour tagging measures the flavour of the neutral D-meson when it is produced, however due to charm mixing the physical meson will contain a component from the other flavour when it decays. Therefore, the amplitudes that are measured will contain a mixture of Cabibbo-suppressed and favoured amplitudes. Owing to the low rate of such oscillations, the mixing contribution to the measured $D^0 \to K^+\pi^-\pi^-\pi^+$ amplitude is expected to be small. In the $D^0 \to K^-\pi^+\pi^+\pi^-$ case, the contribution from mixing and then the DCS amplitude is negligible. Due to this distinction, $D^0 \to K^-\pi^+\pi^+\pi^-$ is

[1]This is an entirely different meaning to double-tagging in the context of Ch. 3

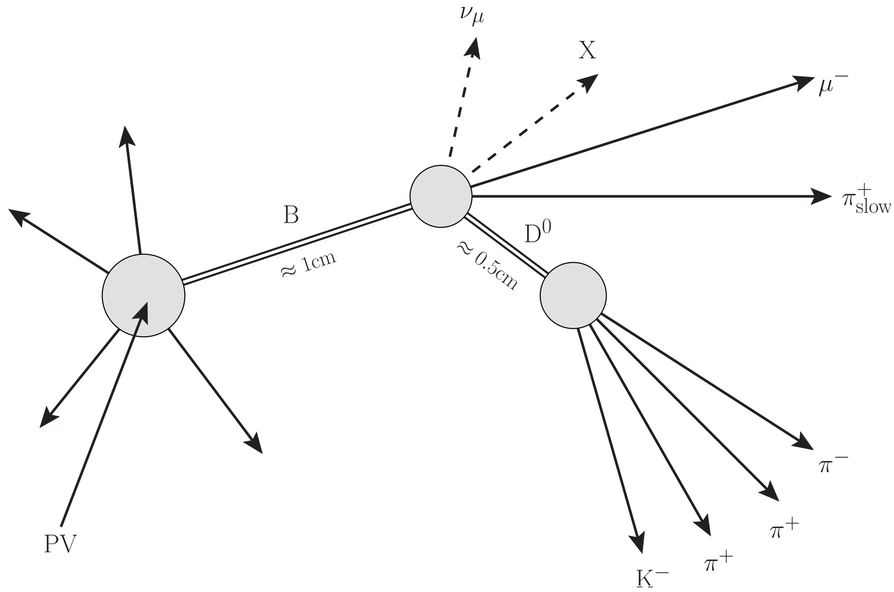

Figure 5.1: Topology of doubly-tagged secondary charm decays.

referred to as Right Sign (RS), and $D^0 \to K^+\pi^-\pi^-\pi^+$ as Wrong Sign (WS), where the D^0 flavour in each case is determined by the tag.

The method of selecting a double-tagged semileptonic sample can be contrasted with the alternative possible approach of exploiting prompt production of neutral D mesons. Although the cross section for prompt production is considerably higher, there are several advantages to the double-tagged semileptonic sample. Firstly, the additional separation from the primary vertex (PV) from the flight of the B meson suppresses backgrounds from random combination of particles from the underlying proton-proton interaction. Secondly, the muon from the B provides an efficient trigger for these decays that is independent of the D^0 daughters. Thirdly, the additional boost from the B decay de-correlates the D rest frame from the lab frame, which ensures a relatively uniform phase-space acceptance. These different factors mean that the doubly-tagged sample has a significantly higher purity than the prompt sample, which is critical for studying the WS decay. Therefore, the double-tag sample is an ideal source of D mesons for an amplitude analysis.

5.2 Preselection

Candidates are reconstructed centrally in a so-called *stripping* according to a dedicated physics reconstruction of a given channel, as described in Sect. 4.7. The $B \to D^*(2010)^+ \left[D^0\pi^+_{\rm slow}\right] \mu^-\mathrm{X}$ decay chain is reconstructed in stages, with requirements placed on tracks and various composite objects, such as the D, B meson candidates, to identify high quality signal candidates and reject background. The following variables and definitions are used in the selection:

- Doca is the distance of closest approach between two tracks. A small Doca between two tracks implies they may have come from a common vertex. This measure is often used early in a selection to reduce the number of combinations of tracks that vertices can be built from. The distance of closest approach in units of its error, labelled χ^2_{Doca} by convention, is also often a useful discriminating variable.

- Ip is the impact parameter, defined as the distance of closest approach between a track and a given vertex, and is pictured in Fig. 5.2. A large impact parameter with respect to a primary vertex implies that a track may have originated from a secondary vertex. Selecting tracks that come from the decays of secondary particles using the impact parameter therefore relies on the flight distance / lifetime of the decaying particle in order to discriminate between these tracks and those that originate from a primary vertex and thus have a smaller impact parameter. The 'significance' of the impact parameter, which is labelled χ^2_{Ip}, is defined as the difference in χ^2 for a fit to a vertex and a fit to the vertex excluding a track (or set of tracks), and is also a powerful discriminator on whether tracks originate from a given vertex.

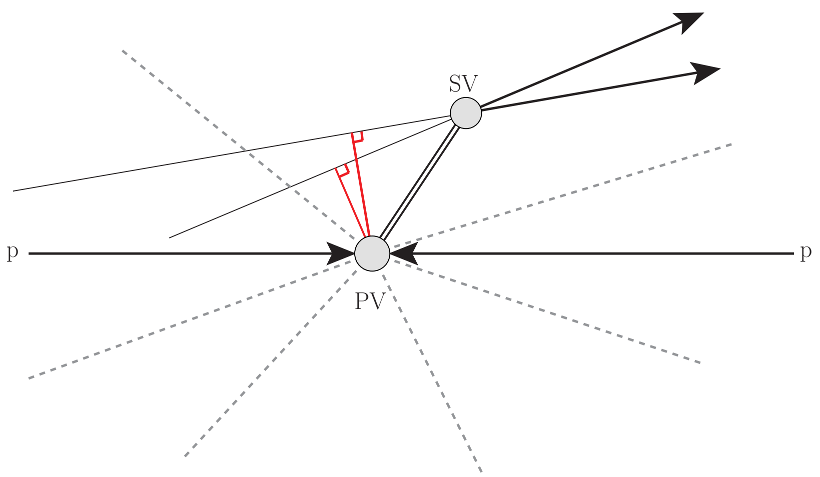

Figure 5.2: The geometry of the decay of a particle (double line) that flies a significant distance from the PV before decaying at a secondary vertex (SV). The decay products of this particle have large impact parameters, which are indicated in red, with respect to the PV.

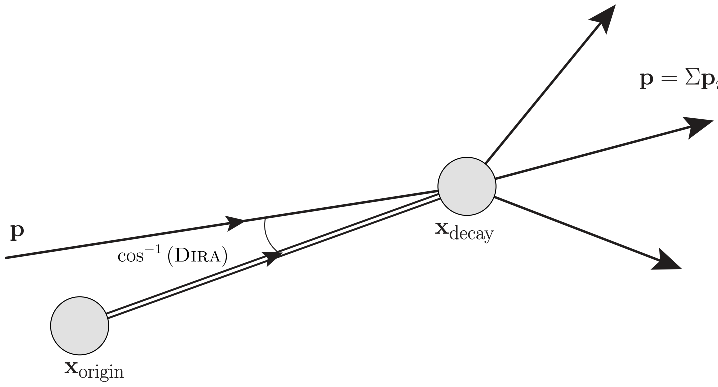

Figure 5.3: A short-lived particle produced at $\mathbf{x}_{\text{origin}}$ flies some distance before decaying at $\mathbf{x}_{\text{decay}}$. Shows the definition of the DIRA for these two vertices and, $\mathbf{p}$, the momentum of the decaying particle inferred from its decay products.

- BPV (best primary vertex) is the primary vertex that a track is most consistent with originating from, defined by the vertex with which the track has the lowest impact parameter significance. Several useful quantities are defined with respect to this vertex, for example, primary vertex impact parameters are usually defined with respect to this 'best' vertex.

- DV (decay vertex) is the vertex reconstructed from the decay products of a relatively short-lived particle such as a B or D meson. The fit quality associated with such a vertex, χ^2_{DV}, is a common discriminator.

- The cosine of the direction angle, or DIRA, is defined as the cosine of the angle between the path implied by a pair of vertices and the direction of the momentum reconstructed from its decay products, as shown in Fig. 5.3. If both vertices have been correctly identified and the decaying particle has been fully reconstructed, the two vectors should be close to parallel, and DIRA$\to 1$. The angle between the two vectors will be larger if one or more of the tracks do not truly originate from the decay vertex, hence this discriminator is useful in reducing combinatorial backgrounds.

- Fits are used to measure track parameters and vertex positions. Requirements on the quality of these fits are useful in rejecting fake tracks and vertices that are not correctly reconstructed, where fit quality is described by a χ^2 per degree of freedom.

- The difference in log-likelihoods between particle mass hypothesis x and y for a track is given by Δ_{x-y}. For example, $\Delta_{K-\pi}(K^-)$ is the difference in log-likelihoods between kaon and pion mass hypotheses for the K^- candidate.

Table 5.1: Offline preselection requirements on track objects

		μ	π_{slow}	K	π
$p_T[\text{ GeV}/c]$	$>$	1.20	0.18	0.30	0.25
$p[\text{ GeV}/c]$	$>$	3.0	-	0.20	0.20
$P_{\text{ghost}}[\%]$	$<$	50.0	-	50.0	50.0
$\chi^2_{IP}(\text{BPV})$	$>$	9.0	-	9.0	9.0
$\chi^2_{\text{track}}/\text{dof}$	$<$	4.0	-	4.0	4.0
PID		$\Delta_{\mu-\pi} > 0.0$	-	$\Delta_{K-\pi} > 8.0$	$\Delta_{K-\pi} < 10.0$

The likelihood is taken from the particle identification procedure, which is mainly reliant on information from the RICH detectors to distinguish between hadrons, with additional information coming from the muon system to identify muons. Identifying a track with something other than a pion is a powerful discriminator against combinatorial backgrounds, as the majority of particles produced in proton-proton collisions are pions. It also is used to discriminate against specific physics backgrounds, such as misidentifying a RS decay as a WS decay via the exchange of two particle hypotheses.

- A ghost track is a track where a significant fraction of the hits associated with the track do not truly originate from the track. A multivariate classifier known as the *ghost-track probability* (P_{ghost}) is used to suppress these tracks, which combines fit quality information from the different sub-detectors into a single probability that the hits associated to a track truly originate from the track.

Composite particle candidates are built from tracks selected according to the requirements listed in Table. 5.1. The kaon must be well identified as a kaon by the RICH detectors, and all tracks except the slow pion must be well separated from the primary vertex and of good quality. The requirements on the composite particle candidates built from these tracks are listed in Table. 5.2. A D^0 candidate is then built from a kaon and three pions that all have small distances of closest approach with respect to each other. A fit is then performed to the common origin vertex of the four tracks, and various requirements placed on the fit and topology, such as that this secondary vertex is well separated from the primary vertex ($\chi^2_{\text{BPV}} > 100$). These requirements are listed in full in Table. 5.2. A slow pion is then added to the D^0 candidate to make a D^* candidate, and finally a muon added to the D^* candidate to make the B candidate.

Table 5.2: Offline preselection requirements on composite objects

Candidate	Requirement
D^0	$1.80\,\mathrm{GeV}/c^2 < m < 1.92\,\mathrm{GeV}/c^2$
	$\chi^2_{\mathrm{DV}}/\mathrm{dof} < 6.0$
	$p_T > 1.8\,\mathrm{GeV}/c$
	DIRA(BPV)> 0.99
	$\chi^2_{\mathrm{DOCA}} < 9.0$
	$\chi^2_{\mathrm{BPV}} > 100$
D^*	$m - m_{D^0} < 0.17\,\mathrm{GeV}/c^2$
	$\chi^2_{\mathrm{DV}}/\mathrm{dof} < 8.0$
B	$2.5\,\mathrm{GeV}/c^2 < m < 6.0\,\mathrm{GeV}/c^2$
	$\chi^2_{\mathrm{DV}}/\mathrm{dof} < 6.0$
	DIRA(BPV)> 0.999
	$z_{\mathrm{decay}}(D^0) > z_{\mathrm{decay}}(B)$

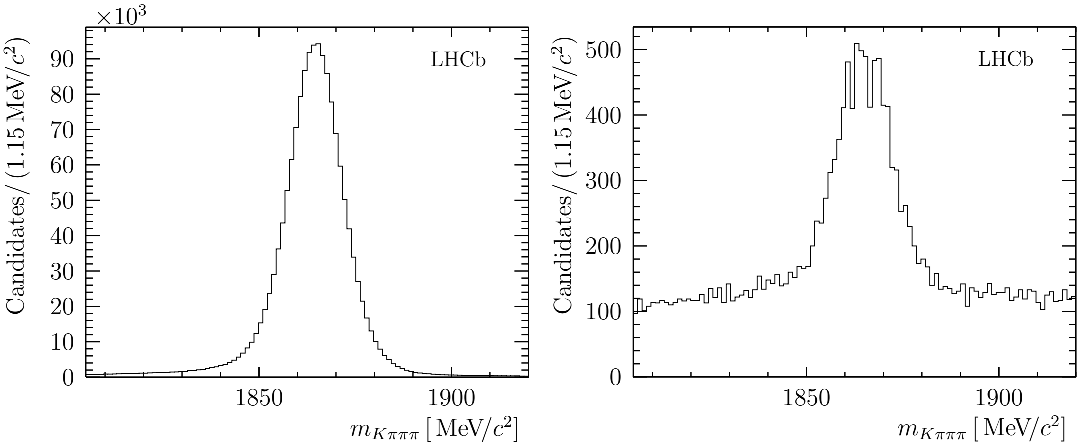

(a) RS data (b) WS data

Figure 5.4: $m_{K\pi\pi\pi}$ distribution for RS and WS data samples after the offline preselection.

The reconstructed invariant mass of the D^0-meson candidate is shown in Fig. 5.4 for RS and WS samples after the preselection, with the only additional requirement that $144.7\,\mathrm{MeV}/c^2 < m_{K\pi\pi\pi\pi_{\mathrm{slow}}} - m_{K\pi\pi\pi} < 146.15\,\mathrm{MeV}/c^2$. The RS sample is about 99% pure after the preselection within a signal region corresponding to about $\pm 3\sigma$ in the $m_{K\pi\pi\pi}$ distribution, while the purity of the WS sample is estimated to be about 50% using the yield in this region, the observed RS yield and the known ratio of branching fractions.

5.2.1 Trigger requirements

Stripped candidates are not generally required to come from any particular trigger selection. This has implications for the analysis as different trigger selections will generally have different acceptances. For example, if an event is recorded exclusively by a hadronic trigger signal on one of the D^0-meson decay products, there is a requirement on the transverse energy of one of these decay products, which would not be present had the recording of the event been triggered by a different track such as the muon. Therefore, requirements are placed on how events are triggered to ensure that selection efficiencies are well defined. For the hardware trigger (L0), it is required that either the candidate was triggered by the muon, or the trigger is independent of the tracks from the B candidate. This ensures the L0 decision is not correlated with the D daughter kinematics. For the first stage of the high-level trigger (HLT1), it is required that the candidate is triggered on either the muon or by any track contributing to the L0 decision (in practice 'L0 muon' due to L0 trigger requirement), or that the HLT1 decision is independent of the B decay. Lastly, the second high-level trigger stage (HLT2) is required to be triggered by either the single muon trigger or by the topological (requiring a 2, 3, or 4 track vertex) triggers. The topological requirements are loosened compared to generic topological triggers by requiring a muon in the event. Most candidates (76%) are accepted only by the topological lines. A small fraction (4%) of candidates are accepted exclusively by the muonic trigger, and the remaining candidates satisfy both sets of trigger requirements. Finally, candidates are accepted where the HLT2 decision is independent of the B decay daughters.

5.3 Offline selection

5.3.1 Multivariate classifier

The purity of the sample is increased further offline using a multivariate classifier, which combines many different variables that individually have some power to discriminate between signal and background to form a single classifier. A threshold can then be placed on the output of this multivariate classifier to make a sample with higher purity. The multivariate classifier used is a boosted decision tree (BDT) [65, 66], and is trained using 15 variables from each candidate, listed and described in Table 5.3. The variables are ordered according to their ability to distinguish

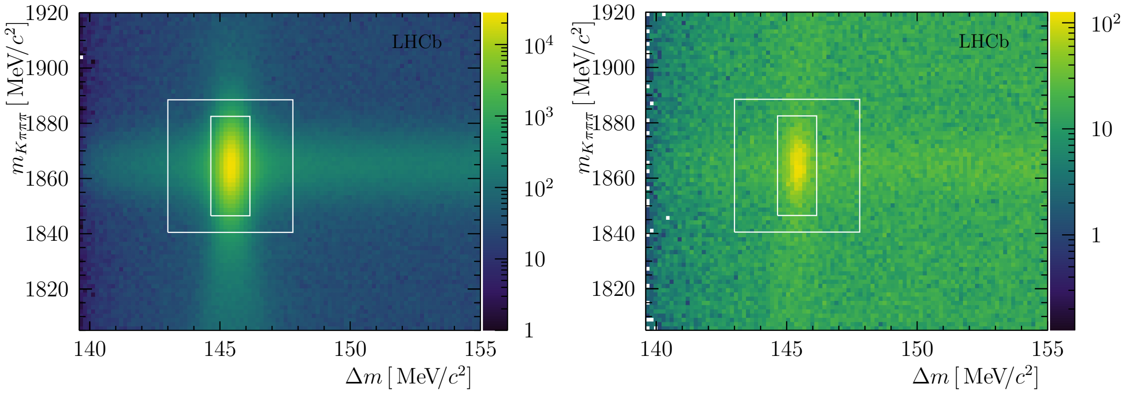

Figure 5.5: Two-dimensional distributions of $m_{K\pi\pi\pi}$ vs Δm for RS (right) and WS (left) samples prior to the application of the offline selection. The inner box shows the definition of the signal region, while the area outside the outer box shows the definition of the sideband used for studying background.

between the signal and background samples. Notably, kinematic variables pertaining to the D^0 daughters are also excluded from the selection to avoid biasing the phase space. Particle identification variables of the D^0 daughters are excluded, as applying efficiency corrections for these variables requires a data-driven approach that is not well suited to the use of a multivariate discriminator. The BDT is trained using the 2011 and 2012 RS candidates as the signal sample. The signal candidates are required to be in the region:

- $1846.5\,\mathrm{MeV}/c^2 < m_{K\pi\pi\pi} < 1882.5\,\mathrm{MeV}/c^2$ and
- $144.65\,\mathrm{MeV}/c^2 < \Delta m < 146.15\,\mathrm{MeV}/c^2$.

For the background sample, the WS sidebands are used, with a wider box defined to suppress WS signal leaking into the sideband:

- $\Delta m < 143.0\,\mathrm{MeV}/c^2$ or $\Delta m > 147.8\,\mathrm{MeV}/c^2$ or
- $m_{K\pi\pi\pi} < 1840.5\,\mathrm{MeV}/c^2$ or $m_{K\pi\pi\pi} > 1888.5\,\mathrm{MeV}/c^2$.

The definition of these regions is shown in the two-dimensional mass plane by Fig. 5.5. The sideband region corresponds to about six standard deviations of separation from the signal peak in Δm and about four standard deviations in $m_{K\pi\pi\pi}$. The trigger and PID calibration acceptance requirements are also applied to the samples used as a preselection. Half of the sample is used for training, the other half for testing, to verify that the BDT is not being over-trained. The

Table 5.3: Variables used in the BDT and their descriptions, ordered by their ability to discriminate between signal and background samples.

Variable	Description
log(PL_IPCHI2_OWNPV)	Logarithm of impact parameter significance of the slow pion with respect to the primary vertex.
log(D0_IPCHI2_OWNPV)	Logarithm of impact parameter significance of D^0 with respect to its associated primary vertex.
PL_TRACK_GhostProb	Ghost track probability of the slow pion.
D0_IP_OWNPV	Impact parameter of the D^0 candidate with respect to its associated primary vertex.
B_ENDVERTEX_CHI2	Fit quality of the B decay vertex (the $D^{*}\mu$ vertex)
D0_ENDVERTEX_CHI2	Fit quality of the D^0 decay vertex fit (the K$\pi\pi\pi$ vertex).
log(B_IPCHI2_OWNPV)	Logarithm of impact parameter significance of B with respect to its associated primary vertex.
D0_APCOSDIRA	Angle between the reconstructed D^0 momentum and the path implied by its birth and decay vertices. In this case, the D^0 birth vertex is taken to be the $D^{*}\mu$ vertex.
Mu_PT	Transverse momentum of the muon candidate.
Mu_TRACK_GhostProb	Ghost track probability of the muon candidate.
Mu_PIDmu	Difference in log-likelihoods between the muon and pion mass hypotheses for the muon candidate.
B_OWNPV_CHI2	The fit quality of the primary vertex associated with the B candidate.
log(Mu_IPCHI2_OWNPV)	Logarithm of impact parameter significance of the muon candidate with respect its associated primary vertex.
Mu_IP_OWNPV	Impact parameter of the μ candidate with respect to its associated primary vertex.
D0_ORIVX_CHI2	Fit quality of the $D^{*0}(2010)$ decay vertex fit (the $D^0\pi$ vertex).

signal training and testing samples therefore consist of 540,000 candidates each, and the corresponding background samples roughly 44,000 candidates each. The distribution of the BDT response to the signal and background samples is shown in Fig. 5.6(a), with each split into the testing and training sample. The BDT response is compatible between each testing and training sample, indicating that the classifier has not been overtrained. The optimal value for the BDT threshold is tuned to give maximum significance, $s/\sqrt{s+b}$, of the WS sample. This is determined by fitting the two dimensional plane $m_{K\pi\pi\pi} : \Delta m$ and scanning in BDT threshold. The number of signal candidates (s) in the WS sample is estimated using the number of

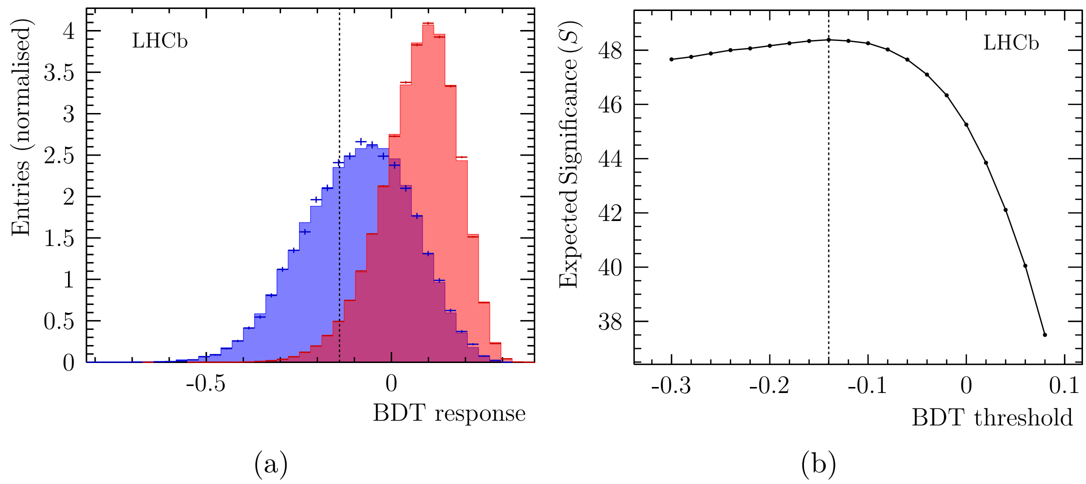

Figure 5.6: (a): Comparison of the BDT response to signal (red) and background (blue) samples, comparing training sample (filled) with testing sample (markers) (b): BDT threshold vs the expected significance (σ) of the WS signal.

signal candidates in the RS sample and the ratio of branching fractions reported in the PDG [34]. The number of background candidates (b) in the WS sample is taken directly from the fit. These fits are detailed in Sect. 5.5. The expected WS significance is shown as a function of the BDT threshold in Fig. 5.6(b). The optimal threshold is found to be BDT > -0.14, and at this threshold the WS sample consists of 3026 signal candidates at 82% purity. The total WS background is 646 ± 12 candidates, where 156 ± 10 are identified as being a RS candidate paired with the wrong slow pion, approximately 4% of the total sample. The RS sample consists of 890700 ± 927 candidates at 99.96% purity.

5.3.2 Rectangular cuts

A series of rectangular cuts are applied on other variables in addition to cutting on the multivariate classifier. Stronger requirements are applied on particle identification variables for the kaon in order to reduce cross-feed from the favoured decays into the WS sample. These elements of the selection are described in detail in Sect.5.4.1. Additionally, requirements are placed on the kinematics of the D^0 daughters such that they fall in the region where the RICH detectors perform well, which is for tracks with momenta between $3\,\text{GeV}/c$ and $100\,\text{GeV}/c$, and to have a pseudo-rapidity between 1.5 and 5.

A kinematic fit [67] is applied to the daughters of the D-meson candidate, constraining the D-meson mass to its true value. This fit is applied to improve

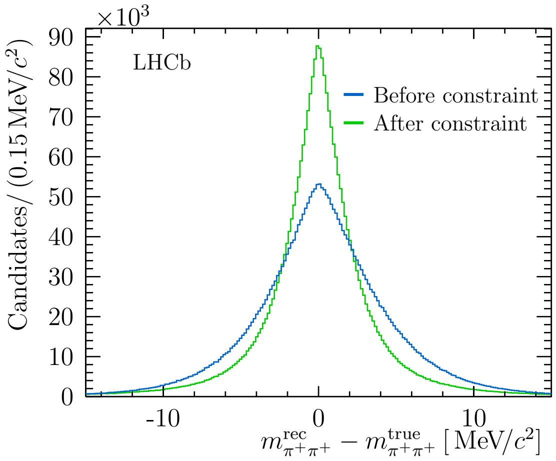

Figure 5.7: Difference between reconstructed and true same-sign dipion invariant-mass. Shown is the difference before and after D^0 mass constraint is applied, and is evaluated using simulated RS decays.

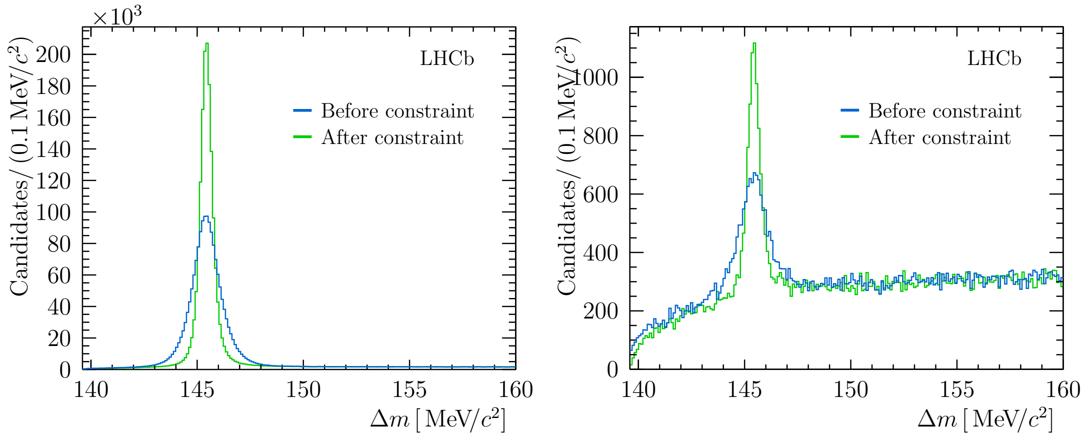

(a) RS data (b) WS data

Figure 5.8: Δm distribution in RS and WS data samples before (blue) and after(green) the B vertex constraint is applied.

resolution within the phase space for the amplitude fit. It is required that this fit converges ($\chi^2 > 0$). Fig. 5.7 shows the same-sign dipion invariant mass resolution before and after the mass constraint is applied. The resolution is improved by approximately a factor of two by applying this constraint.

A kinematic fit is also applied to the daughters of the B-meson candidate, refitting the track parameters under the hypothesis that they share a common vertex (the B decay vertex). This significantly reduces the Δm distribution width, which is shown for both RS and WS samples before and after this constraint is applied in Fig. 5.8. The only selection applied in each case is the $m_{K\pi\pi\pi}$ signal window. The narrower Δm distribution allows for a tighter signal window to be imposed and therefore greatly improves background rejection.

It is found that more stringent requirement on the ghost track probability for the kaon candidate is useful for removing combinatorial background, with $P_{\text{ghost}} < 15\%$ found to be the optimal cut. This variable is not included in the BDT as it is poorly described in the simulation, and potentially correlated with the D-meson phase space.

Multiple candidates will sometimes be found in the same underlying events. These candidates are not necessarily statistically independent, for example the same track may be common between different candidates. Therefore, only a single candidate is selected from each event by randomly selecting one candidate in events where there are multiple candidates remaining after the full selection. In practice, this only rejects a very small number of candidates, roughly 0.004% of each sample.

5.4 Peaking backgrounds

Sources of peaking background in the RS sample are negligible due to its large branching ratio and clean environment in which these samples are reconstructed. Several potential sources of peaking background in the WS sample are discussed in the following section.

5.4.1 Misidentified backgrounds

A notable peaking background in the WS sample originates in decays that have been reconstructed with the correct topology, but where the D-meson daughters have been incorrectly identified. One such background originates from the abundant favoured decays, where the kaon is misidentified as a pion and a positively charged pion is misidentified as a kaon. This is therefore a source of crossfeed from the RS decay into the WS sample. As two particle hypotheses are incorrect for this variety of background, it is referred to as a *double mis-id*. This background will generally be very complicated to model across the phase space, and will also have a different acceptance to the signal mode. Hence, further cuts are applied to suppress this contamination in the selection. Strong particle identification requirements are placed on the kaon, by requiring that the difference in log-likelihoods between the

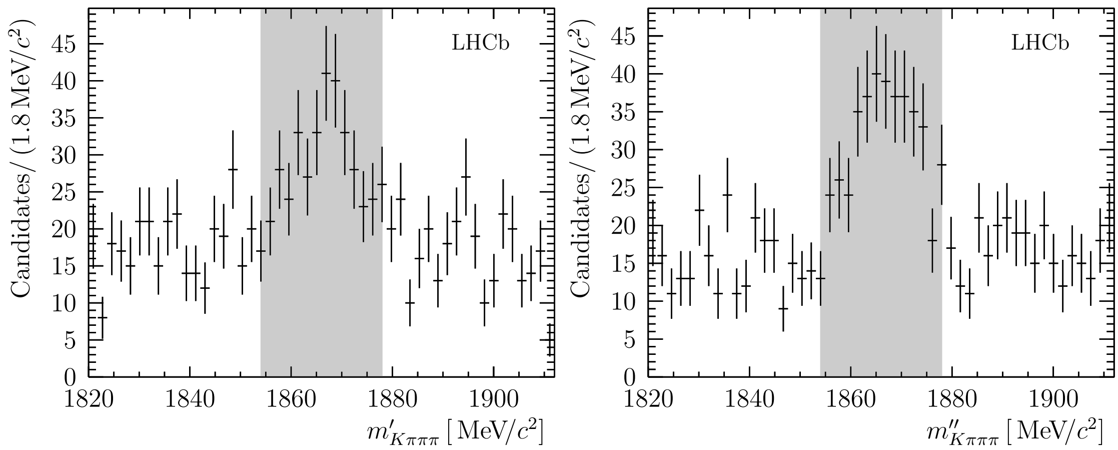

Figure 5.9: $m_{K\pi\pi\pi}$ shown under exchanging the mass hypothesis of the kaon with a pion. Each plot shows exchange of mass hypothesis of one of the pions of opposite charge to the kaon candidate. Double mis-id background is clearly seen about the nominal D^0 mass. The shaded region shows the area that is vetoed.

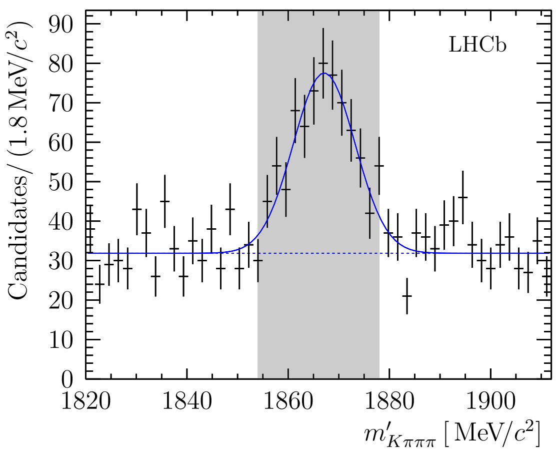

Figure 5.10: $m_{K\pi\pi\pi}$ shown under exchanging the mass hypothesis of the kaon with a pion, with both possible exchanges folded together. The distribution is fitted in order to estimate the residual contamination from this background after the veto is applied.

kaon and pion mass hypotheses for the kaon candidate is greater than ten. Such a requirement is also useful for reducing combinatorial backgrounds, as most particles produced from the primary interactions are pions. After this requirement, the kaon four-momentum is recalculated assuming the pion mass hypothesis, and one of the negatively charged pions with the kaon mass hypothesis. The invariant mass of the D meson is then reconstructed under this swapped hypothesis for each of the negatively charged pions. The invariant mass spectra for each of these swaps are shown in Fig. 5.9, and shows clear peaks at the nominal D-meson mass, indicating that there is residual contamination from this background. Therefore, candidates falling within $\approx 2\sigma = 12\,\mathrm{MeV}/c^2$ of the nominal D^0 mass are vetoed.

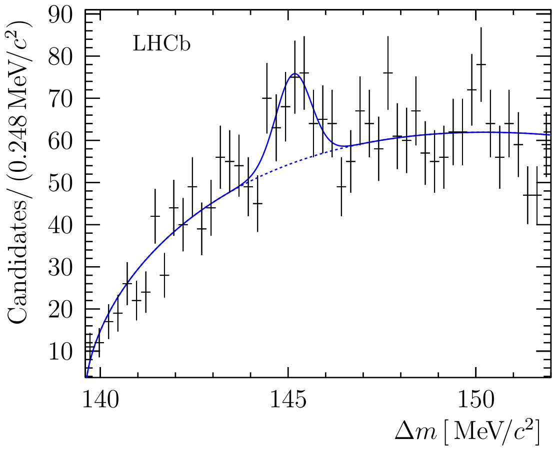

Figure 5.11: Δm in the low sideband of $m_{K\pi\pi\pi}$ ($m_{K\pi\pi\pi} < 1835\,\text{MeV}/c^2$). Also shown is a fit with the Δm threshold function and a single Gaussian function for the broken charm contribution.

The residual contamination from this background is estimated by fitting the swapped D^0 masses with a Gaussian function and flat "background" and calculating the number of candidates that fall outside the veto window. This fit is shown in Fig. 5.10. The estimated number of double mis-IDs prior to the veto is estimated by this procedure to be 382 ± 63. After the veto procedure, it is estimated that there are 16 ± 2 candidates originating from decays where a double misidentification has occurred. Therefore, an explicit description of this background can be neglected, and these candidates are treated as part of the combinatorial background model.

Singly Cabibbo-Suppressed (SCS) decays such as $D^0 \to K^-K^+\pi^-\pi^+$, $D^0 \to \pi^+\pi^-\pi^-\pi^+$ can also potentially contribute via a misidentification of a single particle. However, these have negligible contributions within the mass window applied on $m_{K\pi\pi\pi}$, and candidates are not found near the D^0 if the mass hypothesis of one D-meson daughter is swapped. Therefore, no further selection criteria are required.

5.4.2 Broken charm

There is a background from decays where the D^0 has been partially reconstructed or daughters have been misidentified, but matched with the correct slow pion. This background is referred to as *broken charm*. An example process would be $D^0 \to K\pi\eta'(958)[\pi^+\pi^-\gamma]$. This decay will enter into the signal window of $D^0 \to K\pi\pi\pi$, but will be peaked lower in $m_{K\pi\pi\pi}$ than true D^0 decays. However, these backgrounds will peak in Δm. The Δm distribution at lower $m_{K\pi\pi\pi}$ masses is shown in Fig. 5.11, selecting candidates with $m_{K\pi\pi\pi} < 1835\,\text{MeV}/c^2$. A small peak is observed at about

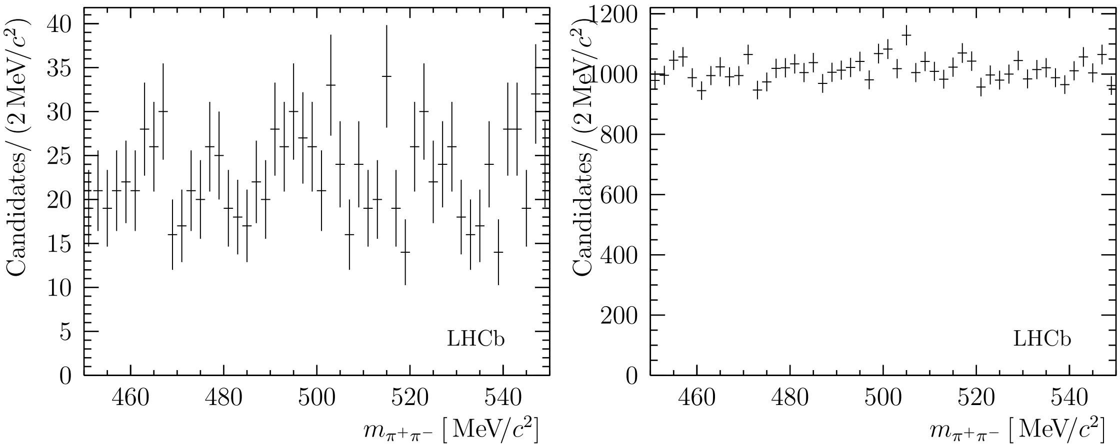

Figure 5.12: Opposite-sign dipion invariant-mass, $m_{\pi^+\pi^-}$, for the WS data sample, around the known K^0_S mass. Both pairs of opposite sign pions are plotted on the same plot. Left: within the signal region. Right: within the sideband of the $m_{K\pi\pi\pi}$ distribution.

145 MeV/c^2, which is consistent with a broken charm background. This distribution is fitted with a combination of a single Gaussian function and a threshold function. This procedure finds 85 ± 27 candidates in the low-mass sideband. The upper-bound on the number of candidates of this category within the $m_{K\pi\pi\pi}$ signal window is then estimated by assuming the distribution of broken charm candidates is flat in $m_{K\pi\pi\pi}$ up to the high end of the signal window. This finds an upper bound of 90 ± 25 candidates. This is an overestimate, as the partially reconstructed background will in general be peaked lower in $m_{K\pi\pi\pi}$, as opposed to being flat. At the upper bound, the fraction of candidates from this source is about 3%, or about 15% of the background. An explicit description of this background is therefore neglected, and it is included as a part of the description of generic combinatorial background.

5.4.3 $D^0 \rightarrow K^0_S K^+ \pi^-$

The decay $D^0 \rightarrow K^0_S K^+ \pi^-$ is singly Cabibbo suppressed, and therefore has a branching ratio approximately 10× that of the WS mode $D^0 \rightarrow K^+\pi^-\pi^-\pi^+$. This decay can feed into the WS sample if the K^0_S flight distance is very short or the quality of the D^0 decay vertex is poor. The opposite-sign dipion invariant-mass should have a narrow peak at the K^0_S mass (497.6 MeV/c^2[34]), therefore this is shown in Fig. 5.12 in both the signal region and in the sidebands of the D^0 mass. No significant peak is observed as this background is heavily suppressed by vertex requirements on the D^0 decay, and hence no further selection requirement is applied.

5.5 Yield extraction

A two-dimensional fit in the $m_{K\pi\pi\pi} : \Delta m$ plane is performed simultaneously between the RS and WS samples in order to determine signal yields and estimate the residual contamination from various sources of background. The plane is shown in Fig. 5.5, with boxes indicating the signal and sideband regions. The signal region in which yields are extracted is defined as:

- $1846.5\,\mathrm{MeV}/c^2 < m_{K\pi\pi\pi} < 1882.5\,\mathrm{MeV}/c^2$,
- $144.65\,\mathrm{MeV}/c^2 < \Delta m < 146.15\,\mathrm{MeV}/c^2$.

Three different categories of decays contribute to the sample, and can be distinguished by their distributions in the $m_{K\pi\pi\pi} : \Delta m$ plane.

Signal: Both the D^* and the D^0 are correctly reconstructed, hence the distributions are peaked in both $m_{K\pi\pi\pi}$ and Δm distributions. This component is modelled using a product of two Cruijff functions [68]. The Cruijff function is a modified version of a Gaussian, with additional parameters to describe the long, asymmetric tails seen in data.

$$\mathcal{P}_S(m_{K\pi\pi\pi}, \Delta m) \propto \exp\left(-\frac{(m_{K\pi\pi\pi}-\mu)^2}{2\sigma^2+\alpha(m_{K\pi\pi\pi}-\mu)^2} - \frac{(\Delta m-\mu')^2}{2\sigma'^2+\alpha'(\Delta m-\mu')^2}\right), \tag{5.1}$$

where $\alpha(')$, $\sigma(')$ have different values either side of the mean value:

$$\sigma, \alpha = \begin{cases} \sigma^L, \alpha^L & m < \mu \\ \sigma^R, \alpha^R & m > \mu. \end{cases} \tag{5.2}$$

Combinatorial: The reconstructed D-meson is a random combination of tracks, and is therefore relatively flat in $m_{K\pi\pi\pi}$ and can be modelled by a first-order polynomial. In Δm, there is a threshold at the pion mass, therefore this is described by a function that explicitly includes this threshold:

$$\mathcal{P}_C(m_{D^0}, \Delta m) \propto (1+2pQ)(Q+1+pQ^2)^a(1+bm_{K\pi\pi\pi}), \tag{5.3}$$

where $Q = \Delta m - \mathrm{m}_\pi$.

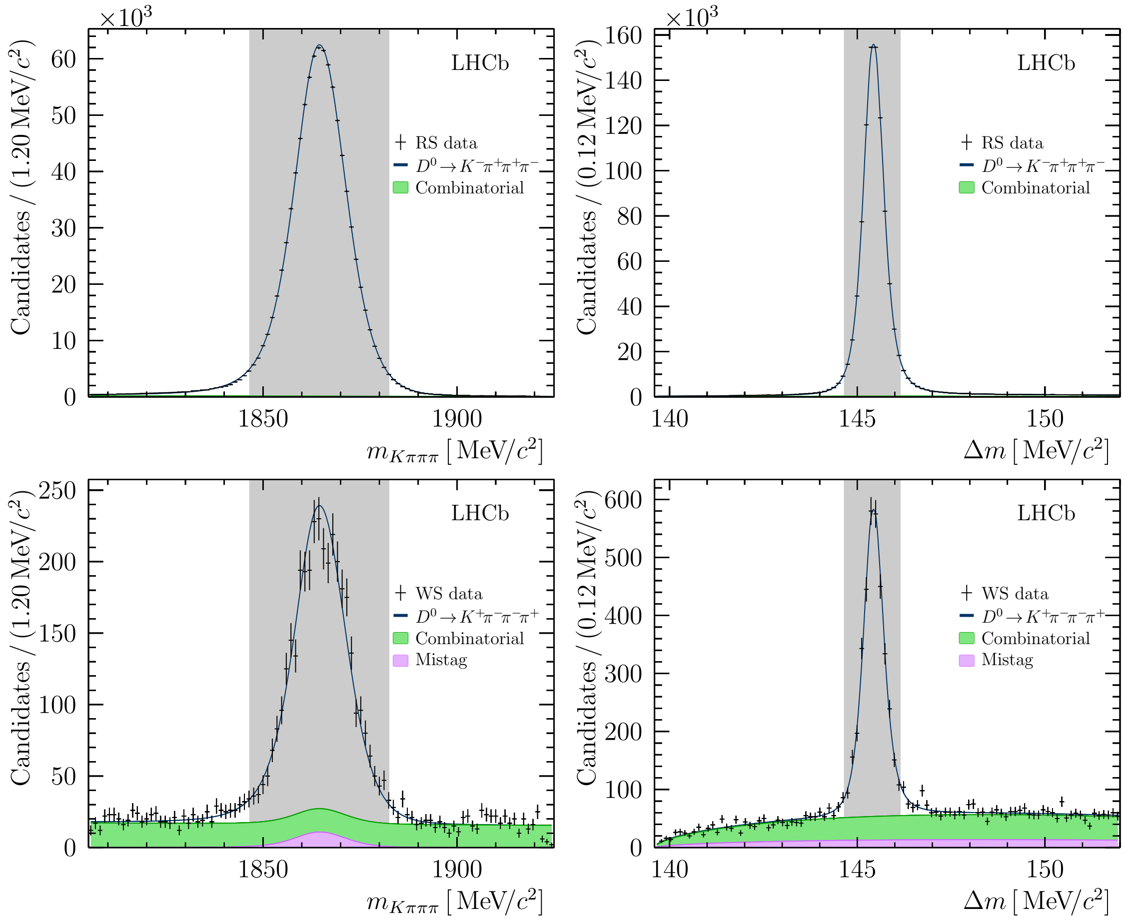

Figure 5.13: Invariant mass and mass difference distributions for RS (top) and WS (bottom) samples, shown with fit projections. The signal region is indicated by the filled grey area, and for each plot the mass window in the orthogonal projection is applied. In each plot, the green area indicates the contribution from combinatorial background.

Mistag: The D meson is correctly reconstructed, but paired with a random slow pion, so it does not form a good D^* candidate. The distribution can therefore be modelled with the same Cruijff function as the signal in $m_{K\pi\pi\pi}$, and a threshold function in Δm.

$$\mathcal{P}_W(m_{D^0}, \Delta m) \propto (1 + 2pQ)(Q + 1 + pQ^2)^a \exp\left(-\frac{(m_{K\pi\pi\pi} - \mu)^2}{2\sigma^2 + \alpha(m_{K\pi\pi\pi} - \mu)^2}\right). \tag{5.4}$$

The individual components are independently normalised, then summed with yields and all of the shape parameters floated. The parameters pertaining to the signal mode are fixed between the RS and WS samples, and the background shapes are allowed to float independently.

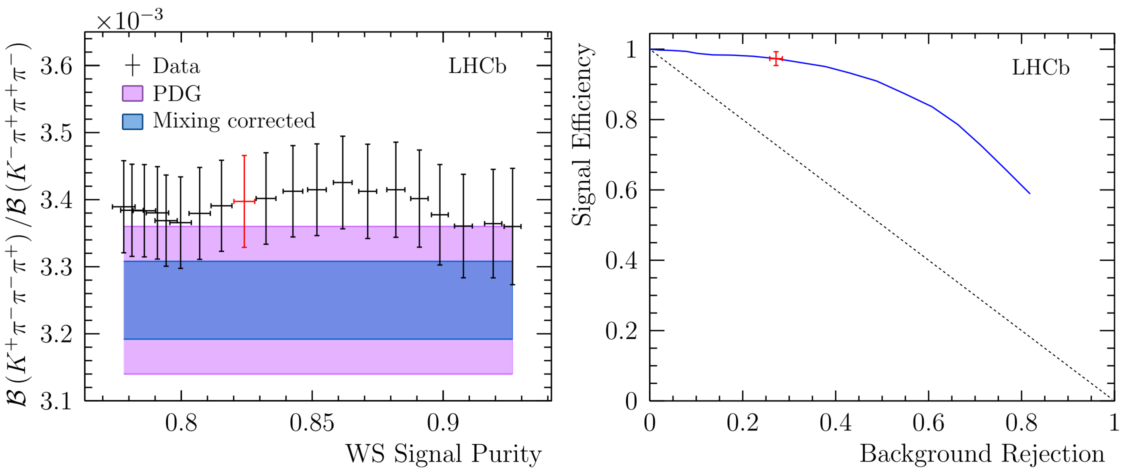

Figure 5.14: Left: Ratio of WS/RS yields as a function of sample purity, obtained by scanning in the requirement on the output of the BDT classifier. The areas show the predicted $\pm 1\sigma$ range taking the ratio of branching from Ref. [34], and from the ratio expected from the D^0 mixing measurement [42] corrected for the decay-time acceptance as described in Sect. 5.6. Right: Background rejection vs signal efficiency relative to the signal and background yields at a BDT cut of -0.2. In both plots, the red marker indicates the values at the optimal requirement of the output of the BDT classifier, which corresponds to -0.14.

The projections of the fit are shown in Fig. 5.13. The fit to the large RS sample is imperfect, however, the purpose of the fit is to constrain the signal shape in the WS sample, for which the agreement is good. As the background contamination in the RS sample is extremely low, a relatively large uncertainty on the level of this contamination does not strongly impact upon the amplitude fit of this mode presented in the next chapter.

Figure 5.14 shows the ratio of signal yields as a function of signal purity to demonstrate that the WS/RS ratio is stable relative to the fit and the selection. Several effects, such as efficiency corrections, are not taken into account here, which can affect the WS and RS differently. The expected ratio is corrected for $D^0\overline{D}^0$ mixing and the decay time acceptance, as described in Sect.5.6, and is shown as a blue band. The PDG value of the ratio is shown as a red band. The efficiency as a function of background rejection is also shown. The nominal working point is selected to be the point where the significance is maximised. This corresponds to a BDT cut of -0.14 .

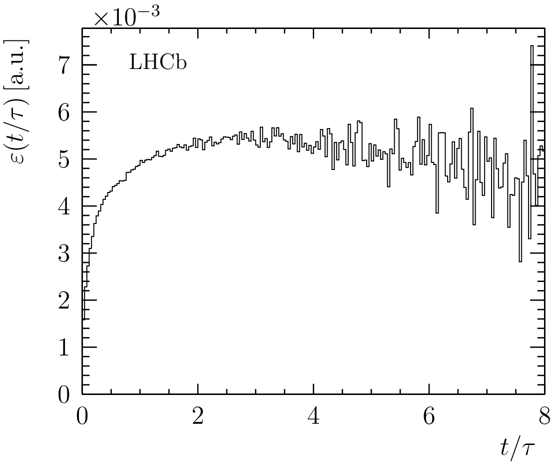

Figure 5.15: Decay time acceptance of RS decays as a function of D^0 candidate proper decay time, taken from 2011 + 2012 RS data sample. The lifetime is calculated constraining the $D^0\mu\pi_s$ vertex. The histogram is normalised to unit area.

5.6 Mixing correction

The WS/RS ratio varies as a function of time due to mixing. The estimate of this ratio integrated over time must therefore be corrected for the acceptance as a function of decay time. The dependence is approximated up to second order in time by:

$$R(t) = (r_{K3\pi})^2 - R_{K3\pi}\left(y\cos(\delta_{K3\pi}) - x\sin(\delta_{K3\pi})\right)\frac{t}{\tau} + (x^2+y^2)\frac{t^2}{\tau^2}, \qquad (5.5)$$

where (x, y) are the charm mixing parameters and $(R_{K3\pi}, \delta_{K3\pi}, r_{K3\pi})$ the hadronic parameters of the $D^0 \to K\pi\pi\pi$ decay. The values of the parameters and the correlations between them are taken from the mixing constrained fit in Ref. [42]. The proper D^0 decay time, τ is taken from the PDG [34] as $0.4101 \pm 0.0015\,\mathrm{ps}$, and the uncertainty on the decay time is assumed to have a negligible effect on the corrected time integrated WS/RS ratio. The decay time acceptance is estimated using the combined 2011 and 2012 RS data sample. It is assumed that the true RS decay time distribution is distributed exponentially according to the proper decay time. It is also assumed that the decay time acceptance between RS and WS decay modes is identical. The estimated decay time acceptance function is shown in Fig. 5.15. The acceptance is reduced at low decay times due to selection requirements involving the impact parameters of tracks, as these variables are strongly correlated with the decay time. The acceptance corrected time integrated WS/RS ratio is therefore given by:

$$R = \int \mathrm{d}t\varepsilon(t)\frac{1}{\tau}e^{-t/\tau}R(t) = (3.26 \pm 0.06) \times 10^{-3}, \qquad (5.6)$$

where $\varepsilon(t)$ is estimated from the histogram in Fig. 5.15. The time integrated ratio without acceptance corrections is given in Ref. [42] as

$$R = (3.22 \pm 0.05) \times 10^{-3}. \tag{5.7}$$

Therefore, there is a slightly less than 1σ shift upwards in the time integrated WS/RS ratio due to decay time acceptance, and hence the WS sample should be relatively typical of decay-time integrated decays. Additionally, the WS/RS ratio at zero decay-time is $(3.014 \pm 0.066) \times 10^{-3}$, the amplitudes for which only contain the pure Cabibbo-suppressed/favoured processes. It is inferred from this that the dominant contribution to the time-integrated WS sample is from the doubly Cabibbo-suppressed amplitude, with the corrections from mixing effects only having a small impact.

5.7 Phase-space acceptance

In order to study the two amplitudes, variations in the acceptance across the phase space due to detector effects and the various stages of the reconstruction must be accounted for. These effects are studied using large samples of simulated events of both WS and RS decay modes, with preliminary models for both signal modes used to generate the D^0 decay. Samples with both neutral and charged B-mesons are generated, as decay chains from both of these contribute significantly to each sample. A variety of detector conditions are simulated such that the simulated events accurately match those in data. The underlying pp event is simulated under both 7 and 8 TeV energies with both 2011 and 2012 conditions. Additionally, the detector response is simulated under both magnet up and magnet down configurations, in order to match the real data taking conditions. This leads to 16 different simulation samples, with the different configurations and the number of events generated for each detailed in Table 5.4. Twice the number of RS events are generated as WS, leading to a simulated sample of roughly 6 million RS candidates and roughly 3 million WS candidates.

The same reconstruction and selection chain is applied to the simulated samples as the data samples, with the exception of particle identification variables associated with the daughters of the D-meson candidate. These variables rely heavily on the RICH detectors, the response of which is poorly described in the simulation, and hence a data-driven reweighting technique[69] is applied to correct for these aspects of the selection requirements.

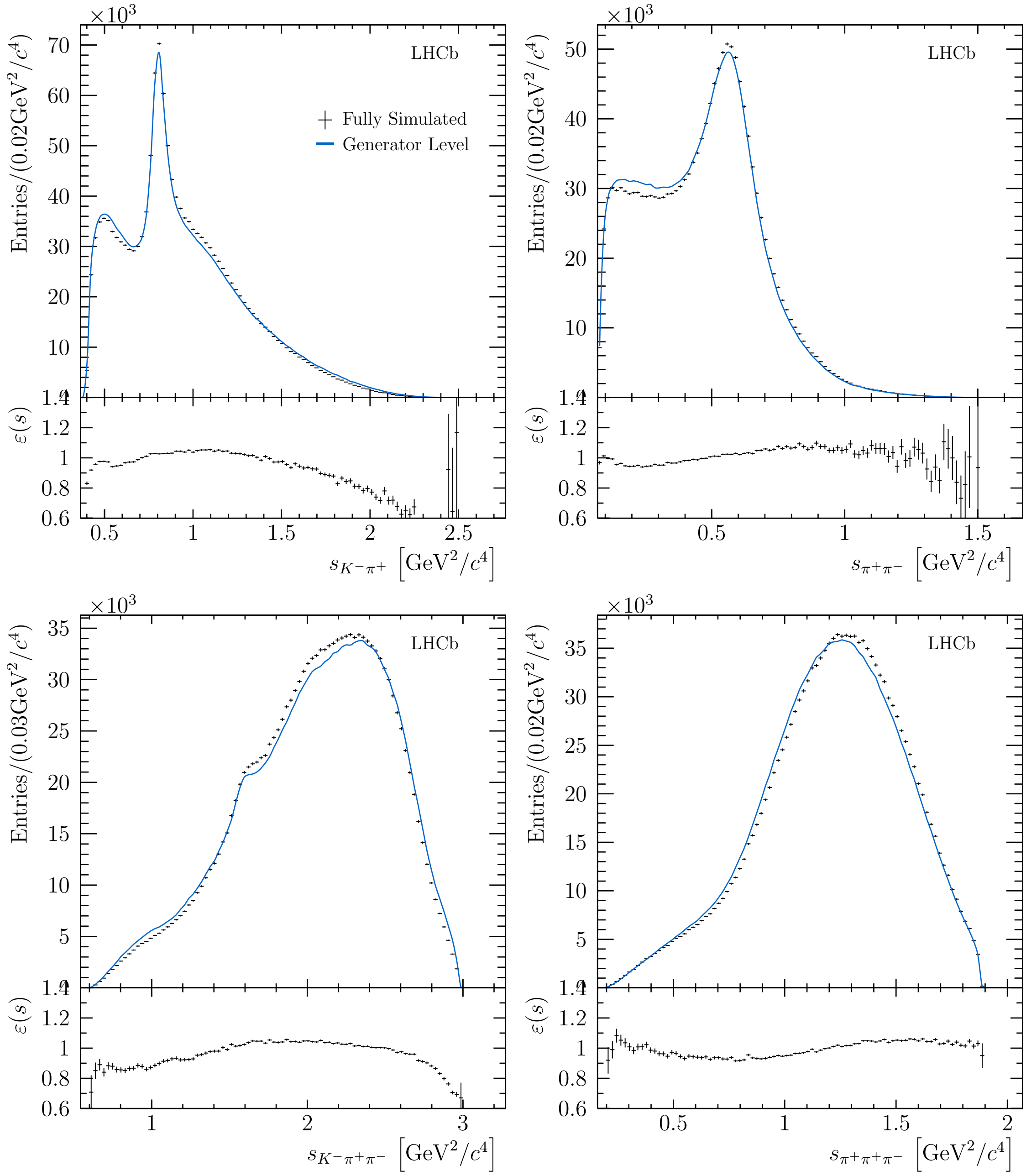

Figure 5.16: Comparison of invariant-mass distributions for the RS mode between fully simulated events with the full selection applied (shown with points) and events at the generator level. Also shown is the ratio of the two distributions.

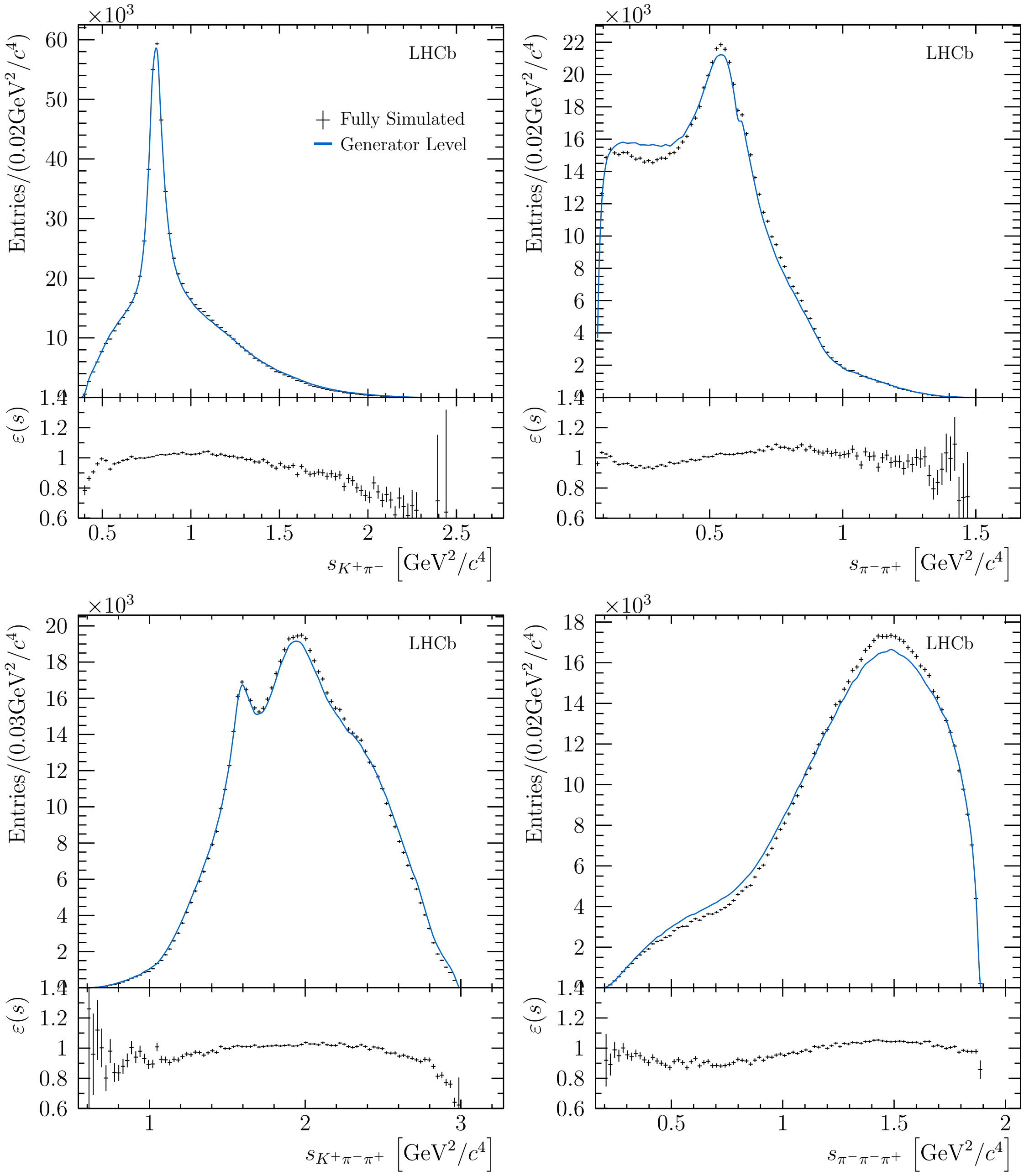

Figure 5.17: Comparison of invariant-mass distributions for the WS mode between fully simulated events with the full selection applied (shown with points) and events at the generator level. Also shown is the ratio of the two distributions.

Table 5.4: Summary of MC samples. The quoted number of candidates is after online / stripping selection only.

Event Type	Year	Polarity	Candidates
$B^0 \to D^*(2010)^+ \, [D^0 \, [K^-\pi^+\pi^+\pi^-] \, \pi^+] \, \mu^- X$	2011	Up	487280
		Down	480360
	2012	Up	962690
		Down	997384
$B^0 \to D^*(2010)^+ \, [D^0 \, [K^+\pi^-\pi^-\pi^+] \, \pi^+] \, \mu^- X$	2011	Up	251424
		Down	264763
	2012	Up	467375
		Down	482520
$B^- \to D^*(2010)^+ \, [D^0 \, [K^-\pi^+\pi^+\pi^-] \, \pi^+] \, \mu^- X$	2011	Up	590189
		Down	532355
	2012	Up	1087148
		Down	1036920
$B^- \to D^*(2010)^+ \, [D^0 \, [K^+\pi^-\pi^-\pi^+] \, \pi^+] \, \mu^- X$	2011	Up	288183
		Down	286721
	2012	Up	529118
		Down	524067
		Total $D^0 \to K^-\pi^+\pi^+\pi^-$	3094171
		Total $D^0 \to K^+\pi^-\pi^-\pi^+$	6174326

The scale of the variation in acceptance across the phase-space can be estimated by comparing the distributions of candidates after the full selection to the distribution the events were generated with. Various distributions are therefore compared between the fully simulated samples, and samples of events that have not been propagated through the detector simulation or selection process. This is shown for four different invariant-mass distributions for the RS and WS simulated samples in Fig. 5.16 and Fig. 5.17, showing both the distributions superimposed and the ratio of the two distributions. The deviations are relatively small, with a maximal deviation of about 30% in the edges of the phase space. The effect of the non-uniformity of the phase-space acceptance is included in amplitude models using these simulated events, using a technique that is described in Sect. 7.1.1.

5.8 Summary

Table 5.5: Signal and background yields for both samples in the signal region, presented separately for each data-taking year.

	Yield		
	Signal	Combinatorial Background	Mistag Background
$D^0 \to K^-\pi^+\pi^+\pi^-$			
2011	$266\,368 \pm 490$	977 ± 10	—
2012	$624\,332 \pm 765$	2475 ± 19	—
Total	$890\,701 \pm 927$	3452 ± 24	—
$D^0 \to K^+\pi^-\pi^-\pi^+$			
2011	875 ± 32	151 ± 3	47 ± 6
2012	2154 ± 51	340 ± 5	108 ± 9
Total	3028 ± 61	491 ± 7	155 ± 11

The final yields of the selection used in the amplitude analysis presented in the later chapters of this thesis are shown in Table 5.5, dividing the samples by data-taking year. The WS sample has a purity of about 82% for 3000 signal candidates, with about a quarter of the background being the result of mistagged favoured decays. The RS sample consists of almost 900,000 signal candidates, with a purity in excess of 99.9%.

6

The Isobar Model

Contents

The amplitudes for a multi-body process can be described in terms of a series of quasi-independent two-body processes. These two-body processes are often referred to as *isobars* and this approximation the *isobar model*. The isobar model has typically been used in describing the three-body decays of pseudoscalars. This is shown pictorially in Fig. 6.1. The isobar can be modelled by a variety of dynamical functions, which are outlined in Sect. 6.1. These dynamical functions describe strong two-body final state interactions (FSI). Typically, the isobar is associated to an intermediate resonance that couples to the two final state particles, and the three-body decay proceeds via a coupling between the initial state, the resonance and the bachelor particle. Higher order topologies that involve interactions between the bachelor and the two final state particles of the isobar are assumed to be

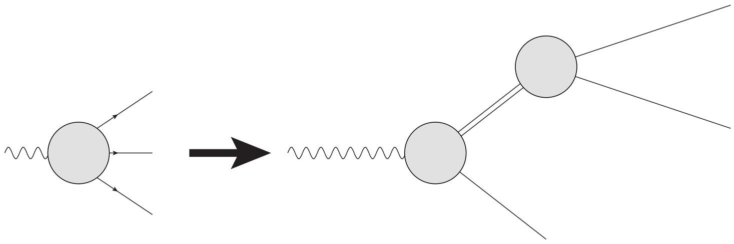

Figure 6.1: Pictorial representation of the isobar model description of the process $P \rightarrow 3P$

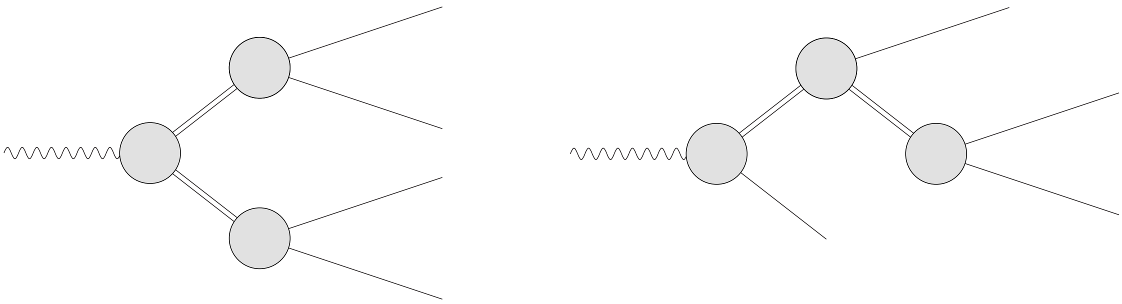

(a) Quasi two-body topology of $P \rightarrow 4P$ (b) Cascade topology of $P \rightarrow 4P$

Figure 6.2: Isobar diagrams for four body decays

negligible. These effects are collectively referred to as *re-scattering*. For each of the dynamical functions that are described in this section, a general overview of the physical considerations that go into the system are described, followed by specific choices that are made for the amplitude analyses of the decay modes studied in the next chapter. In particular, several simplifying assumptions are made to parameterisations in order to reduce the number of degrees of freedom of the system.

Within the approximations of the isobar model, it is straightforward to extend the formalism to include four-body final states, by generalising one of the final-state particles to a second isobar. This gives rise to two distinct decay topologies. The *quasi two-body* topology is shown in Fig. 6.2(a). The initial state decays via a pair of isobars, each of which in turn decays to two particles. The *cascade* topology is shown in Fig. 6.2(b). The initial state decays via an isobar and a stable particle, with the isobar then decaying to three particles via a second isobar and a stable state. Both isobars will in principle carry spin, therefore the description of polarisation and angular momentum is significantly more complicated than in the three body case. A general, covariant approach is adopted, and is described in detail in Sect. 6.2. For the cascade topology, there is an additional complexity from one of the daughters of the first isobar also being an unstable state. The dynamical functions required to describe such a system are developed in Sect. 6.3. A complementary approach to explicitly parameterising the dynamics of one of the quasi two-body systems is to perform a quasi-model-independent partial-wave analysis. This replaces one or more of the dynamical functions used in the fit with a flexible parametrisation that can describe a wide variety of shapes. The formalism for performing such an analysis is described in Sect. 6.4. Section 6.5 discusses how these different components are combined to describe the matrix elements for four-body processes. Section 6.6 gives a brief introduction to how amplitudes are computed in practice, in particular the large size of the RS sample and the relatively complicated nature of the amplitudes presents a significant computational challenge.

6.1 Two-body isobars

Isobars that couple a pair of stable particles are described using two different parameterisations. Narrow, isolated resonant states can be described using the relativistic Breit-Wigner function, which is discussed in Sect. 6.1.1. This is generally the case for vector and tensor states. For scalar states, there are typically multiple broad overlapping resonances, in addition to significant non-resonant scattering amplitudes between the constituent particles of the state. Such a system can be described by the K-matrix formalism, with is discussed in Sect. 6.1.2.

6.1.1 Relativistic Breit-Wigner

Narrow, isolated resonances can be described using the relativistic Breit-Wigner amplitude, which has the form

$$\mathcal{T}(s,q) = \frac{B_L(q,0)\sqrt{k}}{m_0^2 - s - im_0\Gamma(s,q)}, \tag{6.1}$$

where m_0 is the pole mass of the decaying particle, s is the invariant mass squared of the isobar, and q is the momentum transfer, defined as the linear momentum of either decay product in the rest frame of the isobar. An amplitude with $L \geqslant 1$ is dampened at large momentum transfers by the normalised Blatt-Weisskopf form factor, $B_L(q,0)$, which accounts for the finite extent of the decaying meson [70]. These form factors also enhance the amplitude for the decay of a finite sized state near to the kinematic threshold, when compared to the equivalent process of a point-like particle. The total matrix elements, including spin factors, still vanish as $q \to 0$ for decays with orbital angular momentum due to the explicit momentum-scale dependence that naturally emerges from the covariant tensor

Table 6.1: The Blatt-Weisskopf factors for low orbital angular momentum states. The Blatt-Weisskopf radius, d, characterises the interaction radius of the constituent hadrons [70]. The second argument of the Blatt-Weisskopf function, q_0, is the momentum at which the form factor is normalised to unity.

L	$B_L(q, q_0)$
0	1
1	$\sqrt{\dfrac{1+q_0^2d^2}{1+q^2d^2}}$
2	$\sqrt{\dfrac{(q_0^2d^2-3)^2+9q_0^2d^2}{(q^2d^2-3)^2+9q^2d^2}}$

formalism. The normalisation constant, k, approximately normalises the Breit-Wigner function, ignoring effects from the form-factors and running widths. This de-correlates the coupling parameters of a resonance from the lineshape parameters, the mass and width, and hence improves the stability of fits that include such parameters. The normalisation constant is

$$\begin{aligned} k &= \frac{2\sqrt{2}m_0\Gamma\gamma}{\pi\sqrt{m_0^2+\gamma}} \\ \gamma &= m_0\sqrt{m_0^2+\Gamma^2}. \end{aligned} \tag{6.2}$$

The width of the Breit-Wigner, $\Gamma(s, q)$, when the resonance can only decay via a single channel to a quasi two-body final state is

$$\Gamma(s,q) = \frac{\Gamma_0 q m_0}{q_0\sqrt{s}}\frac{q^{2L}}{q_0^{2L}}B_L(q,q_0), \tag{6.3}$$

where q_0 is the linear momentum of either decay product evaluated at the pole mass of the resonance.

6.1.2 K matrix

An example of an amplitude that is not well-described by simple resonant contributions is that of isoscalar $\pi\pi \to \pi\pi$ scattering, and is shown in Fig. 6.3. The first known resonance in this system is the $f_0(980)$ at about $1\,\mathrm{GeV}/c^2$. Rather than a resonance peak being observed at this mass, the amplitude is found to rapidly decrease. Two different effects result in this amplitude: firstly a non-resonant scattering amplitude destructively interferes with the resonant contribution. Secondly, the $f_0(980)$ strongly couples to the KK final state, and hence this *coupled*

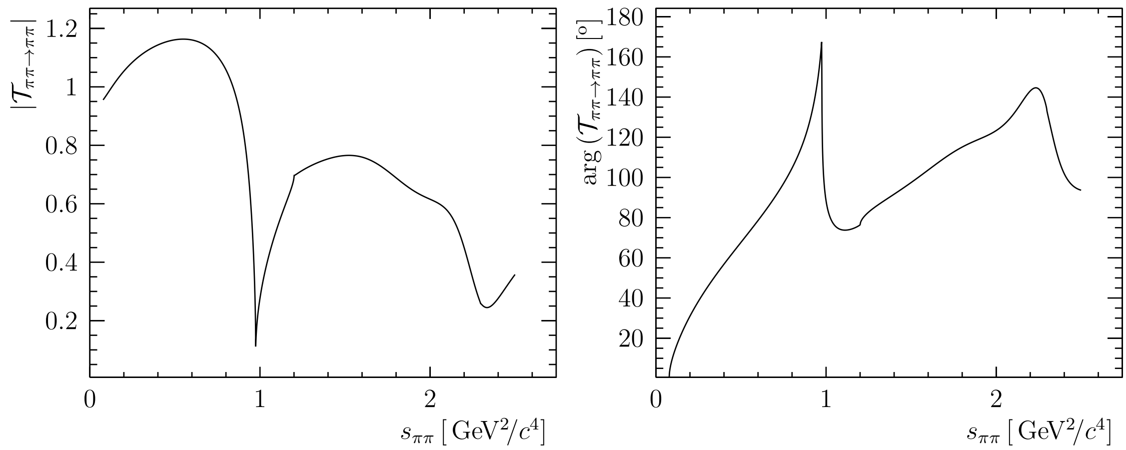

Figure 6.3: Transition amplitude and phase of $\pi\pi \to \pi\pi$ scattering.

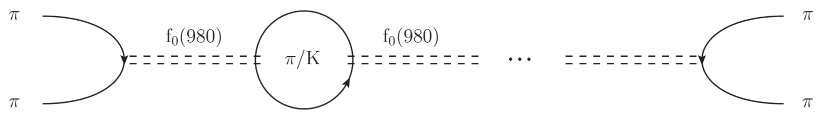

Figure 6.4: Pictorial representation of the contributions from $\pi\pi$, KK to the $f_0(980)$ propagator.

channel also plays an important role in determining the $\pi\pi$ amplitude. At higher masses, further resonances are present such as the $f_0(1370)$, and further coupled final states such as 4π become important. This system is not well described by a simple sum of resonant contributions, in particular this approach can violate constraints from unitarity. An alternative to the simple sum of resonant contributions is the K-matrix formalism, which is constructed to preserve coupled-channel unitarity in the presence of overlapping resonances. A detailed discussion of the formalism is outside the scope of this thesis, but an excellent introduction is given in Ref. [71]. The key result is that the transition matrix of a scattering process $\mathcal{T}$ can be expressed as:

$$\mathcal{T} = \left(I - i\hat{\rho}\hat{K}\right)^{-1}\hat{K}, \tag{6.4}$$

where $\hat{K}$ is a real, symmetric matrix of rank the number of coupled channels considered, known as the *K matrix*. The K matrix is built from a series of real pole terms that generate the resonant content of the system, and polynomial terms that describe non-resonant scattering between hadrons. Within the assumptions of the isobar model, the K matrix provides a universal description of hadron-hadron interactions. The phase-space density matrix, $\hat{\rho}$, is a diagonal matrix with elements the phase-space density of a given channel.

It is instructive to consider the transition amplitude associated with a single pole term and a pair of coupled channels. This is approximately the case for the

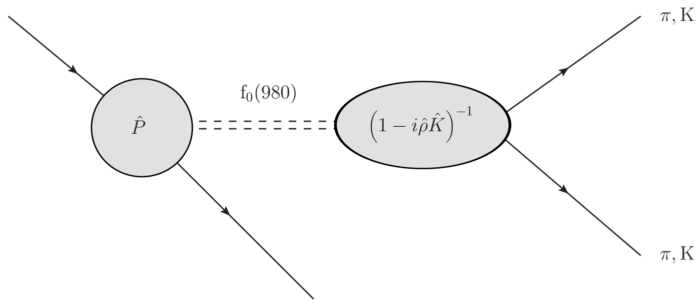

Figure 6.5: Pictorial representation of the production-vector formalism

$f_0(980)$, where the coupled channels to consider are $\pi\pi$ and KK. In this example, the K matrix is a 2×2 matrix with a single pole,

$$K_{ij} = \frac{g_i g_j}{m^2 - s}, \tag{6.5}$$

where m is the pole mass and g_i, g_j characterise the strength of the coupling between channels i, j and the pole. The transition amplitude for $\pi\pi \to \pi\pi$ becomes,

$$\mathcal{T}_{11} = \frac{g_1^2 - i\rho_2 g_2^2}{m^2 - s - i(g_1^2\rho_1(s) + g_2^2\rho_2(s))}, \tag{6.6}$$

where ρ_1, ρ_2 are the elements of the phase-space density matrix for channels $1, 2$. This amplitude is known as the Flattè [72], and has the same form as the Breit-Wigner but with a total width including contributions from both pion and kaon final states. Figure. 6.4 shows a simple picture of the physical interpretation of this formalism, where pion and kaon loops are responsible for generating the finite width of the resonance. When resonances are isolated but multiple coupled channels play a role, the amplitude has the form of a Breit-Wigner but with a total width integrating over all possible final states. The formulation of the running width for three-body final states described in Sect. 6.3 can be considered as the limit of this formalism in the presence of infinite coupled-channels.

The K-matrix prescription described thus far in this chapter deals strictly with scattering amplitudes. The amplitudes considered in this thesis deal with the production rather than scattering processes, which can be described in the production vector, or P-vector formalism. A simple picture of the production vector formalism is shown in Fig. 6.5. The initial state couples to a K-matrix pole, in this example the $f_0(980)$ [1] , and some other final state. The pole is then propagated

[1] This is an oversimplification, as the poles of the K matrix are not associated with physical resonances such as $f_0(980)$, but rather the poles of the T matrix are those that have physical significance

using the K matrix into the final state, in this example either $\pi\pi$ or KK. The initial state is coupled to the K-matrix pole with some coupling strength β, and then the elements of the production vector $\hat{P}$ can be written as:

$$P_i = \frac{\beta g_i}{m^2 - s}. \tag{6.7}$$

There is not a unique prescription for the construction of the production vector, however, it should have the same pole structure as the K matrix itself, such that the amplitude does not vanish at the K-matrix poles. The production amplitude $\mathcal{F}$ can then be written in terms of the P vector as

$$\mathcal{F} = \left(I - i\hat{\rho}\hat{K}\right)^{-1}\hat{P}. \tag{6.8}$$

If there are multiple poles, the P-vector becomes the sum over the poles with different coupling strengths β_i for each pole. When resonances are well separated, the production vector approach tends toward the usual coherent sum of Breit-Wigners, and hence that approach is normally justified when describing vector and tensor degrees of freedom.

$\pi\pi$ S-wave

For the $\pi\pi$ S-wave, the amplitude is constructed by considering five coupled channels: $\pi\pi$, $K\overline{K}$,$\pi\pi\pi\pi$, $\eta\eta$ and $\eta\eta'$. Therefore, it can be described by a 5×5 K matrix. The following parametrisation of the K matrix is commonly used [73]

$$\hat{K}_{ij} = f(s)\left(\sum_{\alpha}\frac{g_i^{\alpha} g_j^{\alpha}}{m_{\alpha}^2 - s} + f_{ij}^{scatt}\frac{1\,\mathrm{GeV}^2 - s_0^{scatt}}{s - s_0^{scatt}}\right), \tag{6.9}$$

where the sum over α is a sum over fives poles. These poles then generate at least five poles in the transition matrix, which are usually associated with the $f_0(980)$, $f_0(1300)$, $f_0(1500)$, $f_0(1750)$, $f_0(1200-1600)$ resonances. In addition to the pole terms, the terms in f_{ij}^{scatt} describe slowly varying scattering contributions. An unphysical kinematic singularity occurs below the $\pi\pi$ production threshold, sometimes referred to as the Adler zero [74]. The term $f(s)$ suppresses this singularity, and has the form

$$f(s) = \frac{1\,\mathrm{GeV}^2/c^4 - s_{A_0}}{s - s_{A_0}}\left(s - s_A\frac{m_\pi^2}{2}\right), \tag{6.10}$$

where the singularity to suppress is at $\sqrt{s} = \sqrt{\frac{s_A}{2}}m_\pi \approx 0.1\,\mathrm{GeV}/c^2$, and the first term is a relatively arbitrary factor that smooths the behaviour of this function, with

$s_{A_0} = -0.15\,\mathrm{GeV}^2/c^4$. All parameters in the K matrix can be fixed from scattering data, with values taken from Ref. [73]. The process-specific production-vector $\hat{P}$ has the same pole structure as the K matrix, such that the physical amplitude does not necessarily vanish at the K-matrix poles, and can be written as

$$\hat{P}_i = \sum_\alpha \frac{\beta_\alpha g_i^\alpha}{m_\alpha^2 - s} + f_i^{prod} \frac{1\,\mathrm{GeV}^2 - s_0^{prod}}{s - s_0^{prod}}. \tag{6.11}$$

This production vector therefore includes both couplings to K-matrix poles, with the strength of the coupling parametrised by β, and direct couplings to the different channels in the K matrix, which is parametrised by couplings f_i^{prod} and a slowly varying polynomial term. These couplings are in general complex, and hence the generic $\pi\pi$ S-wave has 20 degrees of freedom.

This presents a problem for four-body amplitude analyses presented in this thesis, as there are multiple production modes for the $\pi\pi$ S-wave. For example, the production mechanism $D^0 \to K^{*0}[\pi^+\pi^-]^{L=0}$ will have a different set of couplings to $a_1(1260)^+ \to [\pi^+\pi^-]^{L=0}\pi^+$. This results in far too many degrees of freedom, and therefore the following approximations are made to the P-vector:

1. Couplings to poles three, four and five result in small amplitudes within the D^0 decay phase-space, and would require very large production terms to have significant impact within the phase-space, and hence are fixed to zero.

2. Only a direct coupling to one channel other than $\pi\pi$ is considered, which is KK as this has the strongest effect within the phase-space.

This choice reduces the number of free parameters per production mode to eight, which is then tractable. It is noted that the effects of the other channels and poles are still included in the K matrix, but the direct coupling to them is assumed to have small contributions inside the phase space.

$K\pi$ S-wave

The $K\pi$ $I = 1/2$ S-wave up to $\approx 1.5\,\mathrm{GeV}/c^2$ contains both a non-resonant scattering amplitude and the first 0^+ excitation of the kaon, the $K^*(1430)$. The amplitude and phase of the scattering amplitude are shown in Fig. 6.6. The phase rises slowly up to $\approx 1.2\,\mathrm{GeV}/c^2$, which is mostly due to the scattering amplitude and the onset of interference between this amplitude and the resonant contribution.

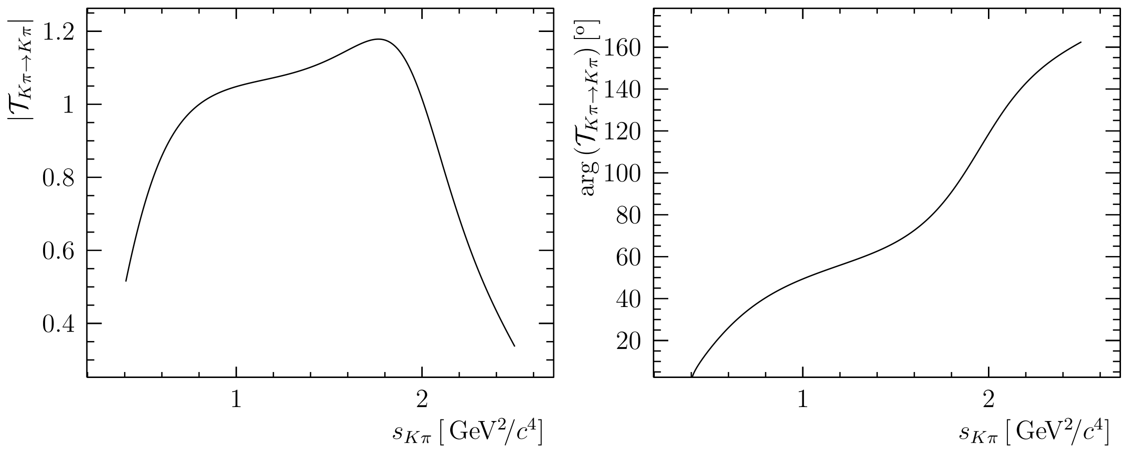

Figure 6.6: The $K\pi$ $I = 1/2$ S-wave scattering amplitude.

Above $1.2\,\mathrm{GeV}/c^2$ the phase rises more rapidly due to the $K^*(1430)$ resonance. At $\approx 1.5\,\mathrm{GeV}/c^2$, other channels such as $K\eta'$ open up and the inelasticity starts to become more important. This system can also be described using a K matrix, consisting of a pair of channels, $K\pi$ and $K\eta'$, where the latter should be considered an effective inelastic channel. The K-matrix elements are written as:

$$K_{ij} = \frac{s - s_{0\frac{1}{2}}}{s_{norm}} \left(\frac{g_i g_j}{s_1 - s} + C_{ij0} + C_{ij1}\tilde{s} + C_{ij2}\tilde{s}^2 \right), \tag{6.12}$$

where the pole $s_1 = 1.7919\,\mathrm{GeV}^2/c^4$, which generates the $K^*(1430)$ resonance. The second-order polynomial terms C_{ijx} describe the non-resonant scattering contribution. Similar to the $K\pi$ S-wave, a kinematic singularity at $s_{0\frac{1}{2}} \approx 0.23\,\mathrm{GeV}^2/c^4$ is removed explicitly. This parametrisation is taken from a study of the $K^-\pi^+$ contribution to $D^+ \to K^-\pi^+\pi^+$ in the amplitude analysis performed by the FOCUS collaboration of this channel [75]. In that analysis, the K-matrix parameters were fitted to a combination of $K\pi \to K\pi$ scattering data from the LASS experiment, with additional constraints from Chiral perturbation theory used to extend the amplitude to threshold.

There is also an $I = 3/2$ scattering amplitude in addition to the $I = 1/2$ amplitude that contributes to the general $K\pi$ S wave. As no resonant contributions are expected with this isospin, and no known sources of inelasticity, the K matrix contains only a scattering component, and can be written as:

$$K_{3/2} = \frac{s - s_{0\frac{3}{2}}}{s_{norm}} \left(D_{110} + D_{111}\tilde{s} + D_{112}\tilde{s}^2 \right), \tag{6.13}$$

where all parameters are also taken from Ref. [75]. The amplitude and phase for this component are shown in Fig. 6.7, and are slowly varying up to $\approx 1.5\,\mathrm{GeV}/c^2$. The amplitude is not well known above this energy.

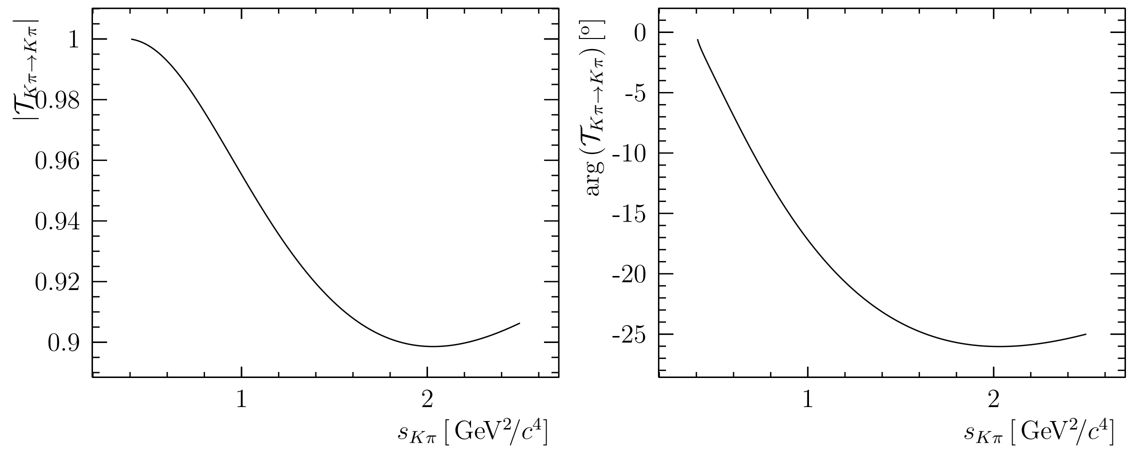

Figure 6.7: The $K\pi$ $I = 3/2$ S-wave scattering amplitude.

The production amplitude for the $K\pi$ S-wave can be constructed using a subtly different picture than the $\pi\pi$ S-wave. The approximation can be made that

$$\hat{K}\hat{P} \approx \hat{\alpha}(s), \tag{6.14}$$

where $\hat{\alpha}(s)$ is a slowly varying complex function. This can be seen from the fact the poles of the P-vector cancel the poles of the K matrix. This allows the insertion of $\hat{K}^{-1}\hat{K}$ into the definition of the transition amplitude in Eq. 6.8, and a re-phrasing of the production vector in terms of the matrix elements from scattering measurements,

$$\mathcal{F}_1 = \alpha_1(s)\hat{T}_{11} + \alpha_2(s)\hat{T}_{12}. \tag{6.15}$$

In this picture, the production process proceeds via the direct production of a $K\pi$ (or $K\eta'$) state. This then scatters using the appropriate elements of the transition matrix into the final state. However, the two pictures are formally equivalent under the approximation in Eq. 6.14.

The advantage of this re-parametrisation is that if the components of α have the same phase, the production amplitude has the same phase-motion as that of a scattering process with the same quantum numbers. This should be true below the inelastic threshold, in the case of $K\pi$ about $1.5\,\mathrm{GeV}/c^2$, and if the effects of re-scattering are negligible. This result is known as Watson's theorem [76]. Conversely, large phase differences at relatively low energies would be clear signs of re-scattering, as the phase-shift from production would no longer match the phase-shift found in scattering.

6.2 Covariant tensor formalism

The effects of spin and orbital angular momentum are calculated using the Rarita-Schwinger formalism, following a similar prescription to that described in Ref. [77]. Spin-matrix elements for quasi two-body processes are constructed in terms of a series of polarisation and pure orbital angular momentum tensors. Consider the decay of particle a that has integer spin J, into particles b and c, which have integer spins s_b, s_c respectively. All three particles have an associated polarisation tensor, $\epsilon^{(a,b,c)}$, which is of rank equal to the spin of the particle. The decay products b, c will also in general have a relative orbital angular momentum l, which is expressed in terms of the pure orbital angular momentum tensor, $L_{\mu...\nu}$, which is of rank l. The matrix element for the decay is

$$\mathcal{M}_{a\to bc} = \epsilon^{(a)*}_{\mu_a...\nu_a}\epsilon^{(b)}_{\mu_b...\nu_b}\epsilon^{(c)}_{\mu_c...\nu_c}L^{(l)}_{\mu_l...\nu_l}G^{\mu_a...\nu_a\mu_b...\nu_b\mu_c...\nu_c\mu_l...\nu_l}, \tag{6.16}$$

where the tensor $G^{\cdots}$ combines the polarisation and pure orbital angular momentum tensor to produce a scalar object. This tensor is constructed from combinations of the metric tensor $g_{\mu\nu}$ and the Levi-Civita tensor contracted with the four-momenta of the decaying particle, $\varepsilon_{\mu\nu\alpha\beta}P^{\mu}$. The second of these tensors is used only if $J-(l-s_b-s_c)$ is odd, and ensures that matrix elements have the correct properties under parity transformations. The matrix element of Eq. 6.16 can also be written by defining the current, $\mathcal{I}$, of the decaying particle,

$$\mathcal{M}_{a\to bc} = \epsilon^{(a)*}_{\underline{\mu}}\mathcal{I}^{(a)\underline{\mu}}, \tag{6.17}$$

where the notation $\underline{\mu} := \mu_a...\nu_a$ has been introduced by this equation to denote sets of Lorentz indices. The current can therefore be written as

$$\mathcal{I}^{(a)\underline{\mu}} = \epsilon^{(b)}_{\underline{\alpha}}\epsilon^{(c)}_{\underline{\beta}}L^{(l)}_{\underline{\gamma}}G^{\underline{\mu\alpha\beta\gamma}} \tag{6.18}$$

The isobar model factorises an N-body decay into a sequence of two-body processes. Each of these quasi two-body decays can be described with a single spin matrix element, and hence the total matrix element is the product of $N-1$ matrix elements,

$$\mathcal{M} = \prod_{i=0}^{N-1}\mathcal{M}_{a_i\to b_i c_i}. \tag{6.19}$$

For example, consider the quasi two-body topology shown in Fig. 6.2(a), labelling the various states by $P \to X\,[ab]\,Y\,[cd]$. The matrix element for this decay is

$$\mathcal{M} = \sum_i \sum_j \mathcal{M}_{P\to X_i Y_j} \mathcal{M}_{X_i \to ab} \mathcal{M}_{Y_j \to cd}, \tag{6.20}$$

where the sums are over the possible polarisations of the intermediate states.

It is preferable to build a generic formulation of the total matrix element for arbitrary topologies, spins and angular momenta, rather than performing an explicit computation for each possible process. A generic approach to computing matrix elements is to introduce a generalised "current" associated with a decaying particle that has absorbed the matrix elements of its decay products, which will be denoted by $\mathcal{J}$. This current can be written in terms of the generalised currents of its decay products as

$$\mathcal{J}^{\underline{\mu}} = L^{(l)}_{\underline{\beta}} G^{\underline{\mu\nu\alpha\beta}} \times \left(\mathcal{S}^1_{\underline{\nu\gamma}} \mathcal{J}_1^{\underline{\gamma}}\right) \times \left(\mathcal{S}^2_{\underline{\alpha\eta}} \mathcal{J}_2^{\underline{\eta}}\right), \tag{6.21}$$

where $\mathcal{S}^{1,2}_{\underline{\mu}}$ is the spin-projection operator of decay products (1,2), which has been used to sum intermediate polarisation tensors, using the definition

$$\sum_i \epsilon_{i\underline{a}} \epsilon_{i\underline{b}}{}^* = \mathcal{S}_{\underline{ab}}. \tag{6.22}$$

The first two projection operations, which are sufficient for describing charm decays, are:

$$\begin{aligned} \mathcal{S}_{\mu\nu}(P) &= -g_{\mu\nu} + \frac{P_\mu P_\nu}{P^2} \\ \mathcal{S}_{\mu\nu\alpha\beta}(P) &= \frac{1}{2}\left(\mathcal{S}_{\mu\alpha} S_{\nu\beta} + \mathcal{S}_{\mu\beta}\mathcal{S}_{\nu\alpha}\right) - \frac{1}{3}\mathcal{S}_{\mu\nu}\mathcal{S}_{\alpha\beta}. \end{aligned} \tag{6.23}$$

This operator projects out the component of a tensor that is orthogonal to the four-momentum, P, and has rank $2J$ for an angular momentum of J. The orbital angular momentum tensors are also constructed from the spin projection operators and the relative momentum of the decay products, Q_a [77], and are written as:

$$\begin{aligned} L_\mu &= -\mathcal{S}_{\mu\nu}(P_a) Q_a^\nu \\ L_{\mu\nu} &= \mathcal{S}_{\mu\nu\alpha\beta}(P_a) Q_a^\alpha Q_a^\beta. \end{aligned} \tag{6.24}$$

The matrix element for a generic cascade of particle decays can then be calculated recursively. In the case of the decay of a spinless particle, the matrix element for the total decay process is identical to the current of the decaying particle. The generalised current can therefore be seen to merely be a convenient device for organising the computation of spin matrix elements, but is not generality associated with the propagation of angular momentum. It is also useful to define the spin-projected currents, $\mathcal{S}_{\underline{\mu\nu}}J^{\underline{\nu}}$, which will be written as $S, V^{\mu}, T^{\mu\nu}$ for (pseudo)scalar, (pseudo)vector and (pseudo)tensor states, respectively.

The spin-projected current for a particle to a pair of decay products in a well-defined orbital angular momentum state can generally be written as a function of the four-momentum of the decay particle, P^{μ}, the four-momentum difference of its decay projects, Q^{μ}, and the spin-projected currents associated with its decay products. Consider the current S associated with the decay of a pseudoscalar to a pair of vector mesons, which have currents V_1^{μ}, and V_2^{ν}. If the vector mesons are in a relative S-wave, the only other tensor available to compute the scalar current is the metric tensor, $g_{\mu\nu}$. The only unique Lorentz scalar combination of these tensors is

$$S = g_{\mu\nu}V_1^{\mu}V_2^{\nu}, \tag{6.25}$$

and hence this is identified as the scalar current. The relations between currents necessary for this thesis are presented in Table 6.2, where the rules have been derived by considering the symmetries of the Lorentz indices, and where relevant the parity properties of the matrix element. All of the rules associated with particles of relatively low spins necessary to describe the decays of pseudoscalars to three or four pseudoscalars are uniquely determined by these constraints up to functions of Lorentz scalars, such as the mass of the decaying particle. This uniqueness property does not generally hold for more complicated decays, for example those that involve a vector meson decaying to a pair of vector mesons. This formulation allows complicated spin configurations to be calculated in terms of a simple and consistent set of rules. The rules are written both with consistent dependencies to clarify their derivations, and in some cases simplified forms are also given. These simplifications typically rely on the symmetry properties of the Levi-Civita tensor and the relationship $\mathcal{S}^{\underline{ab}}\mathcal{S}_{\underline{bc}} = \mathcal{S}^{\underline{a}}_{\underline{c}}$, which is the defining characteristic of a projection operator.

6.2.1 Comparing formalisms

Outside of the covariant tensor formalism, there are considerable ambiguities in defining states with the same spin content and parity, but different orbital quantum numbers. For example, the process $P \to V_1V_2$, where P is a pseudoscalar and V_1,

Table 6.2: Rules for calculating the current associated with a given decay chain in terms of the currents of the decay products. Where relevant, the spin projection operator $\mathcal{S}$ and the orbital angular momentum operators L are those for the decaying particle.

Topology	Current	Simplified current
$S \to [S_1 S_2]$	$S_1 S_2$	
$S \to [V S_1]^{L=1}$	$L^\mu V_\mu S_1$	
$S \to [V_1 V_2]^{L=0}$	$g_{\mu\nu} V_1^\mu V_2^\nu$	
$S \to [V_1 V_2]^{L=1}$	$\varepsilon_{\mu\nu\alpha\beta} P^\mu L^\nu V_1^\alpha V_2^\beta$	$\varepsilon_{\mu\nu\alpha\beta} P^\mu Q^\nu V_1^\alpha V_2^\beta$
$S \to [V_1 V_2]^{L=2}$	$L^{\mu\nu} V_1^\mu V_2^\nu$	
$S \to [T S_1]^{L=2}$	$L^{\mu\nu} T_{\mu\nu} S_1$	
$S \to [T V]^{L=1}$	$L^\mu T_{\mu\nu} V^\nu$	
$S \to [T V]^{L=2}$	$L^{\mu\nu} \varepsilon_{\nu\alpha\beta\gamma} P^\alpha T^{\beta\mu} V^\gamma$	$\varepsilon_{\nu\alpha\beta\gamma} P^\alpha Q^\nu L_\mu T^{\beta\mu} V^\gamma$
$S \to [T_1 T_2]^{L=0}$	$T_1^{\mu\nu} T_{2\mu\nu}$	
$V_\mu \to [S_1 S_2]^{L=1}$	$\mathcal{S}_{\mu\nu} L^\nu S_1 S_2$	$L_\mu S_1 S_2$
$V_\mu \to [V_1 S]^{L=0}$	$\mathcal{S}_{\mu\nu} V_1^\nu S$	
$V_\mu \to [V_1 S]^{L=1}$	$\mathcal{S}_{\mu\nu} \varepsilon^{\nu\alpha\beta\gamma} P_\alpha L_\beta V_{1\gamma} S$	$-\varepsilon_{\mu\alpha\beta\gamma} P^\alpha Q^\beta V_1^\gamma S$
$V_\mu \to [V_1 S]^{L=2}$	$\mathcal{S}_{\mu\nu} L^{\nu\alpha} V_{1\alpha} S$	$L_{\mu\alpha} V_1^\alpha S$
$V_\mu \to [T S]^{L=1}$	$\mathcal{S}_{\mu\nu} L_\alpha T^{\nu\alpha}$	
$V_\mu \to [T S]^{L=2}$	$\mathcal{S}_{\mu\nu} \varepsilon^{\nu\alpha\beta\gamma} P_\alpha L_\beta^\eta T_{\gamma\eta} S$	$-\varepsilon_{\mu\alpha\beta\gamma} P^\alpha Q^\beta T^{\gamma\eta} L_\eta$
$V_\mu \to [T V_1]^{L=0}$	$\mathcal{S}_{\mu\nu} T^{\nu\alpha} V_{1\alpha}$	
$T_{\mu\nu} \to [S_1 S_2]^{L=2}$	$\mathcal{S}_{\mu\nu\alpha\beta} L^{\alpha\beta} S_1 S_2$	$L_{\mu\nu} S_1 S_2$
$T_{\mu\nu} \to [V S]^{L=1}$	$\mathcal{S}_{\mu\nu\alpha\beta} L^\alpha V^\beta S$	$\left(\frac{1}{2}\left(L_\mu S_{\nu\beta} + S_{\mu\beta} L_\nu\right) - \frac{1}{3} S_{\mu\nu} L_\beta\right) V^\beta$
$T_{\mu\nu} \to [V S]^{L=2}$	$\mathcal{S}_{\mu\nu\alpha\beta} \varepsilon^{\alpha\gamma\eta\lambda} P_\gamma L_\eta^\beta V^\lambda S$	$-\frac{1}{2}\left(\varepsilon_{\mu\gamma\eta\lambda} L_\nu + \varepsilon_{\nu\gamma\eta\lambda} L_\mu\right) P^\gamma Q^\eta V^\lambda$
$T_{\mu\nu} \to [T_1 S]$	$\mathcal{S}_{\mu\nu\alpha\beta} T_1^{\alpha\beta}$	

V_2 are vector mesons, has three possible polarisation states. The most general form of the matrix element for this process is given by

$$\mathcal{M}_{P \to V_1 V_2} = V_1^\mu V_2^\nu \left(F_0 g_{\mu\nu} + F_1 \varepsilon_{\mu\nu\alpha\beta} P_1^\alpha P_2^\beta + F_2 P_{1\nu} P_{2\mu} \right), \qquad (6.26)$$

where V_1^ν, V_2^μ are the currents associated with the decay of vector meson 1 and 2, and P_1^μ, P_2^ν the corresponding four-momenta. The terms $F_{0,1,2}$ can generally be functions of Lorentz scalars such as the masses of the vector mesons or the decaying pseudoscalar meson, and hence can be described as "form-factor-like". In the formalism used in the amplitude analyses of $D^0 \to K^-\pi^+\pi^+\pi^-$ [78] and

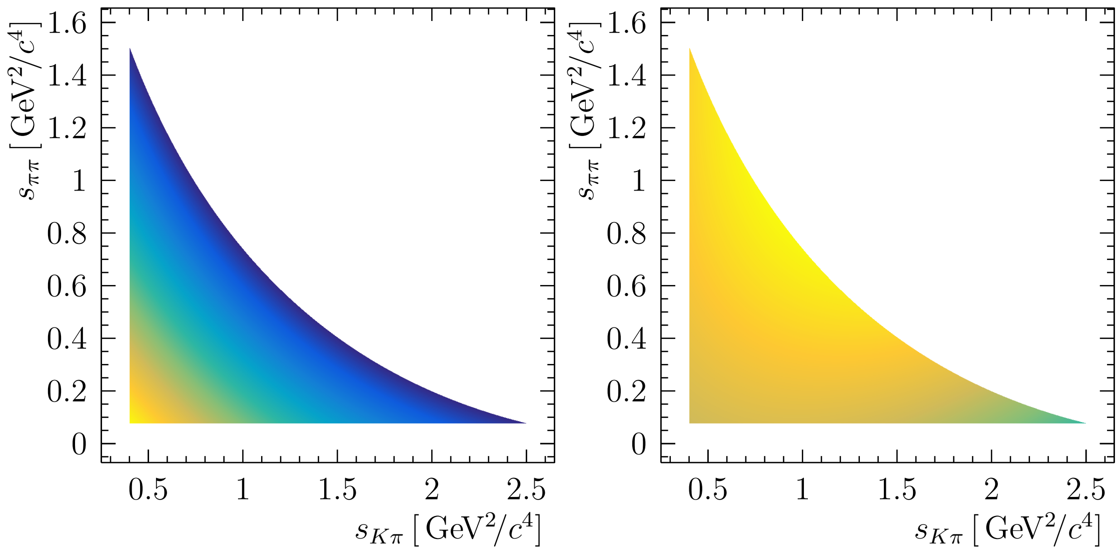

Figure 6.8: The F_0^D (left) and F_2^D (right) dependence on $s_{K\pi}$ and $s_{\pi\pi}$ in the covariant tensor formalism. Note that in the area of the resonances of interest, i.e. the $\rho(770)$ and the $K^*(892)^0$, the variation is small.

$D^0 \to K^+K^-\pi^+\pi^-$ [79], performed by the Mark III and CLEO collaborations respectively, the F_0 term has been referred to as the S-wave ($L = 0$), and the F_2 as the D-wave ($L = 2$). The F_1 term corresponds to the P wave ($L = 1$), and is clearly distinguished by being odd under the parity transformation, with the differences between parity even and parity odd spin factors discussed further in Sect. 6.2.2. It is noted in Ref. [79] that what is defined as the D wave is in fact a superposition of S and D wave. In the covariant tensor formalism, the D wave contains both F_0 and F_2 terms. The S wave only contains an F_0 term. In previous analyses, there is typically a large interference term between S and D wave. By defining in terms of the orbital angular momentum operators, the waves are constructed orthogonal to each other when phase space is extended to infinity. Hence, the interference terms between the different orbital states are inherently suppressed. It is important to note that this choice of basis is not related by a linear transformation, due to different dependence on the vector masses in F_0,F_2. Previously, it has been assumed that these are constants. For a term to be form-factor-like, it is necessary and sufficient that the term only depends on s, s_{V_1}, s_{V_2} where $\sqrt{s}$ is the mass of the decaying particle and $\sqrt{s_{V_1,V_2}}$ are the masses of the two vector states. The form factors therefore result in distortions of the lineshapes of the two vectors, but do not strongly affect the polarisation structure. The dependence on s, s_{V_1}, s_{V_2} can be explicitly calculated in the covariant tensor formalism. The S-wave is unchanged, and therefore F_0^S is a constant. For the D-wave matrix element, the co-efficients are given by

$$\begin{aligned} F_0^D &= \frac{1}{3s}\left(2(s_{V_1}+s_{V_2})s^2 - s^2 - (s_{V_1}-s_{V_2})^2\right) \\ F_2^D &= \frac{1}{3s^2}\left(4(s_{V_1}-s_{V_2})^2 - 2s^2 - s^2(s_{V_1}+s_{V_2})\right). \end{aligned} \tag{6.27}$$

The variation of these factors for the example $D^0 \to K^*[K^-\pi^+]\rho[\pi^+\pi^-]$ is shown in Fig. 6.8 in the two dimensional plane of $s_{K\pi}$ vs. $s_{\pi\pi}$. These form factors vary rather slowly across the phase-space when compared to other features in the $s_{K\pi}, s_{\pi\pi}$ plane, which will generally have relatively narrow peaks associated with the two vector resonances.

6.2.2 Parity

Four-body weak decays can occur via amplitudes that are both odd and even under the parity transformation. Consider the S-wave and P-wave contributions to the two-body vector-vector process $P \to V_1 V_2$. The matrix element for the S-wave is

$$\mathcal{M}_S = \left(-Q_{V_1} + \frac{P_{V_1}\cdot Q_{V_1}}{P_{V_1}^2}P_{V_1}\right)^{\mu}\left(-Q_{V_2} + \frac{P_{V_2}\cdot Q_{V_2}}{P_{V_2}^2}P_{V_2}\right)_{\mu}, \tag{6.28}$$

where P_{V_1}, P_{V_2} are the four momentum of each vector meson, and Q_{V_1},Q_{V_2} are the momentum difference between the decay products of each of the vector mesons. This matrix element involves exclusively contractions of proper vectors, the four momenta, and hence is even under parity. The matrix element for the P-wave is

$$\mathcal{M}_P = \varepsilon_{\mu\nu\alpha\beta}P_{V_1}^{\mu}P_{V_2}^{\nu}Q_{V_1}^{\alpha}Q_{V_2}^{\beta}. \tag{6.29}$$

How this matrix element acts under parity can be made clear by transforming to the frame where the first vector meson is at rest. In this frame, the matrix element is

$$\mathcal{M}_P = \sqrt{s_{V_1}}\mathbf{p}_{V_1}\cdot(\mathbf{q}_{V_1}\times\mathbf{q}_{V_2}), \tag{6.30}$$

where lower case quantities are three-vectors evaluated in this reference frame. Therefore, this matrix element is odd under parity. The general amplitude contains a superposition of the amplitudes for different orbital angular momentum states, and therefore the probability density will contain a mixture of P-even and P-odd terms:

$$|\mathcal{M}|^2 = |\mathcal{M}_S|^2 + |\mathcal{M}_P|^2 + 2\mathcal{R}e\left(\mathcal{M}_S\mathcal{M}_P^*\right), \tag{6.31}$$

and therefore interference between P-even and P-odd amplitudes can result in observable parity asymmetries. These asymmetries can only be observed in restricted regions of phase space as the interference terms vanish when integrating over the entire space.

6.3 Three-body isobars

The dynamical functions discussed in the previous sections describe the final state interactions of a pair of stable hadrons. Consider the case of a cascade decay where rather than two stable particles, a resonance decays to three particles via an additional intermediate isobar. Using the decay $a_1(1260)^+ \to \rho[\pi^+\pi^-]\pi^+$ as an example, the simplest model of this system would assume the ρ is a stable particle, and evaluate the width as given in Eq. 6.3 at the pole mass of the ρ, with a threshold in the width at $\sqrt{s} = m_\rho + m_\pi$. This threshold results in a cusp in the amplitude, which is unphysical as the threshold should be smeared over the finite width of the ρ meson, resulting in a structure known as a *woolly cusp* [80].

A more complete treatment therefore considers the running width to be due to an infinite number of coupled channels, each to an effective ρ meson of a slightly different mass. This is equivalent to integrating over the possible three-body phase-space of the final state particles in the decay. This model therefore assumes that the interactions of the three body final state can be accounted for using only the width of the decaying state,

$$\Gamma(s_R) \propto \int \frac{d^3p_a}{(2\pi)^3 2E_a}\frac{d^3p_b}{(2\pi)^3 2E_b}\frac{d^3p_c}{(2\pi)^3 2E_c}|\mathcal{M}_{R\to abc}|^2\delta(\sqrt{s_R}-(E_a+E_b+E_c))\delta(\mathbf{p}_a+\mathbf{p}_b+\mathbf{p}_c), \tag{6.32}$$

where $\mathcal{M}_{R\to abc}$ is the matrix element for the three-body decay. It is assumed that this can also be calculated using the isobar model. The integral in Eq. 6.32 can be reexpressed as a Dalitz-like integral as only spin-averaged matrix elements are considered. In terms of the invariant mass-squared of the ab and bc systems, s_{ab} and s_{bc} respectively, the integral can be expressed as

$$\Gamma(s_R) \propto \frac{1}{s_R}\int ds_{ab}ds_{bc}|\mathcal{M}_{R\to abc}|^2. \tag{6.33}$$

Multiple intermediate isobars contribute to the decay of most resonances. Consider again the case of the $a_1(1260)^+$. Three intermediate states are known to contribute below the $KK\pi$ threshold:

$$\begin{aligned} a_1(1260)^+ \to & \rho(770)^0[\pi^+\pi^-]\pi^+ \\ & [\rho(770)^0[\pi^+\pi^-]\pi^+]^{L=2} \\ & [\pi^+\pi^-]^{L=0}\pi^+, \end{aligned}$$

where the dominant contribution is from $a_1(1260)^+ \to \rho\pi^+$. Following the formalism in Ref. [81], the matrix element is expressed in terms of currents.

$$\mathcal{M}_{\rho\pi^+} = \varepsilon_a^\mu \left(j_\mu + j'_\mu\right) = \varepsilon_a^\mu \mathcal{M}_\mu^1 \tag{6.34}$$

where $\varepsilon_a^{\mu}(P)$ is the polarisation tensor of the $a_1(1260)^+$. The hadronic current is j_μ and j'_μ the current under the exchange of identical pions. These are composed of the spin "currents" discussed in Sect. 6.2 dressed with two body dynamical functions such as the relativistic Breit-Wigner $\mathcal{T}_{RBW}$ or a K-matrix $\mathcal{T}_{\pi\pi}$ and form factors. For example, the hadronic current for the $a_1(1260)^+ \to \rho\pi^+$ is written as:

$$j^{\mu}_{\rho\pi} = \mathcal{T}_{RBW}(s_\rho)F(q^2)L^{\mu}(p_\rho, q_\rho), \tag{6.35}$$

where the form factor, $F(q^2)$, is a function of the linear momentum of the bachelor pion in the rest frame of the $a_1(1260)$, and takes the form

$$F(q^2) = e^{-R^2q^2/2}, \tag{6.36}$$

where R is related to the finite size of the a_1. This form factor is required such that the width does not diverge as $s \to \infty$. The definitions of spin currents are given in Sect. 6.2. For completeness, the hadronic currents for the other two intermediate states are:

$$\begin{aligned} j^{\mu}_{[\pi\pi]^{L=0}\pi} &= \mathcal{T}_{\pi\pi}(s_{\pi\pi})F(q^2)L_1^{\mu\nu}(p_a, q_a) \\ j^{\mu}_{[\rho\pi]^{L=2}} &= \mathcal{T}_{RBW}(s_\rho)F(q^2)L_2^{\mu\nu}(p_a, q_a)L_{1\nu}(p_\rho, q_\rho). \end{aligned} \tag{6.37}$$

The total matrix element is the coherent sum of these matrix elements, with the appropriate coupling constants g_i.

$$\mathcal{M} = \varepsilon^{\mu} \sum_i g_i \left(j^i_\mu + j^{i\prime}_\mu \right), \tag{6.38}$$

where the sum is over the three states listed above. Taking the modulus-square and summing over the polarisations of the initial state results in

$$|\mathcal{M}|^2 = \mathcal{S}^{\mu\nu} \sum_{ij} g_i g_j^* \left(j^i_\mu + j^{i\prime}_\mu \right) \left(j^j_\nu + j^{j\prime}_\nu \right)^*, \tag{6.39}$$

where the polarisation tensors ε_μ have been summed using the definition of the projection operator $\mathcal{S}_{\mu\nu}$.

In the limit where the intermediate isobar is narrow, the three-body treatment is well approximated by a relativistic Breit-Wigner function, taking the intermediate isobar to be a stable state. For example, the only significant decay chain of the $K_2^*(1430)^-$ resonance is:

$$K_2^*(1430)^- \to \underbrace{K^*(892)^0}_{\hookrightarrow K^-\pi^+}\pi^-,$$

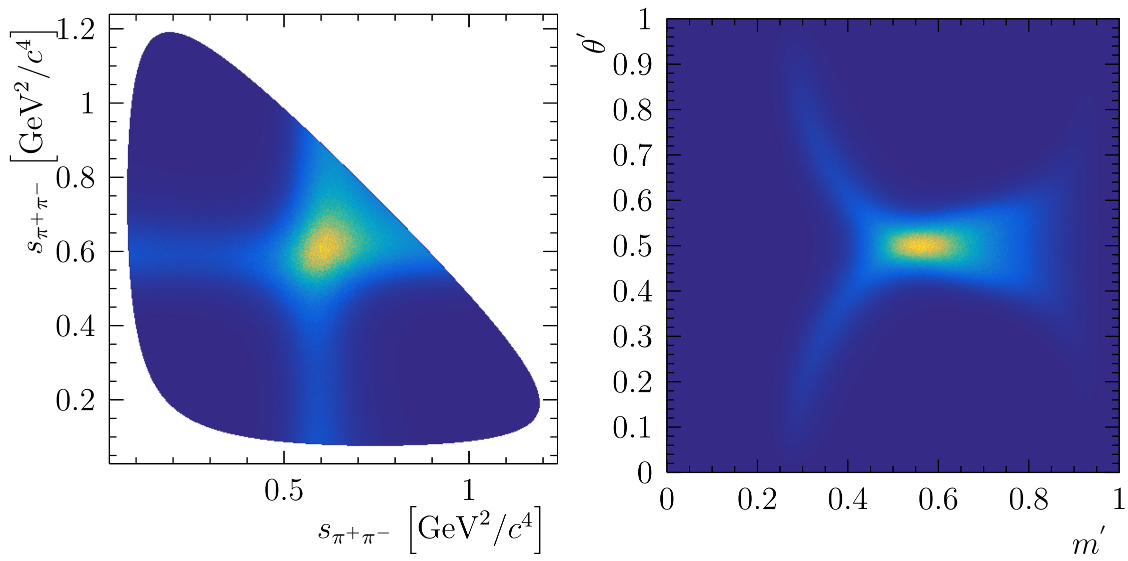

Figure 6.9: Square Dalitz transformation for the spin averaged $a_1(1260) \to \rho\pi$ decay, where the colour scale indicates the decay rate.

and therefore the width of the $K_2^*(1430)^-$ is well approximated by Eq. 6.3 due to the relative narrowness of the $K^*(892)^0$ state.

The integral in Eq. 6.33 must be computed numerically for a general matrix element. It is convenient to re-express the Dalitz coordinates in terms of the so-called square Dalitz coordinates. These have the advantage that the integral is over the unit square, rather than over the somewhat complicated boundary of the regular Dalitz plot. The square Dalitz coordinates are defined as

$$\begin{aligned} m &= \frac{1}{\pi}\mathrm{acos}\left(\frac{2(\sqrt{s_{ab}} - m_{min})}{m_{max} - m_{min}} - 1\right) \\ \theta &= \frac{1}{\pi}\mathrm{acos}\left(\frac{\mathcal{S}_{\mu\nu} p_a^\mu p_c^\nu}{\sqrt{\mathcal{S}_{\mu\nu} p_a^\mu p_a^\nu}\sqrt{\mathcal{S}_{\mu\nu} p_c^\mu p_c^\nu}}\right), \end{aligned} \tag{6.40}$$

where m_{min}, m_{max} are the minimal and maximal values of $\sqrt{s_{ab}}$, the invariant mass of the ab system. The spin-one projection operator of the ab system, $\mathcal{S}_{\mu\nu}$ contracting a pair of four-vectors is equivalent to the dot-product of the corresponding three momenta evaluated in the rest frame of the ab system. Therefore, θ is proportional to the angle between a and c in the rest frame of the ab system, which is the definition of the helicity angle. The Jacobian of this transformation is

$$J = 2\pi^2 |\mathbf{p}_a^\star||\mathbf{p}_c^\star| \sqrt{s_{ab}}(m_{max} - m_{min}) \sin(\pi m) \sin(\pi\theta), \tag{6.41}$$

where $\mathbf{p}_x^\star$ is the three momentum of particle x in the rest frame of ab. An example of the square Dalitz transformation is shown in Fig. 6.9, for the process

$a_1(1260) \to \rho[\pi\pi]\pi$. The regular Dalitz plot is shown in Fig. 6.9(a), with the clear ρ contribution in both combinations of $\pi^+\pi^-$. The result of transforming onto the square Dalitz coordinates is shown in Fig. 6.9(b), where the resonance region has now migrated to the centre of the space. The symmetric pattern in the angular co-ordinate θ' is a consequence of the spin of the decaying ρ meson. After this transformation, Eq. 6.33 becomes

$$\Gamma(s_R) = \frac{1}{s_R} \int_0^1 \int_0^1 J(m,\theta) dm d\theta \left|\mathcal{M}_{R\to abc}(m,\theta)\right|^2 . \tag{6.42}$$

In order to calculate the width as a function of mass the integral is computed at a fixed set of points in s_R, and then approximated everywhere else by interpolating these points using cubic splines.

6.4 Quasi model-independent formalism

In addition to the explicit parameterisations of isobars described in the previous sections, it is useful to be able to examine the behaviour of an amplitude without making assumptions about the shape of the dynamical function. This is referred to as *quasi* model-independent as the extraction of the phase-behaviour of an amplitude relies on the other components of the model being described accurately. The formalism for performing such an analysis follows a method first used by E791 [82, 83] in studying the $K^-\pi^+$ S-wave contribution to $D^+ \to K^-\pi^+\pi^+$ decays.

Typically a dynamical function will depend on the squared invariant mass of its daughters, which will be labelled by x for generality. The range of parameter x is divided into N segments of equal length. The function F_n in segment n is then parametrised by a third order polynomial,

$$F_n(x) = a_n + b_n(x - nL) + c_n(x - nL)^2 + d_n(x - nL)^3, \tag{6.43}$$

where L is the length of each segment, and the co-efficients a_n, b_n, c_n, d_n differ between the segments. The co-efficients can be expressed in terms of the value of the function, a_n, at the connecting points between the segments by applying continuity and differentiability up to second order. The values of the function at the connecting points, a_n are then free parameters to be determined in a fit. This parametrisation is known as a *cubic spline*, and is flexible enough to describe a wide range of smooth functions. The spline will not be able to reproduce features that are smaller than the spacing between the segments. For a general complex amplitude, the real and imaginary parts of the amplitude are treated as two independent cubic splines.

6.5 Matrix elements

The components of the isobar model are combined to form the Lorentz invariant matrix elements of the four-body process. Two examples of how this is done are discussed in this section.

The quasi two-body process $D^0 \to K^*\rho$ is shown in Fig. 6.10. As there are three (S,P,D) possible orbital angular momentum configurations of the two vector mesons, therefore there are three independent complex coupling coefficients between the initial state, D^0, and the $K^*\rho$ state, g_S, g_P and g_D. The couplings between the decaying state and these intermediate states are generally the main parameters of an amplitude fit. The total matrix element for $D^0 \to K^*\rho$ coherently sums the different orbital components:

$$\mathcal{M}_{K^*\rho} = \left(g_S g_{\mu\nu} + g_P P_D^\alpha Q_D^\beta \varepsilon_{\alpha\beta\mu\nu} B_1(q_D, 0) + g_D L_{\mu\nu} B_2(q_D, 0)\right) j^\mu_{K^*} j^\nu_\rho, \tag{6.44}$$

where $B_L(q_D, 0)$ are normalised Blatt-Weisskopf factors associated with the decay of the D^0, detailed in Table. 6.1. The currents $j^\mu_{K^*}, j^\nu_\rho$ describe the propagation and decay of the K^* and ρ resonances, namely by the Breit-Wigner function and the $L = 1$ orbital operator.

The second example to consider is the cascade process $D^0 \to K_1(1270)^-\pi^+$ where the $K_1(1270)$ decays via:

$$\begin{aligned} K_1(1270)^- \to& \rho K^- \\ & K^*\pi^-, \end{aligned}$$

where the other couplings of the $K_1(1270)$ are neglected in this section for brevity. The amplitude for this process is then given by:

$$\mathcal{M}_{K_1\pi} = g_{K_1\pi} B_1 L_\mu(p_D, q_D) j^\mu_{K_1}, \tag{6.45}$$

where $g_{K_1\pi}$ is the complex coupling coefficient between the D^0 and this isobar, sometimes referred to as the production coupling. The current, $j^\mu_{K_1}$, describes the propagation and decay of the $K_1(1270)$ meson.

$$j^\mu_{K_1} = \mathcal{T}_{K_1}\left(g_{\rho K} j^\mu_{\rho K} + g_{K^*\pi} j^\mu_{K^*\pi}\right), \tag{6.46}$$

where $\mathcal{T}_{K_1}$ is the dynamic function associated with the three-body isobar, discussed in Sect.6.3. The currents associated with each of the intermediate states, $j_{\rho K}$ and $j_{K^*\pi}$, are coherently summed with complex co-efficients $g_{\rho K}$ and $g_{K^*\pi}$, and are

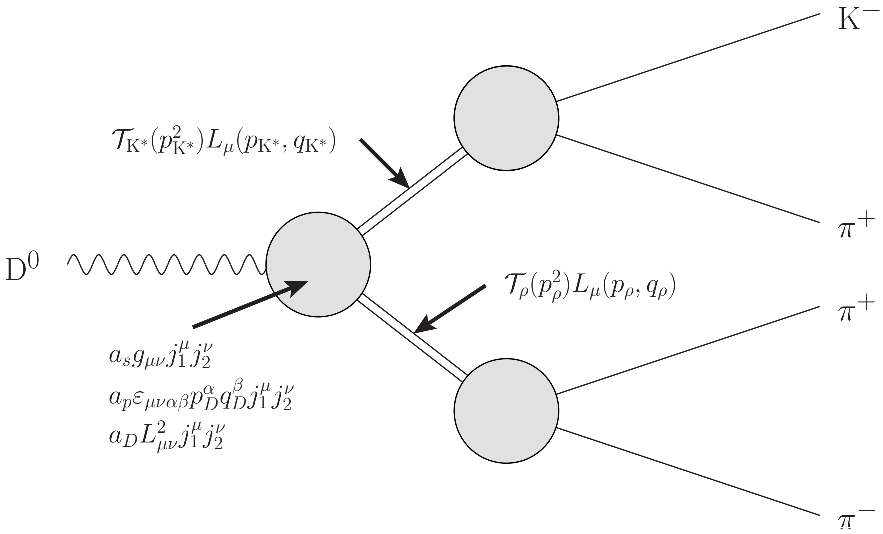

Figure 6.10: Diagram from the quasi two-body process $D^0 \to K^*\rho$

referred to as the decay co-efficients of the $K_1(1270)$. The total matrix element is invariant under a simultaneous transformation of the production coupling and all decay couplings and hence one of the couplings is redundant and can be fixed. By convention, the largest of the decay couplings is fixed along the real axis, so $g_{\rho K} = 1$ in the case of $K_1(1270)$. The production coupling and the other decay couplings are then defined with respect to this choice. It is noted that this is a convention and does not make stricter assumptions about the factorisability of coupling constants. Explicitly, interactions between the bachelor pion and the $K_1(1270)$ daughters potentially alter the coupling coefficients significantly. This would result in different decay couplings measured in different production modes of the $K_1(1270)$. However, within the assumptions of the isobar model, the decay couplings of the $K_1(1270)$ should be universal, and hence this factorisability assumption is imposed when studying the $D^0 \to K^+\pi^-\pi^-\pi^+$ sample. For example, in the case of the $K_1(1270)$ it is assumed that the decay couplings are identical between production modes $D^0 \to K_1(1270)^+\pi^-$ and $D^0 \to K_1(1270)^-\pi^+$. A comparison of the couplings between different production modes of a resonance could lead to some novel tests of the assumptions of the isobar model, but such work is outside of the scope of this thesis.

6.6 AmpGen framework

The large sizes of the RS data set and simulation samples mean an efficient method for computing amplitudes is crucial in performing fits in a reasonable amount of time. An additional challenge in the case of studying four-body final states is that there are many different spin matrix elements, as well as many different combinations of propagators. It is clearly impractical to code each possible amplitude by hand. Therefore, amplitudes must be described within some abstraction layer that calculates the complex function of the final state momenta and various constants, such as the masses and widths of the resonances. These abstraction layers are typically inefficient, as they will involve many function invocations and various complex memory operations. Flexibility in the definition of the amplitude is often achieved via the use of virtual functions, that if the PDF is evaluated many times can incur a significant performance penalty.

The goal is hence to achieve maximum flexibility and modularity in defining the amplitude, while not incurring significant run-time penalties when compared to hand-written code. This is achieved by defining the algebraic expressions that make up the components of the amplitude in the form of *binary expression trees*, where the underlying representation of the tree is a series of C++ objects. Before the amplitude is evaluated, this expression tree is converted into efficient source code, compiled and then dynamically linked against the executable. As the software generates the code that evaluates the amplitude, this technique is a form of *metaprogramming*. There are several advantages to the meta-programming approach other than the speed to evaluation:

1. The definition of the amplitude is flexible. The same generating code can be used for any number of final-state particles, including final-state particles with intrinsic spin. This flexibility incurs no significant runtime penalties, as it is partitioned from the function evaluation by the compilation process.

2. Inputs to the function can be mapped from event data or constants like resonant masses and widths. These are then packed in a cache friendly way, without having to deal with such optimisations when writing the code.

3. Compiled models can be distributed as part of the documentation, therefore it is straightforward to use the results of a complicated model without having to rely on a complicated framework. This is useful for interfacing with Monte Carlo generators, and is how these models are integrated into the LHCb simulation framework.

This approach has been implemented in the AmpGen Fitter, which is loosely based on the Minuit INTerface (Mint) Fitter used for the amplitude analyses of the decays $D^0 \to K^-K^-\pi^+\pi^-$ and $D^0 \to \pi^+\pi^-\pi^+\pi^-$ performed on CLEO data [79, 84]. Each complex amplitude can be evaluated approximately at a rate 10^6/s/core, which is roughly $20\times$ faster than the original Mint fitter. The improvement in performance is more dramatic for more complex amplitudes, such as those with more complicated spin amplitudes or using K-matrix propagators. Due to the improvement in performance, it is straightforward to fit the parameters of lineshapes such as masses and widths that usually need to be fixed. It is also possible to perform complex quasi-model independent investigations. Evaluation of the amplitudes, calculation of normalisation integrals and error propagation are all multi-threaded using the OpenMP API.

6.6.1 Decay descriptors

A model is described in terms of a series of user-specified decay descriptors. These are parsed into decay trees, which in turn can generate the binary expression tree for the amplitude. A series of examples of these decay descriptors are given, and the expressions that they generate:

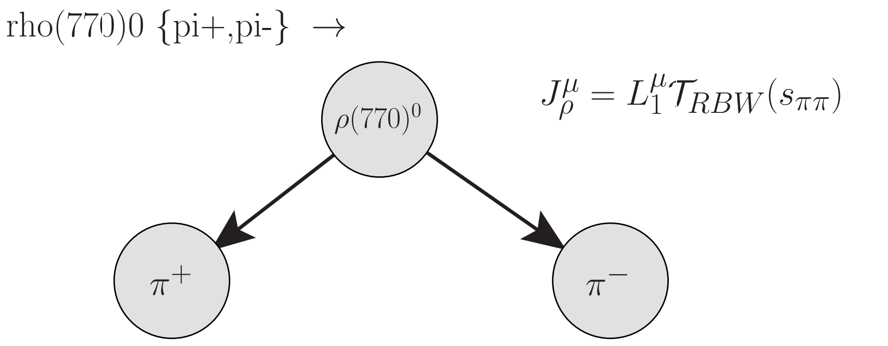

Figure 6.11: Decay descriptor, tree and expression for $\rho(770)^0 \to \pi^+\pi^-$

The first example is shown in Fig. 6.11. A $\rho(770)^0$ meson decays to a pair of pions. By default it is assumed that resonances are described by the relativistic Breit-Wigner formula, and that the daughter particles are in the minimal orbital angular momentum state allowed by the relevant conservation laws. Alternative lineshapes and other orbital angular momentum states can also be specified by modifying the decay descriptor.

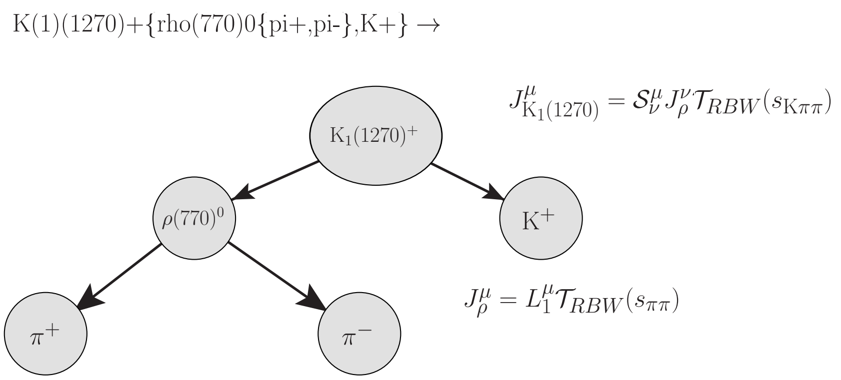

Figure 6.12: Decay descriptor, tree and expression for $K_1(1270) \to \rho(770)^0 K^+$.

The total decay tree can either be constructed from a series of subtrees, or specified inline. An example of this is shown in Fig. 6.12. A $K_1(1270)^+$ meson decays into a $\rho(770)^0$ meson and a charged kaon. The $\rho(770)^0$ meson has the same decay descriptor and hence amplitude as the previous example.

7

Amplitude analysis of $D^0 \to K^\mp\pi^\pm\pi^\mp\pi^\pm$ decays

Contents

In this chapter, the resonant sub-structure of the decay modes $D^0 \to K^-\pi^+\pi^+\pi^-$ and $D^0 \to K^+\pi^-\pi^-\pi^+$ are modelled using the formalism developed in Ch. 6.

Amplitude analyses have been performed in the past on the RS mode by the Mark III [78], and BES III collaborations [85]. The analysis of the favoured mode presented in this thesis uses $\approx 60\times$ the number of signal candidates as the BES III and roughly 700 times more than the Mark III analyses. In addition, the BES III analysis does not include the treatment of the effects of the three-body final states on the running widths of resonances outlined in Sect.6.3, nor the more complex scalar parameterisations outlined in Sect.6.1.2. This is the first amplitude analysis of the WS decay mode, made possible by the extremely large size of the LHCb data sets.

Section 7.1 introduces the formalism of the fit and how corrections for efficiency variations are implemented using simulated events. It is useful to be able to subdivide the four-body phase space reliably into a discrete set of hyper-volumes, both to quantify the quality of fits in a χ^2 test and to define regions of interest for future model-independent measurements. The algorithm for this division is described in Sect. 7.2.

The number of possible parameterisations is extremely large ($\approx \mathcal{O}(10^{17})$) in four-body amplitude models. Therefore a model-building algorithm is employed to select plausible parameterisations. This algorithm is outlined in Sect. 7.3

Sources of systematic uncertainty are discussed in Sect. 7.5. Results for the RS mode $D^0 \to K^-\pi^+\pi^+\pi^-$ are shown in Sect. 7.6. The knowledge gained from the favoured fit is then applied to the suppressed mode, with results presented in Sect. 7.7.

The model building procedure described in Sect. 7.3 results in ensembles of parameterisations with comparable fit qualities. The general features of these ensembles are discussed in Sect. 7.7.1. The coherence factor introduced in Ch. 2 and measured in Ch. 3 is then calculated using ensembles of models, and 'local' coherence factors and relative strong phases are calculated in a plausible binning scheme for future measurements.

7.1 Fitting formalism

Independent fits are performed on the $K^-\pi^+\pi^+\pi^-$ and $K^+\pi^-\pi^-\pi^+$ data sets, using an unbinned maximum-likelihood procedure to determine the amplitude parameters. The principal degrees of freedom in these fits are the complex coupling co-efficients between states, and in several cases masses and widths of isobars that are currently poorly known.

7.1.1 Likelihood definition

The probability density functions (PDFs) are functions of position in D^0 decay phase-space, $\mathbf{x}$, and are composed of the signal amplitude model and the two sources of background described in Ch. 5:

$$P(\mathbf{x}) = \varepsilon(\mathbf{x})\phi(\mathbf{x}) \left(\frac{Y_s}{\mathcal{N}_s} \left|\mathcal{M}(\mathbf{x})\right|^2 + \frac{Y_c}{\mathcal{N}_c}\mathcal{P}_c(\mathbf{x}) + \frac{Y_m}{\mathcal{N}_m}|\overline{\mathcal{M}}(\mathbf{x})|^2 \right). \tag{7.1}$$

The signal PDF is described by the function $\left|\mathcal{M}(\mathbf{x})\right|^2$, where $\mathcal{M}(\mathbf{x})$ is the total matrix element for the process, weighted by the four-body phase-space density $\phi(\mathbf{x})$, and the phase-space acceptance, $\varepsilon(\mathbf{x})$. The mistag component involving $\overline{\mathcal{M}}(\mathbf{x})$, is only present in the WS sample, and is modelled using the RS signal PDF. The combinatorial background is modelled by $\mathcal{P}_c(\mathbf{x})$, and is present in both samples. The normalisation of each component is given by the integral of the PDF over the phase space, $\mathcal{N}_i$, where $i = (c, s, m)$, weighted by the fractional yield, Y_i, determined in Ch. 5.

The function to minimise is twice the negative log-likelihood:

$$\mathcal{L} = -2 \sum_{\mathbf{x}\in\text{data}} \log\left(P(\mathbf{x})\right). \tag{7.2}$$

It is easier to minimise the equivalent reduced function

$$\mathcal{L}' = \mathcal{L} + 2 \sum_{\mathbf{x}\in\text{data}} \log(\phi(\mathbf{x})\varepsilon(\mathbf{x})) = -2 \sum_{\mathbf{x}\in\text{data}} \left(\frac{P(\mathbf{x})}{\phi(\mathbf{x})\varepsilon(\mathbf{x})} \right), \tag{7.3}$$

rather than $\mathcal{L}$, as neither the efficiency nor phase space depend on any parameters in the fit. This allows the cancellation of the efficiency and phase-space terms in $P(\mathbf{x})$, which significantly simplifies the fit procedure: the efficiency variations now only appear in the definition of the normalisation integrals, and hence an explicit parametrisation of how the efficiency varies across the five-dimensional phase space can be avoided.

The efficiency-corrected normalisation of each PDF, $\mathcal{P}(\mathbf{x})$, is calculated using Monte Carlo integration, and can be written as

$$\mathcal{N} = \int \mathrm{d}\mathbf{x}\varepsilon(\mathbf{x})\mathcal{P}(\mathbf{x}) \approx \frac{1}{N}\sum_{i=0}^{N} \frac{\varepsilon(\mathbf{x}_i)}{g(\mathbf{x}_i)} \left|\mathcal{P}(\mathbf{x})\right|^2, \tag{7.4}$$

where the sum is over events in an *integration sample.* The events in the integration sample are distributed according to $g(\mathbf{x})$ with respect to the phase-space density.

Consider the case where the integration sample consists of events that are generated with some distribution $\mathcal{G}(\mathbf{x})$, then propagated through the full reconstruction and selected in the same way as data. The distribution of events in the integration sample is therefore $g(\mathbf{x}) = \varepsilon(\mathbf{x})\mathcal{G}(\mathbf{x})$. Inserting this into Eq. 7.4 cancels the explicit dependence on the efficiency variation:

$$\mathcal{N} = \frac{1}{N}\sum_{i=0}^{N}\frac{\mathcal{P}(\mathbf{x})}{\mathcal{G}(\mathbf{x}_i)}. \tag{7.5}$$

The advantage of this approach is that an explicit functional form for the efficiency is not required by the fit, which is non-trivial to parameterise in five dimensions. The disadvantage of this scheme is that it requires large samples of fully simulated events, which is computationally expensive. This technique therefore relies on the reliability of the simulation in modelling variations in the acceptance across the phase space of the D decay.

The effect of the limited size of the integration sample can be mitigated by *importance sampling*. Consider the variance on a normalisation integral:

$$\mathrm{Var}(\mathcal{N}) = \frac{1}{N}\sum_{i=0}^{N}\left(\frac{\mathcal{P}(\mathbf{x}_i)}{\mathcal{G}(\mathbf{x}_i)}\right)^2 - \left(\frac{1}{N}\sum_{i=0}^{N}\frac{\mathcal{P}(\mathbf{x}_i)}{\mathcal{G}(\mathbf{x}_i)}\right)^2, \tag{7.6}$$

and the standard error on the integral given by $\sigma(\mathcal{N}) = \sqrt{\mathrm{Var}(\mathcal{N})/N}$. The uncertainty is minimised by choosing a generator distribution such that $\mathcal{G}(\mathbf{x}) \approx \mathcal{P}(\mathbf{x})$, which is to sample the function more frequently in regions where the value of the function is large. The integration samples are therefore generated such that they approximately match the distributions seen in real data. In practice, preliminary signal models of each decay are used to generate the integration samples, which are described in Sect. 5.7.

7.1.2 Fit fractions

The numerical values of coupling parameters depend strongly on various choices of convention in the formalism. Therefore, it is common to define the fractions in the data sample associated with each component of the amplitudes (fit fractions). In the limit of narrow resonances, the fit fractions are analogous to relative branching fractions. The fit fraction for component p is

$$I_p = \frac{\int d\mathbf{x}\,|\mathcal{M}_p(\mathbf{x})|^2}{\int d\mathbf{x}\sum_{ij}\mathcal{M}_i(\mathbf{x})\mathcal{M}_j(\mathbf{x})^*}. \tag{7.7}$$

For cascade processes, the different secondary isobars contribute coherently to the fit fractions. The *partial* fit fractions for each sub-process are then defined as the fit fraction with only the contributions from the parent isobar included in the denominator.

7.2 Dynamic binning

A dynamic binning scheme is used both in the estimation of the quality of the fit and to produce an underlying division of the phase space to produce binning schemes for Sect. 7.8. The algorithm approximately follows that described in Ref. [42], with additional steps to deal with only a small number of bins in the WS case that would not be correctly handled. This can be seen by the fact that the scheme in Ref. [42] produces 2^{dn} bins where d is the dimension of the problem (i.e. 5) and n is an integer. Therefore, this approach results in an unsuitable number of bins. For example, $n = 1$ would be 32 bins, which is too small to be useful, whereas $n = 2$ yields 1024 bins which is too many given the size of the WS sample. Hence, the procedure is modified with the second step described below in order to increase the granularity. The procedure is designed to divide a problem into N_{bins} bins with approximately an equal population in each, which should be of order the minimum population N_{min}, and is as follows:

1. For each bin that has a population of greater than $N_{min}2^d$ candidates:
   (a) Split bin along one direction, such that half the data lies either side of the division, ensuring that the bin width is greater than some minimum width.
   (b) Repeat in each direction.
   (c) Return to (a)
2. For each bin with a population less than $N_{min}2^d$ but greater than $2N_{min}$, select the number of divisions d' such that $d' = \lfloor \log_2\left(\frac{N}{N_{min}}\right)\rfloor$, i.e. the number of divisions that can be made such that the population in each resulting bin is greater than N_{min}. Then select the directions in which the data are least uniform[1]. Divide along these directions, also using the rule that half the population should end up in each sub-bin after division.

[1]Uniformity is defined in this case by the spread in nearest neighbour distances of candidates in the bin.

This binning scheme therefore divides a population equally amongst $\lfloor \log_2 \left(\frac{N}{N_{min}}\right) \rfloor$ bins.

7.2.1 Goodness-of-fit

The quality of fits is quantified by computing a χ^2 metric. Candidates are binned using the dynamic binning scheme described in the previous section. The five invariant mass-squared combinations are used as coordinates from the adaptive binning:

$$s_{\pi^+\pi^-\pi^+}\,,\, s_{K^-\pi^+}\,,\, s_{K^-\pi^-}\,,\, s_{\pi^+\pi^-}\,,\, s_{K^-\pi^+\pi^-}\,.$$

The choice of coordinates becomes irrelevant in the limit of very small bins, as the amplitude becomes a single-valued function of any five independent coordinates. The χ^2 is defined as:

$$\chi^2 = \sum_{i \in \mathrm{bins}} \frac{\left(N_i - \langle N_i \rangle\right)^2}{N_i + \bar{\sigma}_i^2}, \tag{7.8}$$

where N_i is the observed number of candidates and $\langle N_i \rangle$ the expected number of entries, determined by reweighting the integration sample with the fitted PDF:

$$\langle N_i \rangle = \sum_{j \in \mathrm{bin}(i)} \omega_j. \tag{7.9}$$

Here ω_j is the weight of integration event j. The statistical uncertainty from the finite size of the integration sample, $\bar{\sigma}_i$, is included in the definition of the χ^2, and is estimated as:

$$\bar{\sigma}_i^2 = \sum_{j \in \mathrm{bin}(i)} \omega_j^2. \tag{7.10}$$

7.3 Model construction

The number of possible models that could be used to fit the amplitudes is extremely large due to the large number of possible decay chains. This is due to the fact that each decay chain contains a pair of isobars. For example, the $a_1(1260)$ resonance could potentially decay to the three pion final state via the following six intermediate states

$$\left[\rho(770)^0\pi^+\right]^{L=0,2}\,,\, \left[\rho(1450)^0\pi^+\right]^{L=0,2}\,,\, [\pi^+\pi^-]^{L=0}\pi^+\,,\, f_2(1270)\pi^+.$$

So for each of the cascade processes, there are a large number of different possibilities for the intermediate decays of the resonances. There are also typically a large number of different isobar and orbital angular momentum configurations for the quasi-two body topology. The possible decay chains that are considered are discussed in Sect. 7.4. A model of "reasonable" complexity will typically contain $\mathcal{O}(10)$ different decay chains, and hence a naive estimate for the number of possible models is on the order $\mathcal{O}(10^{17})$. It is therefore unfeasible to test any reasonable proportion of the possible parameter space. Therefore, an algorithmic approach to model building is adopted, the steps of which are listed below.

1. Take a model and a set of possible additional decay chains. Perform a fit to the data using this model adding one of these decay chains.

2. If adding this decay chain improves the χ^2 per degree of freedomby at least 0.02, then retain the model for further consideration.

3. On the first iteration, restrict the pool of decay chains that are added to the model to those 40 contributions that give the largest improvements to the fit.

4. Re-iterate the model-building procedure, using the 15 models with the best fit quality as the initial model as starting points. Finish the procedure if no model has improved significantly.

For each decay mode, a different initially guessed model is used at the beginning of the procedure based on the current knowledge of the decay mode. In the RS case, the initially guessed model is chosen to be similar to the Mark III model, with several additional decay chains included on the basis of other amplitude analyses:

- The dominant decay chain in the Mark III model is $D^0 \to a_1(1260)^+K^-$, but only including the $a_1(1260)^+ \to \rho\pi^+$ decay. The decay chains $a_1(1260)^+ \to [\pi\pi]^{L=0}\pi$ and $a_1(1260)^+ \to [\rho\pi]^{L=2}$ are also included, as these have been observed in the amplitude analysis of $D^0 \to \pi^+\pi^-\pi^+\pi^-$ performed by the FOCUS collaboration [86].

- The $D^0 \to [K^*(892)^0\rho(770)^0]^{L=1}$ decay chain, which is expected to be present given the existence of the S-wave and D-wave like [2] components found in the Mark III model.

[2]The definitions of the S-wave and D-wave components in the Mark III model differ for the reasons discussed in Sect. 6.2.1.

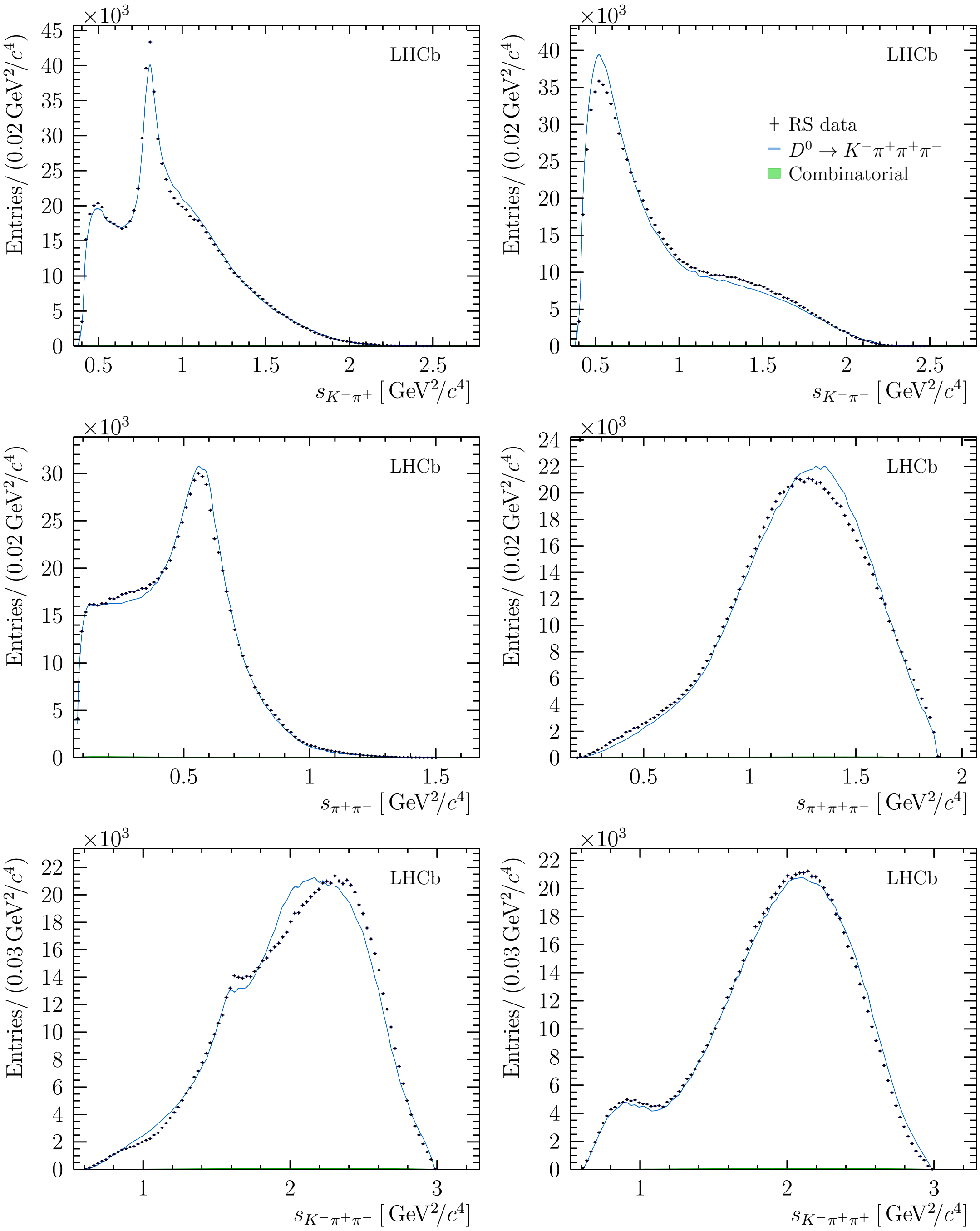

Figure 7.1: Distributions for six invariant-mass observables in the RS mode $D^0 \to K^-\pi^+\pi^+\pi^-$. The expectation from the initially guessed model is shown in blue. The total background contribution, which is very low, is shown in green.

- The $D^0 \to K_2^*(1430)^-[K^-\pi^+\pi^-]\pi^+$ decay chain is expected based on the $D^0 \to K_2^*(1430)^-[K_S^0\pi^-]\pi^+$ branching ratio, which was measured to be $(3.4^{+1.9}_{-1.0}) \times 10^{-4}$ in an amplitude analysis performed by the BaBar collaboration [46]. Using the branching ratios of the $K_2^*(1430)^-$ reported in Ref. [34] and using isospin arguments, the fit fraction of $D^0 \to K_2^*(1430)^- \left[\overline{K}^*(892)^0\pi^-\right]\pi^+$ should be $\approx 0.5\%$.

- The decay $D^0 \to K_1(1400)^-\pi^+$ is expected to be present as the $K_1(1270)$ and $K_1(1400)$ are mixtures of the 1^1P_1 and 1^3P_1 quark states as discussed in Sect. 2.6. Hence, as couplings are expected to be between quark eigenstates rather than mass eigenstates, if the $K_1(1270)$ is present, the $K_1(1400)$ must also be present.

- The four-body non-resonant term included in the Mark III model is replaced with a two-body scalar-scalar term represented by a product of $\pi\pi$ and $K\pi$ K-matrices.

Invariant-mass distributions for this preliminary fit are shown in Fig. 7.1.

The initial model for the WS decay mode is found by inspecting invariant-mass projections as there is no existing amplitude model, and in general few models of doubly Cabibbo-suppressed D^0 decays on which to base any assumptions. The only clear contributions in the invariant-mass projections are from the $K^*(892)^0$ and $\rho(770)$ resonances. The quasi two-body contributions should be roughly comparable between WS and RS amplitudes, hence it is presumed that this is a $D^0 \to K^*(892)^0\rho(770)$ contribution, which is included in the default model in all three orbital angular momentum states. Using a similar argument, a two-body scalar-scalar term modelled by a product of K matrices is also included in the default WS model as this is found to have a considerable contribution to the RS decay mode. Invariant-mass distributions for this preliminary fit are shown in Fig. 7.2.

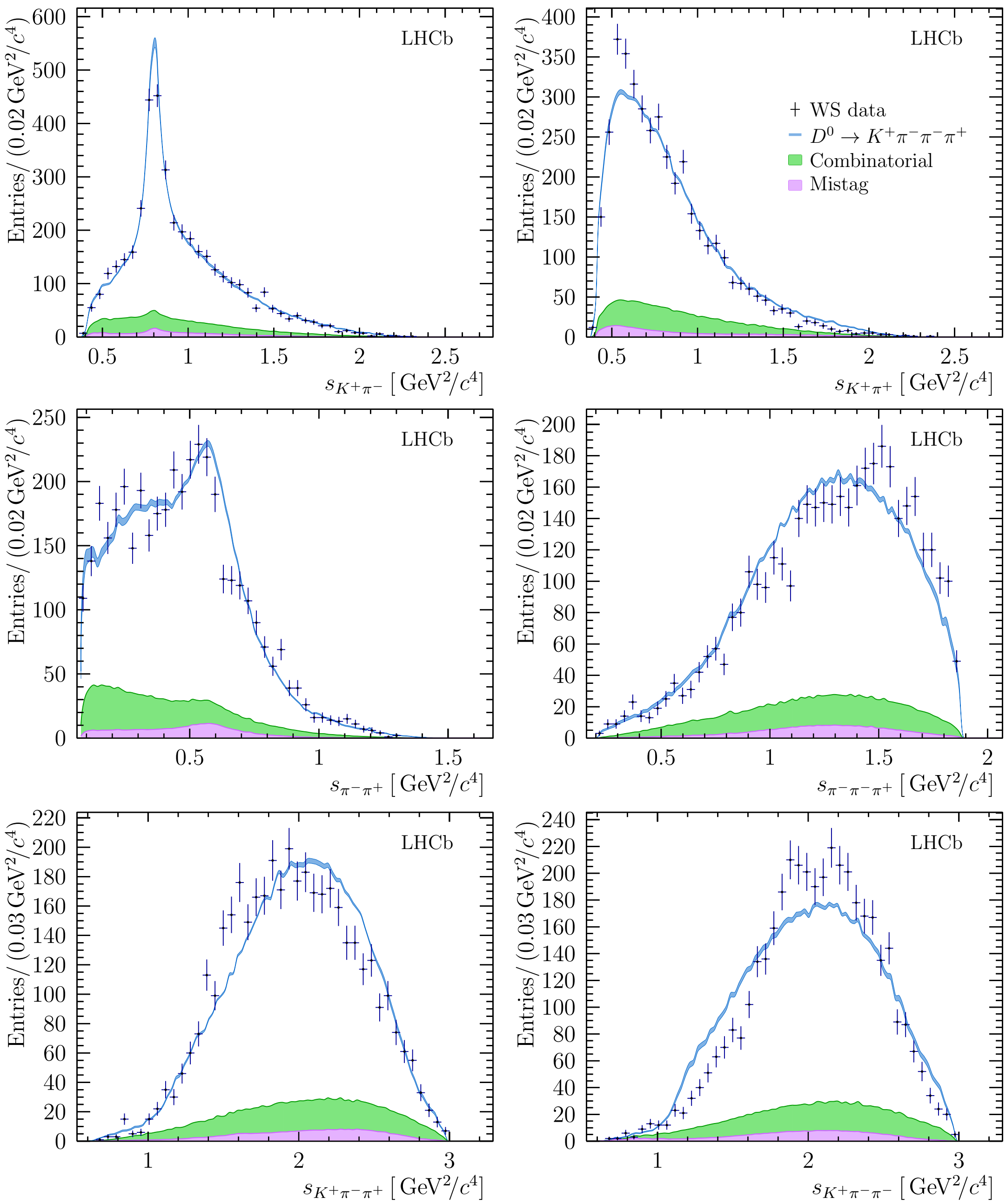

Figure 7.2: Distributions for six invariant-mass observables in the WS mode $D^0 \to K^+\pi^-\pi^-\pi^+$. The expectation from the initially guessed model is shown in blue. The total background contribution is shown in green.

7.4 List of decay chains

The list of possible decay chains is built from what is allowed by the relevant conservation laws. Approximately one hundred different decay chains are included as possible contributions to the model. Certain cascade decays already have well known sub-branching ratios. For example, although the $K_1(1400)$ decays almost exclusively via the $K^*(892)$, the various decays of the $K_1(1400)$ are treated separately without assumption about their branching ratios.

- $D^0 \to Y_{\pi\pi}\,[\pi\pi]\,Y_{K\pi}\,[K\pi]$, where $Y_{\pi\pi}$ is one of the following states: $\rho(770)$, $\rho(1450)$, $f_2(1270)$ or $[\pi^+\pi^-]^{L=0}$, and $Y_{K\pi}$ is one of the following: $K^*(892)^0$, $K^*(1410)^0$, $K^*(1680)^0$, $K_2^*(1430)^0$ or $[K^-\pi^+]^{L=0}$.

  The $[\pi^+\pi^-]^{L=0}$ and $[K^-\pi^+]^{L=0}$ contributions are modelled using K matrices. In cases with a scalar contribution and a radial recurrence of a vector state, such as $\rho(1450)^0[K^-\pi^+]^{L=0}$, the K matrix is fixed to be the same as the first vector, i.e. the K-matrix parameters of $\rho(770)^0[K^-\pi^+]^{L=0}$. For vector-vector and vector-tensor contributions, the different possible polarisation states are included together in the model building. The contributions from the radial excitations of the kaon are only included as a possibility when included with the $\pi\pi$ S-wave, as the other decay chains involving this resonance, for example the decay $K^*(1410)\rho(770)^0$, tend to have large interference terms, which requires fine tuning with other amplitudes and hence are considered to be unphysical.

- $D^0 \to X_{\pi\pi\pi}\,[Y_{\pi\pi}\,[\pi\pi]\,\pi]\,K$, where $X_{\pi\pi\pi}$ is one of the following states: $a_1(1260)$, $a_1(1640)$, $\pi(1300)$ or $a_2(1320)$.

- $D^0 \to X_{K\pi\pi}\,[Y_{K\pi}\,[K\pi]\,\pi]\,\pi$, $D^0 \to X_{K\pi\pi}\,[Y_{\pi\pi}\,[\pi\pi]\,K]\,\pi$, where $X_{K\pi\pi}$ is one of the following states: $K_1(1270)$, $K_1(1400)$, $K^*(1410)$, $K^*(1680)$, $K_2^*(1430)$ or $K(1460)$.

All of these states are considered under all possible orbital configurations that obey the respective conservation laws.

7.5 Systematic uncertainties

Several sources of systematic uncertainty are considered. Experimental issues are discussed first, followed by uncertainties related to the model and the formalism.

All parameters in the fit have a systematic uncertainty originating from the finite size of the integration sample used in the likelihood minimisation. This effect is reduced by *importance sampling*. The events in the integration sample are distributed approximately according to the signal PDFs, which reduces the uncertainty on the normalisation integrals. The remaining uncertainty is estimated using a resampling technique. Half of the integration sample is randomly selected, and the fit performed using only this subsample. This is done many times, and the systematic uncertainty from the finite integration statistics is taken to be $1/\sqrt{2}$ the width of the distribution of fit parameters from this exercise.

There is an additional systematic uncertainty due to possible imperfect modelling of the detector and the underlying event in the simulation, which will in turn lead to incorrect efficiency corrections. These effects are estimated by sub-dividing the data set into equally populated bins by a variable in which the efficiency corrections may be expected to vary, which is chosen to be the transverse momentum of the D^0-meson candidate. The data in these bins are then refitted independently. The fit results for each of these slices is then combined, and the absolute difference between this result and the nominal fit taken as an estimate of the uncertainty in any mis-modelling of the efficiency. Additional robustness checks are performed using the RS data-set, dividing the data by data-taking year and signal trigger category, and are found to compatible within the assigned uncertainties.

The uncertainty due to the determination of the signal fraction and mistag fraction in each sample is measured by varying these fractions within the uncertainties found in the fit to the $m_{K\pi\pi\pi}$: Δm plane.

Well-known parameters that are not floated in the fit, such as the $\rho(770)^0$ mass and width, are randomly varied according to the uncertainties given in Ref. [87], and the corresponding difference on the parameters in the fit given by the distribution of fit results are assigned as uncertainties. It is assumed that input correlations between these parameters are negligible. Radii of several particles used in the Blatt-Weisskopf form factor are varied using the same procedure. The D^0 radial parameter is varied by $\pm 0.5\,\mathrm{GeV}^{-1}$.

The uncertainty due to parametrisation of the combinatorial background in the WS case is estimated using pseudo-experiments. A combination of MC signal events generated with the final model and sideband events is used to approximately simulate the data set. The composite data set is then refitted using the signal model, and differences between the generator level and fitted values are taken as the systematic uncertainty on the background parametrisation.

The final choice of model is an additional source of systematic uncertainty. For the coupling parameters, it is not meaningful to compare them between different parameterisations, as these are by definition the parameters of a given model. It is however useful to consider the impact the choice of parametrisation has on fit fractions and the fitted masses and widths. Therefore, the model choice is not included in the total systematic uncertainty, but its impact on the relevant parameters is considered separately in Sect. 7.7.1. The impact of the model choice on the description of the phase variations is considered in Sect. 7.8.

The total systematic uncertainty is obtained by adding together the components in quadrature. The total systematic uncertainty is significantly larger than the statistical uncertainty on the RS fit, with the largest contributions coming from the form factors that account for the finite size of the decaying mesons. For the WS fit, the total systematic uncertainty is comparable to the statistical uncertainty, with the largest uncertainty coming from the parametrisation of the combinatorial background. A full breakdown of the different sources of systematic uncertainty for all parameters is given in Appendix 8.

7.6 The RS-mode $D^0 \to K^-\pi^+\pi^+\pi^-$

Invariant-mass projections for $D^0 \to K^-\pi^+\pi^+\pi^-$are shown in Fig. 7.3 together with the expected distribution from the model in Table 7.1. The χ^2 per degree-of-freedom is calculated, with the only source of systematic uncertainty considered from the finite size of the integration sample, and is found for the final model to be ≈ 1.24, indicating that the data are reasonably described by the model given the very large sample size.

Three cascade contributions, the $a_1(1260)^+$, the $K_1(1270)^-$ and $K(1460)^-$ are modelled using the three-body running width treatment described in Sect. 6.3. The masses and widths of these states are floated in the fit. The mass, width and coupling parameters for these resonances are presented in Tables 7.2, 7.3 and 7.4.

Table 7.1: Table of fit fractions, coupling parameters and other quantities for the RS mode $D^0 \to K^-\pi^+\pi^+\pi^-$. Also given is the χ^2 per degree of freedom (ν) for the fit. The first uncertainty is statistical, the second systematic. Couplings are defined with respect to the coupling to the channel $D^0 \to [K^*(892)^0\rho(770)^0]^{L=2}$.

	Fit Fraction [%]	$\lvert g\rvert$	$\arg(g)[^o]$
$\left[\overline{K}^*(892)^0\rho(770)^0\right]^{L=0}$	$7.34 \pm 0.08 \pm 0.47$	$0.196 \pm 0.001 \pm 0.015$	$-22.4 \pm 0.4 \pm 1.6$
$\left[\overline{K}^*(892)^0\rho(770)^0\right]^{L=1}$	$6.03 \pm 0.05 \pm 0.25$	$0.362 \pm 0.002 \pm 0.010$	$-102.9 \pm 0.4 \pm 1.7$
$\left[\overline{K}^*(892)^0\rho(770)^0\right]^{L=2}$	$8.47 \pm 0.09 \pm 0.67$		
$\left[\rho(1450)^0\overline{K}^*(892)^0\right]^{L=0}$	$0.61 \pm 0.04 \pm 0.17$	$0.162 \pm 0.005 \pm 0.025$	$-86.1 \pm 1.9 \pm 4.3$
$\left[\rho(1450)^0\overline{K}^*(892)^0\right]^{L=1}$	$1.98 \pm 0.03 \pm 0.33$	$0.643 \pm 0.006 \pm 0.058$	$97.3 \pm 0.5 \pm 2.8$
$\left[\rho(1450)^0\overline{K}^*(892)^0\right]^{L=2}$	$0.46 \pm 0.03 \pm 0.15$	$0.649 \pm 0.021 \pm 0.105$	$-15.6 \pm 2.0 \pm 4.1$
$\rho(770)^0\,[K^-\pi^+]^{L=0}$	$0.93 \pm 0.03 \pm 0.05$	$0.338 \pm 0.006 \pm 0.011$	$73.0 \pm 0.8 \pm 4.0$
$\alpha_{3/2}$		$1.073 \pm 0.008 \pm 0.021$	$-130.9 \pm 0.5 \pm 1.8$
$\overline{K}^*(892)^0\,[\pi^+\pi^-]^{L=0}$	$2.35 \pm 0.09 \pm 0.33$		
$f_{\pi\pi}$		$0.261 \pm 0.005 \pm 0.024$	$-149.0 \pm 0.9 \pm 2.7$
β_1		$0.305 \pm 0.011 \pm 0.046$	$65.6 \pm 1.5 \pm 4.0$
$a_1(1260)^+K^-$	$38.07 \pm 0.24 \pm 1.38$	$0.813 \pm 0.006 \pm 0.025$	$-149.2 \pm 0.5 \pm 3.1$
$K_1(1270)^-\pi^+$	$4.66 \pm 0.05 \pm 0.39$	$0.362 \pm 0.004 \pm 0.015$	$114.2 \pm 0.8 \pm 3.6$
$K_1(1400)^-\left[\overline{K}^*(892)^0\pi^-\right]\pi^+$	$1.15 \pm 0.04 \pm 0.20$	$0.127 \pm 0.002 \pm 0.011$	$-169.8 \pm 1.1 \pm 5.9$
$K_2^*(1430)^-\left[\overline{K}^*(892)^0\pi^-\right]\pi^+$	$0.46 \pm 0.01 \pm 0.03$	$0.302 \pm 0.004 \pm 0.011$	$-77.7 \pm 0.7 \pm 2.1$
$K(1460)^-\pi^+$	$3.75 \pm 0.10 \pm 0.37$	$0.122 \pm 0.002 \pm 0.012$	$172.7 \pm 2.2 \pm 8.2$
$[K^-\pi^+]^{L=0}\,[\pi^+\pi^-]^{L=0}$	$22.04 \pm 0.28 \pm 2.09$		
$\alpha_{3/2}$		$0.870 \pm 0.010 \pm 0.030$	$-149.2 \pm 0.7 \pm 3.5$
$\alpha_{K\eta'}$		$2.614 \pm 0.141 \pm 0.281$	$-19.1 \pm 2.4 \pm 12.0$
β_1		$0.554 \pm 0.009 \pm 0.053$	$35.3 \pm 0.7 \pm 1.6$
$f_{\pi\pi}$		$0.082 \pm 0.001 \pm 0.008$	$-147.0 \pm 0.7 \pm 2.2$
Sum of Fit Fractions	$98.29 \pm 0.37 \pm 0.84$		
χ^2/ν	$40483/32701 = 1.238$		

Table 7.2: Table of fit fractions and coupling parameters for the component involving the $a_1(1260)^+$ meson. The coupling parameters are defined with respect to the $a_1(1260)^+ \to \rho^0\pi^-$ coupling. For each parameter, the first uncertainty is statistical, the second systematic.

$a_1(1260)^+$	$m_0 = 1195.05 \pm 1.05 \pm 6.33\,\mathrm{MeV}/c^2$; $\Gamma_0 = 422.01 \pm 2.10 \pm 12.72\,\mathrm{MeV}/c^2$		
	Partial Fractions [%]	$\lvert g\rvert$	$\arg(g)[^o]$
$\rho(770)^0\pi^+$	$89.75 \pm 0.45 \pm 1.00$		
$[\pi^+\pi^-]^{L=0}\,\pi^+$	$2.42 \pm 0.06 \pm 0.12$		
β_1		$0.991 \pm 0.018 \pm 0.037$	$-22.2 \pm 1.0 \pm 1.2$
β_0		$0.291 \pm 0.007 \pm 0.017$	$165.8 \pm 1.3 \pm 3.1$
$f_{\pi\pi}$		$0.117 \pm 0.002 \pm 0.007$	$170.5 \pm 1.2 \pm 2.2$
$[\rho(770)^0\pi^+]^{L=2}$	$0.85 \pm 0.03 \pm 0.06$	$0.582 \pm 0.011 \pm 0.027$	$-152.8 \pm 1.2 \pm 2.5$

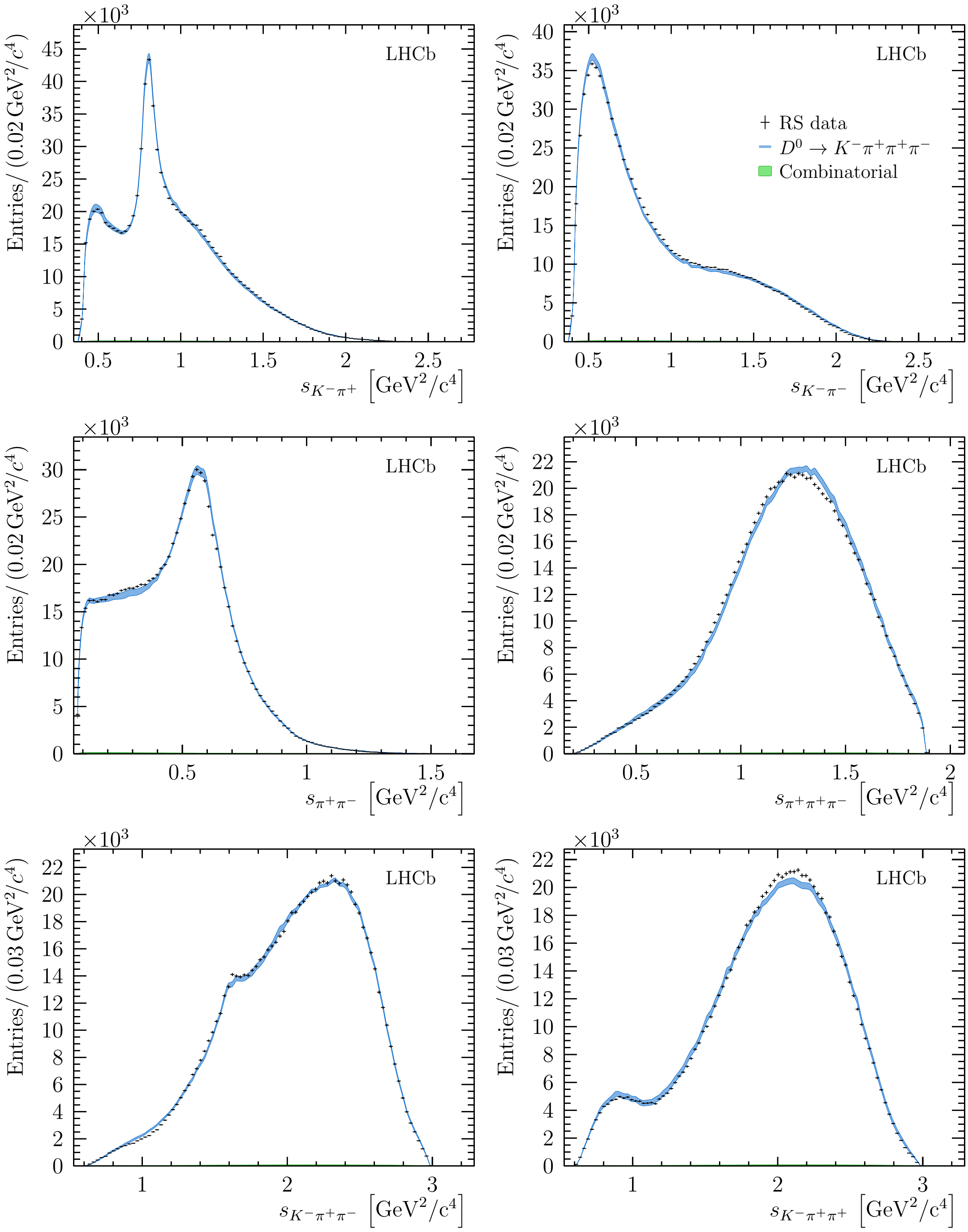

Figure 7.3: Distributions for six invariant-mass observables in the RS mode $D^0 \to K^-\pi^+\pi^+\pi^-$. Bands indicate the expectation from the model, with the width of the band indicating the total systematic uncertainty. The total background contribution, which is very low, is shown in green.

The largest contribution is found to come from the axial vector $a_1(1260)^+$, which is a result that was also found in the Mark III analysis. This decay proceeds via the colour-favoured external W-emission diagram that is expected

Table 7.3: Table of fit fractions and coupling parameters for the component involving the $K_1(1270)$ meson. The coupling parameters are defined with respect to the $K_1(1270) \to \rho^0 K^-$ coupling. For each parameter, the first uncertainty is statistical, the second systematic.

$K_1(1270)^-$	$m_0 = 1289.81 \pm 0.56 \pm 1.66\,\mathrm{MeV}/c^2$; $\Gamma_0 = 116.11 \pm 1.65 \pm 2.96\,\mathrm{MeV}/c^2$		
	Partial Fractions [%]	$\lvert g \rvert$	$\arg(g)[^o]$
$\rho(770)^0 K^-$	$96.30 \pm 1.64 \pm 6.61$		
$\rho(1450)^0 K^-$	$49.09 \pm 1.58 \pm 11.54$	$2.016 \pm 0.026 \pm 0.211$	$-119.5 \pm 0.9 \pm 2.3$
$\overline{K}^*(892)^0 \pi^-$	$27.08 \pm 0.64 \pm 2.82$	$0.388 \pm 0.007 \pm 0.033$	$-172.6 \pm 1.1 \pm 6.0$
$[K^-\pi^+]^{L=0}\,\pi^-$	$22.90 \pm 0.72 \pm 1.89$	$0.554 \pm 0.010 \pm 0.037$	$53.2 \pm 1.1 \pm 1.9$
$\left[\overline{K}^*(892)^0 \pi^-\right]^{L=2}$	$3.47 \pm 0.17 \pm 0.31$	$0.769 \pm 0.021 \pm 0.048$	$-19.3 \pm 1.6 \pm 6.7$
$\omega(782)\,[\pi^+\pi^-]\,K^-$	$1.65 \pm 0.11 \pm 0.16$	$0.146 \pm 0.005 \pm 0.009$	$9.0 \pm 2.1 \pm 5.7$

Table 7.4: Table of fit fractions and coupling parameters for the component involving the $K(1460)^-$ meson. The coupling parameters are defined with respect to the $K(1460)^- \to K^*\pi$ coupling. For each parameter, the first uncertainty is statistical, the second systematic.

$K(1460)^-$	$m_0 = 1482.40 \pm 3.58 \pm 15.22\,\mathrm{MeV}/c^2$; $\Gamma_0 = 335.60 \pm 6.20 \pm 8.65\,\mathrm{MeV}/c^2$		
	Partial Fractions [%]	$\lvert g \rvert$	$\arg(g)[^o]$
$\overline{K}^*(892)^0 \pi^-$	$51.39 \pm 1.00 \pm 1.71$		
$[\pi^+\pi^-]^{L=0}\,K^-$	$31.23 \pm 0.83 \pm 1.78$		
f_{KK}		$1.819 \pm 0.059 \pm 0.189$	$-80.8 \pm 2.2 \pm 6.6$
β_1		$0.813 \pm 0.032 \pm 0.136$	$112.9 \pm 2.6 \pm 9.5$
β_0		$0.315 \pm 0.010 \pm 0.022$	$46.7 \pm 1.9 \pm 3.0$

to dominate this final state.

There are also large contributions from the different orbital angular momentum configurations of the quasi two-body processes $D^0 \to K^*(892)^0\rho(770)^0$, with a total contribution of around 20%. The polarisation structure of this component is not consistent with naive expectations, with the D wave being the dominant contribution and overall hierarchy $D > S > P$. This result may be compared with that obtained for the study $D^0 \to \rho(770)^0\rho(770)^0$ in Ref. [84], where the D-wave polarisation of the amplitude was also found to be dominant.

A significant contribution is found from the unconfirmed pseudo-scalar state $K(1460)^-$. This resonance is a 2^1S_0 excitation of the kaon [35]. Evidence for this state has been reported in the partial-wave analyses of the process $K^\pm p \to K^\pm\pi^+\pi^-p$ [39, 38], manifesting itself as a 0^- state with mass $\approx 1400\,\mathrm{MeV}/c^2$ and width $\approx 250\,\mathrm{MeV}/c^2$ coupling to the $K^*(892)^0\pi$ and $[\pi^-\pi^+]^{L=0}K^-$ channels. The mass and width reported in Table 7.4 are found to be somewhat larger than these previously

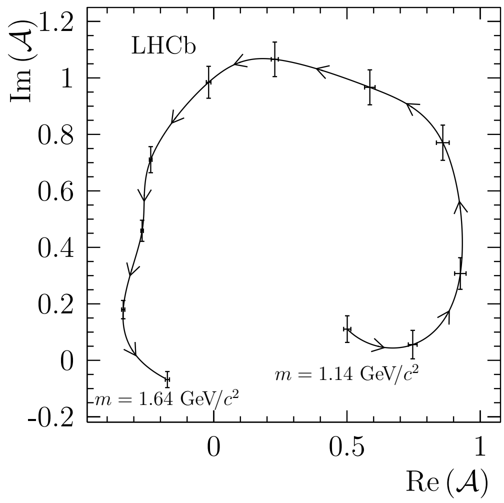

Figure 7.4: The Argand diagram for the model-independent partial-wave analysis (MIPWA) for the $K(1460)$ resonance. Points show the values of the function determined by the fit, with only statistical uncertainties shown.

reported values. However these are values for a particular parametrisation of the amplitude, and hence cannot be readily compared to other measurements. The comparison can be made with the peak position and width calculated using the amplitude, which are found to be $m_{\text{peak}} \approx 1420\,\text{MeV}/c^2$ and $\Gamma_{\text{peak}} \approx 260\,\text{MeV}/c^2$, and are in excellent agreement with those quoted in Ref. [39]. The intermediate decays of the $K(1460)^-$ are also found to be roughly consistent with previous studies, with approximately equal widths to $K^*(892)^0\pi$ and $[\pi\pi]^{L=0}K$. The resonant nature of this state is confirmed using a model-independent partial-wave analysis (MIPWA), following the method first used by the E791 collaboration [82, 83]. The relativistic Breit-Wigner parametrisation is replaced with a set of complex values defined at 15 discrete positions in $s(K^-\pi^+\pi^-)$, with the complex value at each point treated as an independent pair of free parameters to be determined by the fit. The amplitude is then modelled by interpolating between these values using cubic splines. The Argand diagram for this amplitude is shown in Fig. 7.4, with points indicating the values determined by the fit, and shows the phase motion expected from a resonance.

Four-body weak decays contain amplitudes that are both even, such as $D \to [VV']^{L=0,2}$, where V and V' are vector resonances, and odd, such as $D \to [VV']^{L=1}$, under parity transformations. Interference between these amplitudes can give rise to parity asymmetries which are different in D^0 and $\overline{D}^0$ decays. These asymmetries are the result of strong-phase differences, but can be mistaken for *CP* asymmetries [88]. Both sources of asymmetry can be studied by examining the distribution of the angle between the decay planes of the two quasi two-body systems, ϕ, which can be constructed from the three-momenta $\mathbf{p}$ of the decay products in the rest frame of the D^0 meson as

$$\begin{aligned}\cos(\phi) &= \hat{\mathbf{n}}_{K^-\pi^+} \cdot \hat{\mathbf{n}}_{\pi^-\pi^+} \\ \sin(\phi) &= \frac{\mathbf{p}_{\pi^+} \cdot \hat{\mathbf{n}}_{K^-\pi^+}}{|\mathbf{p}_{\pi^+} \times \hat{\mathbf{p}}_{K^-\pi^+}|},\end{aligned} \tag{7.11}$$

where $\hat{\mathbf{n}}_{ab}$ is the direction normal to the decay plane of a two-particle system ab,

$$\hat{\mathbf{n}}_{ab} = \frac{\mathbf{p}_a \times \mathbf{p}_b}{|\mathbf{p}_a \times \mathbf{p}_b|}, \tag{7.12}$$

and $\hat{\mathbf{p}}_{K^-\pi^+}$ is the direction of the combined momentum of the $K^-\pi^+$ system.

The interference between P-even and P-odd amplitudes averages to zero when integrated over the entire phase space. Therefore, the angle ϕ is studied in regions of phase space. The region of the $\overline{K}^*(892)^0$ and $\rho(770)^0$ resonances is studied as the largest P-odd amplitude is the decay $D^0 \to [\overline{K}^*(892)^0\rho(770)^0]^{L=1}$. Selecting this region allows the identical pions to be distinguished, by one being part of the $\overline{K}^*(892)^0$-like system and the other in the $\rho(770)^0$-like system. The data in this region are shown in Fig. 7.5, divided into quadrants of helicity angles, θ_A and θ_B, defined as the angle between the K^-/π^- and the D^0 in the rest frame of the $K^-\pi^+/\pi^-\pi^+$ system. The distributions show clear asymmetries under reflection about 180°, indicating parity nonconservation. However, equal and opposite asymmetries are observed in the CP-conjugate mode $\overline{D}^0 \to K^+\pi^-\pi^-\pi^+$, indicating that these asymmetries originate from strong phases, rather than from CP-violating effects. Bands show the expected asymmetries based on the amplitude model, which has been constructed according to the CP-conserving hypothesis, and show reasonable agreement with the data.

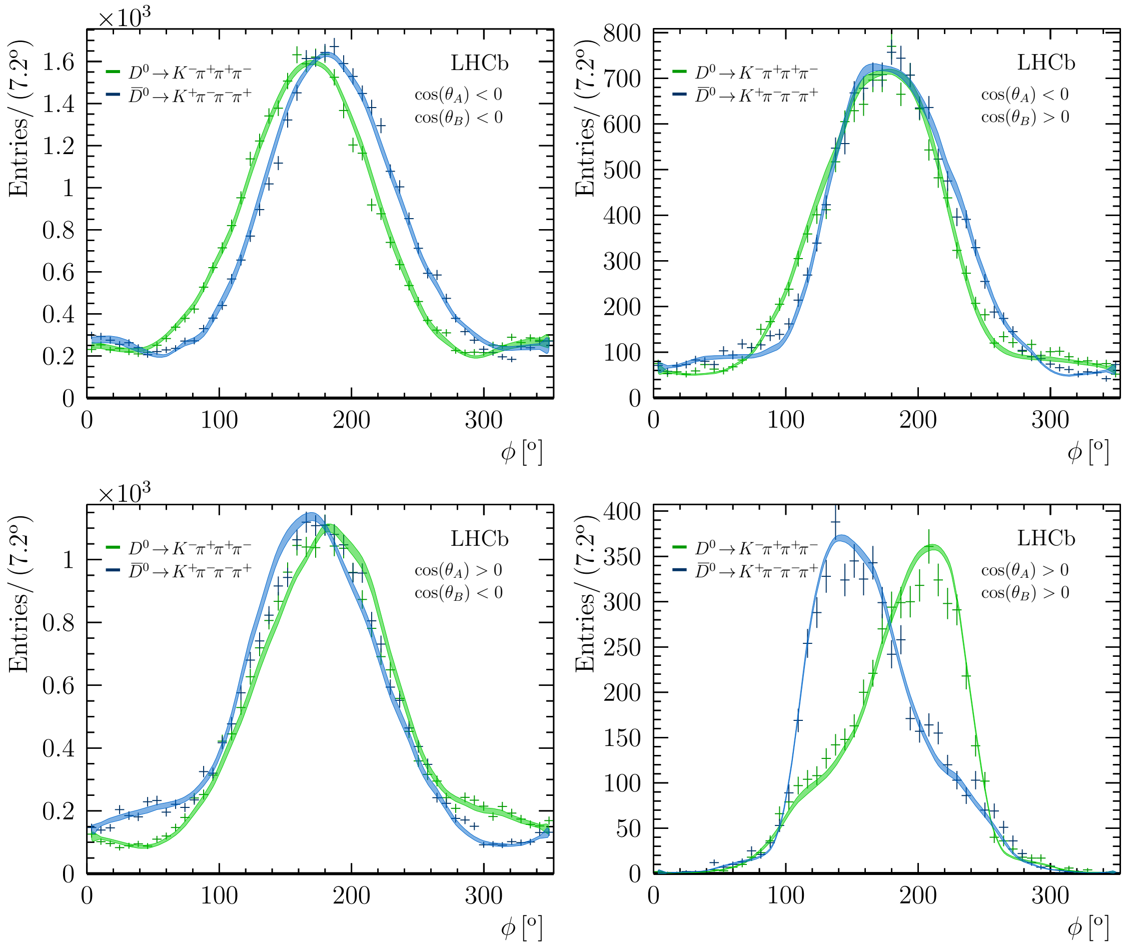

Figure 7.5: Parity violating distributions for the RS decay in the $\overline{K}^*(892)^0\rho(770)^0$ region defined by $\pm 35\,\mathrm{MeV}(\pm 100\,\mathrm{MeV})$ mass windows about the nominal $\overline{K}^*(892)^0$ $(\rho(770)^0)$ masses. Bands show the predictions of the fitted model including systematic uncertainties.

7.7 The WS-mode $D^0 \to K^+\pi^-\pi^-\pi^+$

Invariant-mass distributions for $D^0 \to K^+\pi^-\pi^-\pi^+$are shown in Fig. 7.6. Large contributions are clearly seen in $s_{K^+\pi^-}$ from the $K^*(892)^0$ resonance. The fit fractions and amplitudes of the final model are given in Table **??**. Dominant contributions are found from the axial kaons, $K_1(1270)^+$ and $K_1(1400)^+$, which are related to the same colour-favoured W-emission diagram that dominates the RS mode, where it manifests itself in the $a_1(1260)^+K^-$ component.

The reduced χ^2 for the fit to the WS mode is ≈ 1.46, which is notably worse than for the RS mode despite the lower statistics. If the true WS amplitude has a comparable structure to the RS amplitude, it contains several decay chains at the $\mathcal{O}(1\%)$ level that cannot be satisfactorily resolved given the small sample size, and hence the quality of the WS fit is degraded by the absence of these sub-dominant contributions.

The contribution from the $K_1(1400)^+$ is larger than that from the $K_1(1270)^+$. It is instructive to consider this behaviour in terms of the quark states, ${}^1P_1$ and ${}^3P_1$. These quark states mix approximately equally to produce the mass eigenstates,

$$\begin{aligned} |K_1(1400)\rangle &= \cos(\theta_K)|{}^3P_1\rangle - \sin(\theta_K)|{}^1P_1\rangle \\ |K_1(1270)\rangle &= \sin(\theta_K)|{}^3P_1\rangle + \cos(\theta_K)|{}^1P_1\rangle, \end{aligned} \tag{7.13}$$

where θ_K is a mixing angle. The mixing is somewhat less than maximal, with Ref. [36] reporting a preferred solution with $\theta_K = (33^{+6}_{-2})^{\mathrm{o}}$. In the WS mode, the axial kaons are produced via a weak current, which is decoupled from the ${}^1P_1$ state in the SU(3) flavour-symmetry limit. If the mixing were maximal the mass eigenstates would be produced equally, but a smaller mixing angle results in a preference for the $K_1(1400)$, which is qualitatively consistent with the pattern seen in data. In the RS mode, the axial kaons are not produced by the external weak current, and hence there is no reason to expect either quark state to be preferred. The relatively small contribution from the $K_1(1400)$ to this final state is then understood as a consequence of approximately equal production of the quark states.

The coupling parameters and shape parameters of the $K_1(1270)$ resonance are fixed to the values measured in the RS mode in the nominal fit. A fit is also performed with these coupling parameters freely varying, and they are found to be consistent with those measured in the RS mode.

A large contribution is found from $D^0 \to \rho(1450)^0 K^*(892)^0$ in all models that describe the data well. This result is likely to be an effective representation of several different K^* production modes that are well approximated by this term.

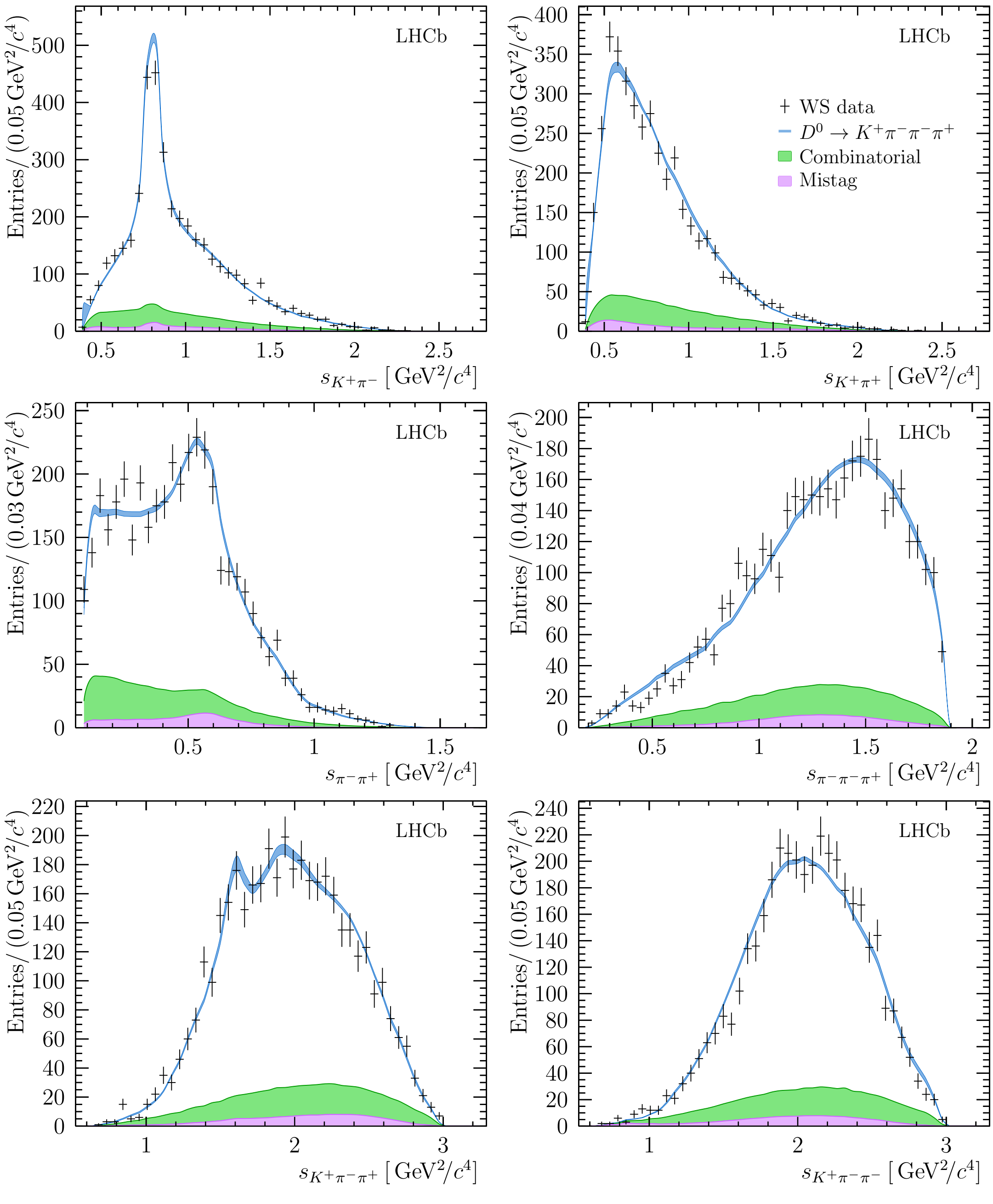

Figure 7.6: Distributions for six invariant-mass observables in the WS decay $D^0 \to K^+\pi^-\pi^-\pi^+$. Bands indicate the expectation from the model, with the width of the band indicating the total systematic uncertainty. The total background contribution is shown as a filled area, with the lower region indicating the expected contribution from mistagged $\overline{D}^0 \to K^+\pi^-\pi^-\pi^+$ decays.

Table 7.5: Table of fit fractions, coupling parameters and other quantities for the WS mode $D^0 \to K^+\pi^-\pi^-\pi^+$. Also given is the χ^2 per degree-of-freedom (ν) for the fit. The first uncertainty is statistical, the second systematic. Couplings are defined with respect to the coupling to the channel $D^0 \to \left[K^*(892)^0\rho(770)^0\right]^{L=2}$.

	Fit Fraction [%]	$\lvert g\rvert$	$\arg(g)[^o]$
$[K^*(892)^0\rho(770)^0]^{L=0}$	$9.62 \pm 1.58 \pm 1.03$	$0.205 \pm 0.019 \pm 0.010$	$-8.5 \pm 4.7 \pm 4.4$
$[K^*(892)^0\rho(770)^0]^{L=1}$	$8.42 \pm 0.83 \pm 0.57$	$0.390 \pm 0.029 \pm 0.006$	$-91.4 \pm 4.7 \pm 4.1$
$[K^*(892)^0\rho(770)^0]^{L=2}$	$10.19 \pm 1.03 \pm 0.79$		
$[\rho(1450)^0 K^*(892)^0]^{L=0}$	$8.16 \pm 1.24 \pm 1.69$	$0.541 \pm 0.042 \pm 0.055$	$-21.8 \pm 6.5 \pm 5.5$
$K_1(1270)^+\pi^-$	$18.15 \pm 1.11 \pm 2.30$	$0.653 \pm 0.040 \pm 0.058$	$-110.7 \pm 5.1 \pm 4.9$
$K_1(1400)^+ [K^*(892)^0\pi^+]\,\pi^-$	$26.55 \pm 1.97 \pm 2.13$	$0.560 \pm 0.037 \pm 0.031$	$29.8 \pm 4.2 \pm 4.6$
$[K^+\pi^-]^{L=0}\,[\pi^+\pi^-]^{L=0}$	$20.90 \pm 1.30 \pm 1.50$		
$\alpha_{3/2}$		$0.686 \pm 0.043 \pm 0.022$	$-149.4 \pm 4.3 \pm 2.9$
β_1		$0.438 \pm 0.044 \pm 0.030$	$-132.4 \pm 6.5 \pm 3.0$
$f_{\pi\pi}$		$0.050 \pm 0.006 \pm 0.005$	$74.8 \pm 7.5 \pm 5.3$
Sum of Fit Fractions	$101.99 \pm 2.90 \pm 2.85$		
χ^2/ν	$350/239 = 1.463$		

7.7.1 Alternative parameterisations

The model finding procedure outlined in Sect. 7.3 results in ensembles of parameterisations of comparable quality and complexity. The decay chains included in the models discussed in the previous sections are included in the majority of models of acceptable quality, with further variations made by addition of further small components. The fraction of models in this ensemble containing a given decay mode are shown in Table 7.6 for the RS decay mode, with the average fit fraction associated with each decay chain also tabulated. The ensemble of RS models consists of about 200 models with χ^2 per degree-of-freedom varying between 1.21 and 1.26. Many of the decay chains in the ensemble include resonances, such as the $K_1(1270)$, decaying via radially excited vector mesons, such as the $\rho(1450)^0$ and $K^*(1410)^0$ mesons. In particular, the decay $mK_1(1270)^- \to \rho(1450)^0 K^-$ is included in the models discussed in Sect. 7.6, 7.7 and is found in the majority of the models in the ensemble. This decay channel of the $K_1(1270)^-$ meson has a strong impact at low dipion masses due to the very large width of the $\rho(1450)^0$, of about 400 MeV/c. As this decay mode has not been studied extensively in other production mechanisms of the $K_1(1270)^-$, and the ensemble is not in complete agreement as to its presence, it is perhaps useful to consider models that do not include this decay chain as an alternative parametrisation. The situation can be clarified with independent measurements of the properties of these resonances. The $a_1(1640)^+$ resonance is also found in many models in the ensemble, and is likely to be present at some level despite being outside of the phase space. This resonance will strongly interfere with the dominant $a_1(1260)^+$ component, and as the parameters of this resonance are poorly known, improved external inputs will be required to correctly constrain this component.

The coupling parameters cannot strictly be compared between different models, as in many cases these coupling parameters have a different interpretation depending on the choice of model. However, it is instructive to consider how the fit fractions vary depending on the choice of model, which are shown in Table 7.7. It is also useful to consider how the choice of model impacts upon the fitted masses and widths, which is shown in Table 7.8. The values for the model shown in Sect. 7.6 are also shown, which has compatible values with the ensemble. The variation with respect to the choice of model is characterised by the RMS of the parameters in the ensemble, and is of a comparable size to the combined systematic uncertainty from other sources on these parameters.

Table 7.6: Components present in alternative parameterisations of the RS decay mode $D^0 \to K^-\pi^+\pi^+\pi^-$, with the fraction of models in the ensemble that contain this decay mode and the associated average fit fraction. Only components that contribute to $> 5\%$ of the models in the ensemble are shown.

Mode	Fraction of models [%]	$\langle \mathcal{F} \rangle$ [%]
$K_1(1400)^- \left[\rho(1450)^0 K^-\right] \pi^+$	13.6	0.319
$K(1460)^- \left[K_2^*(1430)^0 \pi^-\right] \pi^+$	13.1	0.060
$K^*(1680)^- \left[\rho(770)^0 K^-\right] \pi^+$	13.1	0.068
$K_2^*(1430)^- \left[\rho(1450)^0 K^-\right] \pi^+$	13.1	0.096
$K_2^*(1430)^- \left[K^*(1680)^0 \pi^-\right] \pi^+$	13.1	0.133
$K_2^*(1430)^- \left[K^*(1410)^0 \pi^-\right] \pi^+$	13.1	0.123
$K_1(1400)^- \left[\rho(770)^0 K^-\right] \pi^+$	13.1	0.449
$K_1(1400)^- \left[K^*(1410)^0 \pi^-\right] \pi^+$	13.1	0.112
$a_1(1640)^+ \left[\left[\pi^+\pi^-\right]^{L=0} \pi^+\right] K^-$	12.1	2.468

The $D^0 \to K^+\pi^-\pi^-\pi^+$ ensemble consists of 108 models, all of which have a χ^2 per degree-of-freedom of less than 1.45, the best models in the ensemble having a χ^2 per degree-of-freedom of about 1.35. The fraction of models in this ensemble containing a given decay mode are shown in Table 7.9. The fit quality of the $D^0 \to K^+\pi^-\pi^-\pi^+$ models is notably worse than that of the $D^0 \to K^-\pi^+\pi^+\pi^-$ models, as there are likely to be many smaller decay modes missing from the $D^0 \to K^+\pi^-\pi^-\pi^+$ model that cannot be satisfactorily resolved given the current sample size. In particular, there should be percent level contributions from some of the decay chains present in the $D^0 \to K^-\pi^+\pi^+\pi^-$ mode, such as $D^0 \to a_1(1260)^- K^+$ and $D^0 \to K^*(892) \left[\pi^+\pi^-\right]^{L=0}$. In addition to the marginal decays of the $K_1(1270)$ present in the $D^0 \to K^+\pi^-\pi^-\pi^+$ ensemble, the models suggest contributions from the $K^*(1680)$, which due to its large width and position on the edge of the phase space, resembles a quasi-nonresonant component. As is the case for the large $D^0 \to K^*(892)^0 \rho(1450)$ component, this contribution is likely to be mimicking several smaller decay channels that cannot be resolved with the current sample size.

Table 7.7: Dependence of fit fractions (and partial fractions) on the final choice of RS model. This dependence is expressed as the mean value and the RMS of the values in the ensemble. Also shown are the fit fractions of the baseline model presented in Sect. 7.6.

	(Partial) Fraction [%] Baseline	Ensemble Mean ± RMS
$\left[\overline{K}^*(892)^0\rho(770)^0\right]^{L=0}$	$7.34 \pm 0.08 \pm 0.47$	7.10 ± 0.13
$\left[\overline{K}^*(892)^0\rho(770)^0\right]^{L=1}$	$6.03 \pm 0.05 \pm 0.25$	6.00 ± 0.12
$\left[\overline{K}^*(892)^0\rho(770)^0\right]^{L=2}$	$8.47 \pm 0.09 \pm 0.67$	8.42 ± 0.20
$\left[\rho(1450)^0\overline{K}^*(892)^0\right]^{L=0}$	$0.61 \pm 0.04 \pm 0.17$	0.65 ± 0.13
$\left[\rho(1450)^0\overline{K}^*(892)^0\right]^{L=1}$	$1.98 \pm 0.03 \pm 0.33$	1.91 ± 0.06
$\left[\rho(1450)^0\overline{K}^*(892)^0\right]^{L=2}$	$0.46 \pm 0.03 \pm 0.15$	0.46 ± 0.05
$\rho(770)^0\,[K^-\pi^+]^{L=0}$	$0.93 \pm 0.03 \pm 0.05$	1.08 ± 0.12
$\overline{K}^*(892)^0\,[\pi^+\pi^-]^{L=0}$	$2.35 \pm 0.09 \pm 0.33$	2.19 ± 0.34
$a_1(1260)^+K^-$	$38.07 \pm 0.24 \pm 1.38$	38.06 ± 2.08
$\quad\rho(770)^0\pi^+$	$89.75 \pm 0.45 \pm 1.00$	86.66 ± 4.52
$\quad[\pi^+\pi^-]^{L=0}\,\pi^+$	$2.42 \pm 0.06 \pm 0.12$	3.01 ± 1.02
$\quad[\rho(770)^0\pi^+]^{L=2}$	$0.85 \pm 0.03 \pm 0.06$	0.80 ± 0.10
$K_1(1270)^-\pi^+$	$4.66 \pm 0.05 \pm 0.39$	4.74 ± 0.24
$\quad\rho(770)^0K^-$	$96.30 \pm 1.64 \pm 6.61$	77.04 ± 9.22
$\quad\rho(1450)^0K^-$	$49.09 \pm 1.58 \pm 11.54$	34.13 ± 8.19
$\quad\omega(782)\,[\pi^+\pi^-]\,K^-$	$1.65 \pm 0.11 \pm 0.16$	1.70 ± 0.15
$\quad\overline{K}^*(892)^0\pi^-$	$27.08 \pm 0.64 \pm 2.82$	26.95 ± 2.52
$\quad\left[\overline{K}^*(892)^0\pi^-\right]^{L=2}$	$3.47 \pm 0.17 \pm 0.31$	3.57 ± 0.49
$\quad[K^-\pi^+]\,\pi^-$	$22.90 \pm 0.72 \pm 1.89$	20.39 ± 2.89
$K_1(1400)^-\left[\overline{K}^*(892)^0\pi^-\right]\pi^+$	$1.15 \pm 0.04 \pm 0.20$	1.23 ± 0.10
$K_2^*(1430)^-\left[\overline{K}^*(892)^0\pi^-\right]\pi^+$	$0.46 \pm 0.01 \pm 0.03$	0.44 ± 0.04
$K(1460)^-\pi^+$	$3.75 \pm 0.10 \pm 0.37$	3.63 ± 0.27
$\quad\overline{K}^*(892)^0\pi^-$	$51.39 \pm 1.00 \pm 1.71$	53.18 ± 1.52
$\quad[\pi^+\pi^-]^{L=0}\,K^-$	$31.23 \pm 0.83 \pm 1.78$	30.46 ± 1.19
$[K^-\pi^+]^{L=0}\,[\pi^+\pi^-]^{L=0}$	$22.04 \pm 0.28 \pm 2.09$	21.87 ± 1.51

Table 7.8: Dependence of fitted masses and widths on the final choice of RS model. This dependence is expressed as the mean value and the RMS of the values in the ensemble. The values found for the baseline model presented in Sect. 7.6 are listed for comparison

	Baseline	Ensemble
$m(a_1(1260)^+)[\,\text{MeV}/c^2]$	$1195.05 \pm 1.05 \pm 6.33$	1196.85 ± 6.21
$\Gamma(a_1(1260)^+)[\,\text{MeV}/c^2]$	$422.01 \pm 2.10 \pm 12.72$	420.92 ± 8.70
$m(K_1(1270)^-)[\,\text{MeV}/c^2]$	$1289.81 \pm 0.56 \pm 1.66$	1287.77 ± 3.97
$\Gamma(K_1(1270)^-)[\,\text{MeV}/c^2]$	$116.11 \pm 1.65 \pm 2.96$	114.27 ± 7.57
$m(K(1460)^-)[\,\text{MeV}/c^2]$	$1482.40 \pm 3.58 \pm 15.22$	1474.60 ± 12.28
$\Gamma(K(1460)^-)[\,\text{MeV}/c^2]$	$335.60 \pm 6.20 \pm 8.65$	333.89 ± 12.88

Table 7.9: Components present in alternative parameterisations of the WS decay mode $D^0 \to K^+\pi^-\pi^-\pi^+$, with the fraction of models in the ensemble that contain this decay mode and the associated average fit fraction. Only components that contribute to $> 5\%$ of the models in the ensemble are shown.

Decay Chain	Fraction of models [%]	$\langle\mathcal{F}\rangle$ [%]
$K_1(1270)^+\left[\rho(770)^0K^+\right]^{L=2}\pi^-$	47.2	1.21
$K^*(1680)^+\left[K^*(1680)^0\pi^+\right]\pi^-$	38.0	2.89
$K^*(1680)^+\left[\rho(770)^0K^+\right]\pi^-$	33.3	2.58
$a_1(1640)^-\left[\left[\pi^+\pi^-\right]^{L=0}\pi^-\right]K^+$	27.8	3.24
$K^*(1680)^+\left[\rho(1450)^0K^+\right]\pi^-$	22.2	2.53
$K_1(1270)^+\left[K^*(1410)^0\pi^+\right]^{L=2}\pi^-$	22.2	0.60
$K_1(1270)^+\left[\left[\pi^+\pi^-\right]^{L=0}K^+\right]\pi^-$	21.3	0.26
$K^*(1680)^+\left[K^*(1410)^0\pi^+\right]\pi^-$	17.6	1.98
$\rho(770)^0\left[K^+\pi^-\right]^{L=0}$	17.6	3.49
$K^*(1680)^+\left[K_2^*(1430)^0\pi^+\right]\pi^-$	16.7	0.82
$K_1(1400)^+\left[\left[\pi^+\pi^-\right]^{L=0}K^+\right]\pi^-$	13.0	0.29
$K_2^*(1430)^0\left[K^+\pi^-\right]\rho(770)^0$	13.0	0.35
$K^*(1410)^0\rho(770)^0$	10.2	3.50

7.8 Coherence factor

The coherence factor $R_{K3\pi}$ and average strong-phase difference $\delta_{K3\pi}$ were defined in Ch. 2 as measures of the phase-space averaged interference properties between suppressed and favoured amplitudes. As a reminder of the definitions of these parameters,

$$R_{K3\pi}e^{-i\delta_{K3\pi}} = \frac{\int \mathrm{d}\mathbf{x}\mathcal{A}_{D^0\to K^+\pi^-\pi^-\pi^+}(\mathbf{x})\mathcal{A}^*_{\bar{D}^0\to K^+\pi^-\pi^-\pi^+}(\mathbf{x})}{A_{D^0\to K^+\pi^-\pi^-\pi^+}A_{\bar{D}^0\to K^+\pi^-\pi^-\pi^+}} \tag{7.14}$$

where $\mathcal{A}_{D^0\to K^+\pi^-\pi^-\pi^+}$ is the amplitude of the suppressed decay and $\mathcal{A}_{\bar{D}^0\to K^+\pi^-\pi^-\pi^+}$ is the *CP*-conjugate of the favoured amplitude. The averaged suppressed amplitude is given by

$$A^2_{D^0\to K^+\pi^-\pi^-\pi^+} = \int \mathrm{d}\mathbf{x}\, |\mathcal{A}_{D^0\to K^+\pi^-\pi^-\pi^+}(\mathbf{x})|^2\,, \tag{7.15}$$

with a comparable expression for the favoured amplitude. The average ratio of amplitudes is an additional useful parameter, and was defined as

$$r_{K3\pi} = A_{D^0\to K^+\pi^-\pi^-\pi^+}/A_{\bar{D}^0\to K^+\pi^-\pi^-\pi^+}. \tag{7.16}$$

As discussed in Ch. 2, knowledge of these parameters is necessary when making use of the decays in an inclusive manner in $B^-\to DK^-$ transitions for measuring the unitarity angle γ [89], and can also be exploited for charm mixing studies. Chapter 3 presented a determination of these parameters using observables with direct sensitivity to the coherence factor and related parameters that have been measured at the $\psi(3770)$ resonance with CLEO-c data [43], and through charm mixing at LHCb [42]. The analysis of those measurements presented in Ch. 3 yielded

$$\begin{aligned} R_{K3\pi} &= 0.43^{+0.17}_{-0.13} \\ \delta_{K3\pi} &= (128^{+28}_{-17})^{\mathrm{o}} \\ r_{K3\pi} &= (5.49\pm 0.06)\times 10^{-2}. \end{aligned} \tag{7.17}$$

The models presented in this thesis can be used to calculate the model-derived coherence factor:

$$R^{\mathrm{mod}}_{K3\pi} = 0.459 \pm 0.010 \pm 0.020. \tag{7.18}$$

where the first uncertainty is statistical, and the second is the systematic uncertainty from the choice of WS model, which is assigned by taking the spread in values from an ensemble of alternative models from the model building algorithm, requiring that models have a χ^2 per degree of freedom of less than 1.5, and that all unconstrained components in the fit have a significance of $> 2\sigma$. This result is in good agreement with the direct measurement. There is no sensitivity to $\delta_{K3\pi}$ and $r_{K3\pi}$ as the amplitude models are evaluated separately for RS and WS decays.

The stability of the local phase description can also be verified by evaluating the model-derived coherence factor and associated parameters in different regions of phase space. This is equivalent to changing the definition of Eq. 7.14 such that integrals are performed over some limited region rather than the entire phase space. In this case, it is also possible to determine the local values of $\delta_{K3\pi}$ and $r_{K3\pi}$ relative

Table 7.10: Summary of coherence factor and average strong-phase difference with spread of coherence factor and average strong phase from choice of WS model characterised with the RMS of the distribution assigned as the uncertainty.

Bin	$R_{K3\pi}$	$\delta_{K3\pi}[^{\circ}]$	$r_{K3\pi} \times 10^{-2}$
1	0.701 ± 0.017	169 ± 3	5.287 ± 0.034
2	0.691 ± 0.016	151 ± 1	5.679 ± 0.032
3	0.726 ± 0.010	133 ± 1	6.051 ± 0.032
4	0.742 ± 0.008	117 ± 1	6.083 ± 0.030
5	0.783 ± 0.005	102 ± 2	5.886 ± 0.031
6	0.764 ± 0.007	84 ± 3	5.727 ± 0.033
7	0.424 ± 0.013	26 ± 3	5.390 ± 0.061
8	0.473 ± 0.030	-149 ± 7	4.467 ± 0.065

to the phase-space averaged values. Therefore, overall normalisation factors are fixed such that the central value of the direct measurement is correctly reproduced.

In order to define these regions, the space is divided into hypercubes using the algorithm described in Sect. 7.2. The division is done such that the hypercubes cannot be smaller in any dimension than $50\,\mathrm{MeV}/c^2$. The hypercubes are grouped into bins of average phase difference between the two amplitudes in the bin, using the baseline amplitude models described in Sect. 7.6 and Sect. 7.7. These bins will not generally be contiguous in the phase space, and therefore visualising the bins is not instructive. The range $[-180^{\circ}, 180^{\circ}]$ in strong-phase difference is split into eight bins. The division of this range is done such that each bin is expected to have an approximately equal population of WS events within the bin. The coherence factors, average strong-phase differences and their RMS spread arising from the choice of WS model are summarised in Table 7.10. Good stability is observed, which is a consequence of the dominant features of the amplitude being common for all models, and gives confidence to using the models presented in this paper to define regions of interest for future binned measurements of γ or studies of charm mixing. The relatively high coherence factor in some regions of phase-space demonstrates the potential improvements in sensitivity to measurements of CP-violating observables for such measurements.

8

Conclusions and outlook

Several studies of the four-body decays $D^0 \to K^{\mp}\pi^{\pm}\pi^{\pm}\pi^{\mp}$ have been presented in this thesis, including both model-independent determinations of hadronic factors used in studies of the unitarity angle γ and detailed model-dependent studies of the resonant structure of the two decay modes.

A model independent determination of the coherence factor and associated hadronic parameters was presented in Ch. 3 using the CLEO-c data set and constraints from charm mixing, and represents a significant improvement on previous determinations of these parameters.

Chapter 7 presents the most precise amplitude analysis of the $D^0 \to K^-\pi^+\pi^+\pi^-$ decay mode to date, with one of the largest samples of any charm decay mode ever studied using an amplitude analysis. This revealed several notable results, including a quasi-model-independent confirmation of the first radial excitation of the kaon, the $K(1460)$. The first amplitude analysis ever of the decay mode $D^0 \to K^+\pi^-\pi^-\pi^+$ was also presented, which is also one of the few studies of a resonant sub-structure of a doubly Cabibbo-suppressed amplitude. Both amplitudes are found to have large contributions from axial resonances, the decays $D^0 \to a_1(1260)^+K^-$ and $D^0 \to K_1(1270/1400)^+\pi^-$ for $D^0 \to K^-\pi^+\pi^+\pi^-$and $D^0 \to K^+\pi^-\pi^-\pi^+$, respectively. This is consistent with the general picture that colour-favoured W-emission topologies are crucial in describing these decays.

The coherence factor is calculated using the two amplitude models, and found to be in excellent agreement with the model-independent determination described in

Ch. 3. The values of the coherence factor both globally and in regions of phase space are found to be relatively stable with respect to alternative parameterisations of the amplitudes. This gives confidence that these models provide stable predictions that can be used to improve knowledge of several important electroweak parameters. Firstly, the rates of the decay modes $B^{\pm} \to D[K^{\mp}\pi^{\pm}\pi^{\pm}\pi^{\mp}]K^{\pm}$ can be studied locally in the four-body phase-space of the D-meson decay in order to improve knowledge of the unitarity angle γ. Secondly, the time evolution of the WS decay mode $D^0 \to K^+\pi^-\pi^-\pi^+$ amplitude can be exploited to make improved measurements of the charm mixing parameters (x, y). There are several possible strategies for exploiting these models in such measurements. The first is to make model-dependent measurements of the various electroweak parameters of interest. However, great care must be taken in the evaluation of systematic uncertainties associated with the theoretical limitations of amplitude models. Hence, a perhaps preferable strategy is to use the models to inspire binning schemes in which to make model-independent measurements of the *CP*-violating phase γ and of charm mixing, utilising external constraints on the coherence factors and average strong-phase differences in these bins from CLEO-c or perhaps BES III.

From the perspective of future improvements to these models, larger sample sizes are unlikely to improve knowledge of the RS amplitude. However, the robustness of models can perhaps be improved by considering the amplitudes of several different decay modes simultaneously. For example, including the coupled channels $D^0 \to K^{\mp}K^{\pm}K^{\mp}\pi^{\pm}$ in a global fit, which despite its limited phase space perhaps offers interesting additional constraints on the coupled isoscalar states. An alternative approach is to make comparisons with decay modes where some amplitudes can be related by isospin arguments, such as $D^0 \to K^*(892)^0\,[K^0_{\mathrm{S}}\pi^0]\,\pi^+\pi^-$. Knowledge of the WS amplitude will surely be improved by studies with larger sample sizes, for which the model described in this thesis provides a solid starting point. Such studies will be required to take into account the effects of $D^0\overline{D}^0$ mixing.

Measurements of the unitarity triangle are entering an era of precision where discrepancies with the Standard Model may be observed. An improved understanding of multi-body hadronic systems, such as those presented in this thesis, is one of the myriad of efforts necessary to reduce uncertainties to the level where new physics sources of *CP*-violation can be observed.

Appendices

The various contributions assigned for different systematic uncertainties are summarised in this appendix by a series of tables. The legend for these is given in Table 1, including which sources of uncertainty are considered on each decay mode. The breakdown of systematic uncertainties for the RS decay $D^0 \to K^-\pi^+\pi^+\pi^-$for coupling parameters, fit fractions and other parameters are given in Tables 2 and 3 for the quasi two-body decay chains and cascade decay chains, respectively. The systematic uncertainties for the WS mode $D^0 \to K^+\pi^-\pi^-\pi^+$are given in Table 4 for both coupling parameters and the fit fractions.

Table 1: Legend for systematic uncertainties, including whether this sources of uncertainty is considered on the RS/WS decay mode.

	Description	RS	WS
I	Efficiency variations	✓	
II	Simulation statistics	✓	✓
III	Masses and widths	✓	✓
IV	Form factor radii	✓	✓
V	Background fraction	✓	✓
VI	Background parameterisation		✓
VII	RS parameters		✓

Table 2: Systematic uncertainties on the RS decay coupling parameters and fit fractions for quasi two-body decay chains.

			I	II	III	IV	V
$\overline{K}^{*}(892)^0\rho(770)^0$	$\mathcal{F}$	$7.340 \pm 0.084 \pm 0.637$	0.426	0.050	0.063	0.466	0.025
	$\lvert g\rvert$	$0.196 \pm 0.001 \pm 0.015$	0.000	0.001	0.001	0.015	0.000
	$arg(g)[^o]$	$-22.363 \pm 0.361 \pm 1.644$	1.309	0.239	0.119	0.955	0.075
$\left[\overline{K}^{*}(892)^0\rho(770)^0\right]^{L=1}$	$\mathcal{F}$	$6.031 \pm 0.049 \pm 0.436$	0.358	0.029	0.061	0.239	0.006
	$\lvert g\rvert$	$0.362 \pm 0.002 \pm 0.010$	0.002	0.001	0.002	0.009	0.000
	$arg(g)[^o]$	$-102.907 \pm 0.380 \pm 1.667$	1.431	0.224	0.321	0.760	0.025
$\left[\overline{K}^{*}(892)^0\rho(770)^0\right]^{L=2}$	$\mathcal{F}$	$8.475 \pm 0.086 \pm 0.826$	0.492	0.051	0.059	0.659	0.023
$\rho(1450)^0\overline{K}^{*}(892)^0$	$\mathcal{F}$	$0.608 \pm 0.040 \pm 0.165$	0.061	0.032	0.134	0.065	0.019
	$\lvert g\rvert$	$0.162 \pm 0.005 \pm 0.025$	0.007	0.004	0.018	0.015	0.003
	$arg(g)[^o]$	$-86.122 \pm 1.852 \pm 4.345$	1.933	1.570	2.485	2.152	1.368
$\left[\rho(1450)^0\overline{K}^{*}(892)^0\right]^{L=1}$	$\mathcal{F}$	$1.975 \pm 0.029 \pm 0.351$	0.115	0.017	0.315	0.103	0.003
	$\lvert g\rvert$	$0.643 \pm 0.006 \pm 0.058$	0.001	0.003	0.050	0.029	0.001
	$arg(g)[^o]$	$97.304 \pm 0.516 \pm 2.770$	2.249	0.288	1.341	0.854	0.031
$\left[\rho(1450)^0\overline{K}^{*}(892)^0\right]^{L=2}$	$\mathcal{F}$	$0.455 \pm 0.028 \pm 0.163$	0.078	0.016	0.090	0.110	0.004
	$\lvert g\rvert$	$0.649 \pm 0.021 \pm 0.105$	0.052	0.011	0.063	0.065	0.003
	$arg(g)[^o]$	$-15.564 \pm 1.960 \pm 4.109$	1.208	1.323	2.631	2.484	0.762
$\rho(770)^0\,[K^-\pi^+]^{L=0}$	$\mathcal{F}$	$0.926 \pm 0.032 \pm 0.083$	0.069	0.019	0.016	0.039	0.006
	$\lvert g\rvert$	$0.338 \pm 0.006 \pm 0.011$	0.000	0.004	0.002	0.010	0.002
	$arg(g)[^o]$	$73.048 \pm 0.795 \pm 3.951$	3.567	0.469	0.481	1.549	0.185
$\alpha_{3/2}$	$\lvert g\rvert$	$1.073 \pm 0.008 \pm 0.021$	0.018	0.005	0.005	0.009	0.003
	$arg(g)[^o]$	$-130.856 \pm 0.457 \pm 1.786$	1.679	0.282	0.274	0.435	0.155
$\overline{K}^{*}(892)^0\,[\pi^+\pi^-]^{L=0}$	$\mathcal{F}$	$2.347 \pm 0.089 \pm 0.557$	0.483	0.079	0.148	0.206	0.076
$f_{\pi\pi}$	$\lvert g\rvert$	$0.261 \pm 0.005 \pm 0.024$	0.022	0.004	0.006	0.007	0.003
	$arg(g)[^o]$	$-149.023 \pm 0.943 \pm 2.696$	2.275	0.540	1.176	0.617	0.196
β_1	$\lvert g\rvert$	$0.305 \pm 0.011 \pm 0.046$	0.040	0.010	0.013	0.013	0.007
	$arg(g)[^o]$	$65.554 \pm 1.534 \pm 4.004$	3.017	0.857	2.322	0.771	0.455
$[K^-\pi^+]^{L=0}\,[\pi^+\pi^-]^{L=0}$	$\mathcal{F}$	$22.044 \pm 0.282 \pm 4.137$	3.631	0.268	0.213	1.945	0.188
$\alpha_{3/2}$	$\lvert g\rvert$	$0.870 \pm 0.010 \pm 0.030$	0.029	0.005	0.003	0.004	0.002
	$arg(g)[^o]$	$-149.187 \pm 0.712 \pm 3.503$	3.467	0.350	0.250	0.194	0.157
$\alpha_{K\eta'}$	$\lvert g\rvert$	$2.614 \pm 0.141 \pm 0.281$	0.263	0.063	0.041	0.062	0.018
	$arg(g)[^o]$	$-19.073 \pm 2.414 \pm 11.979$	11.775	1.507	1.151	0.816	0.755
β_1	$\lvert g\rvert$	$0.554 \pm 0.009 \pm 0.053$	0.019	0.005	0.004	0.050	0.002
	$arg(g)[^o]$	$35.310 \pm 0.662 \pm 1.627$	0.969	0.439	0.588	1.069	0.168
$f_{\pi\pi}$	$\lvert g\rvert$	$0.082 \pm 0.001 \pm 0.008$	0.004	0.001	0.001	0.007	0.000
	$arg(g)[^o]$	$-146.991 \pm 0.718 \pm 2.248$	1.849	0.463	0.593	1.003	0.252

Table 3: Systematic uncertainties on the RS decay coupling parameters, fit fractions and masses and widths of resonances for cascade topology decay chains.

			I	II	III	IV	V
$a_1(1260)^+\mathrm{K}^-$	$\mathcal{F}$	$38.073 \pm 0.245 \pm 2.594$	2.198	0.155	0.171	1.356	0.053
	$\|g\|$	$0.813 \pm 0.006 \pm 0.025$	0.002	0.003	0.004	0.024	0.001
	$\arg(g)[^o]$	$-149.155 \pm 0.453 \pm 3.132$	2.628	0.321	0.531	1.579	0.162
$\rho(770)^0\pi^+$	$\mathcal{F}$	$89.745 \pm 0.452 \pm 1.498$	1.116	0.298	0.596	0.720	0.192
$[\pi^+\pi^-]^{L=0}\,\pi^+$	$\mathcal{F}$	$2.420 \pm 0.060 \pm 0.202$	0.165	0.043	0.037	0.102	0.010
β_1	$\|g\|$	$0.991 \pm 0.018 \pm 0.037$	0.005	0.015	0.012	0.031	0.006
	$\arg(g)[^o]$	$-22.185 \pm 1.044 \pm 1.195$	0.769	0.597	0.393	0.545	0.169
β_0	$\|g\|$	$0.291 \pm 0.007 \pm 0.017$	0.012	0.006	0.003	0.010	0.001
	$\arg(g)[^o]$	$165.819 \pm 1.325 \pm 3.076$	2.155	0.802	0.819	1.845	0.318
$f_{\pi\pi}$	$\|g\|$	$0.117 \pm 0.002 \pm 0.007$	0.001	0.002	0.002	0.007	0.001
	$\arg(g)[^o]$	$170.501 \pm 1.235 \pm 2.243$	0.151	0.765	0.960	1.722	0.731
$[\rho(770)^0\pi^+]^{L=2}$	$\mathcal{F}$	$0.850 \pm 0.032 \pm 0.077$	0.058	0.021	0.023	0.040	0.007
	$\|g\|$	$0.582 \pm 0.011 \pm 0.027$	0.020	0.007	0.008	0.015	0.002
	$\arg(g)[^o]$	$-152.829 \pm 1.195 \pm 2.512$	1.691	0.710	0.755	1.520	0.258
$a_1(1260)^+$	$m_0\,[\mathrm{MeV}/c^2]$	$1195.050 \pm 1.045 \pm 6.333$	3.187	0.784	0.497	5.371	0.493
	$\Gamma_0\,[\mathrm{MeV}/c^2]$	$422.013 \pm 2.096 \pm 12.723$	2.638	1.335	0.723	12.341	0.549
$K_1(1270)^-\pi^+$	$\mathcal{F}$	$4.664 \pm 0.053 \pm 0.624$	0.485	0.037	0.285	0.268	0.012
	$\|g\|$	$0.362 \pm 0.004 \pm 0.015$	0.013	0.002	0.002	0.008	0.001
	$\arg(g)[^o]$	$114.207 \pm 0.760 \pm 3.612$	3.320	0.526	0.441	1.227	0.219
$\rho(770)^0\mathrm{K}^-$	$\mathcal{F}$	$96.301 \pm 1.644 \pm 8.237$	5.523	1.082	5.624	2.110	0.286
$\rho(1450)^0\mathrm{K}^-$	$\mathcal{F}$	$49.089 \pm 1.580 \pm 13.727$	7.467	1.062	11.159	2.611	0.452
	$\|g\|$	$2.016 \pm 0.026 \pm 0.211$	0.108	0.017	0.172	0.053	0.007
	$\arg(g)[^o]$	$-119.504 \pm 0.856 \pm 2.333$	1.597	0.489	1.102	1.190	0.146
$\overline{K}^*(892)^0\pi^-$	$\mathcal{F}$	$27.082 \pm 0.639 \pm 4.039$	2.943	0.410	2.525	1.046	0.097
	$\|g\|$	$0.388 \pm 0.007 \pm 0.033$	0.025	0.004	0.017	0.011	0.001
	$\arg(g)[^o]$	$-172.577 \pm 1.087 \pm 5.957$	5.653	0.712	1.482	0.876	0.255
$[\mathrm{K}^-\pi^+]^{L=0}\pi^-$	$\mathcal{F}$	$22.899 \pm 0.722 \pm 3.091$	2.483	0.457	1.490	0.973	0.119
	$\|g\|$	$0.554 \pm 0.010 \pm 0.037$	0.033	0.007	0.005	0.015	0.001
	$\arg(g)[^o]$	$53.170 \pm 1.068 \pm 1.920$	1.564	0.659	0.401	0.735	0.323
$\left[\overline{K}^*(892)^0\pi^-\right]^{L=2}$	$\mathcal{F}$	$3.465 \pm 0.168 \pm 0.469$	0.362	0.117	0.204	0.176	0.043
	$\|g\|$	$0.769 \pm 0.021 \pm 0.048$	0.035	0.014	0.011	0.027	0.004
	$\arg(g)[^o]$	$-19.286 \pm 1.616 \pm 6.657$	6.463	1.013	0.914	0.800	0.207
$\omega(782)\,[\pi^+\pi^-]\,\mathrm{K}^-$	$\mathcal{F}$	$1.649 \pm 0.109 \pm 0.228$	0.161	0.083	0.120	0.069	0.007
	$\|g\|$	$0.146 \pm 0.005 \pm 0.009$	0.006	0.004	0.002	0.004	0.000
	$\arg(g)[^o]$	$9.041 \pm 2.114 \pm 5.673$	5.401	1.402	0.587	0.826	0.126
$K_1(1270)^-$	$m_0\,[\mathrm{MeV}/c^2]$	$1289.810 \pm 0.558 \pm 1.656$	1.197	0.436	0.244	1.010	0.198
	$\Gamma_0\,[\mathrm{MeV}/c^2]$	$116.114 \pm 1.649 \pm 2.963$	1.289	1.221	0.981	2.090	0.545
$K_1(1400)^-\left[\overline{K}^*(892)^0\pi^-\right]\pi^+$	$\mathcal{F}$	$1.147 \pm 0.038 \pm 0.205$	0.079	0.022	0.181	0.049	0.003
	$\|g\|$	$0.127 \pm 0.002 \pm 0.011$	0.002	0.001	0.010	0.005	0.000
	$\arg(g)[^o]$	$-169.822 \pm 1.102 \pm 5.879$	2.052	0.687	5.343	1.124	0.270
$K_2^*(1430)^-\left[\overline{K}^*(892)^0\pi^-\right]\pi^+$	$\mathcal{F}$	$0.458 \pm 0.011 \pm 0.041$	0.031	0.007	0.010	0.024	0.001
	$\|g\|$	$0.302 \pm 0.004 \pm 0.011$	0.005	0.002	0.003	0.009	0.000
	$\arg(g)[^o]$	$-77.690 \pm 0.732 \pm 2.051$	0.898	0.409	1.174	1.360	0.051
$K(1460)^-\pi^+$	$\mathcal{F}$	$3.749 \pm 0.095 \pm 0.803$	0.717	0.066	0.076	0.341	0.064
	$\|g\|$	$0.122 \pm 0.002 \pm 0.012$	0.002	0.001	0.002	0.012	0.001
	$\arg(g)[^o]$	$172.675 \pm 2.227 \pm 8.208$	6.826	2.235	2.413	2.619	1.761
$\overline{K}^*(892)^0\pi^-$	$\mathcal{F}$	$51.387 \pm 0.996 \pm 9.581$	9.490	0.529	0.629	0.974	0.333
$[\pi^+\pi^-]^{L=0}\,\mathrm{K}^-$	$\mathcal{F}$	$31.228 \pm 0.833 \pm 11.085$	11.021	0.454	0.414	0.989	0.247
f_{KK}	$\|g\|$	$1.819 \pm 0.059 \pm 0.189$	0.180	0.027	0.030	0.036	0.025
	$\arg(g)[^o]$	$-80.790 \pm 2.225 \pm 6.563$	5.820	1.617	1.740	1.361	1.305
β_1	$\|g\|$	$0.813 \pm 0.032 \pm 0.136$	0.132	0.016	0.018	0.018	0.015
	$\arg(g)[^o]$	$112.871 \pm 2.555 \pm 9.487$	8.636	2.025	2.241	1.817	1.730
β_0	$\|g\|$	$0.315 \pm 0.010 \pm 0.022$	0.019	0.005	0.005	0.009	0.002
	$\arg(g)[^o]$	$46.734 \pm 1.946 \pm 2.952$	1.110	1.576	1.416	1.121	1.318
$K(1460)^-$	$m_0\,[\mathrm{MeV}/c^2]$	$1482.400 \pm 3.576 \pm 15.216$	13.873	3.466	3.216	3.611	1.916
	$\Gamma_0\,[\mathrm{MeV}/c^2]$	$335.595 \pm 6.196 \pm 8.651$	1.524	4.234	2.017	5.901	3.962

Table 4: Systematic uncertainties on the WS decay coupling parameters and fit fractions.

			II	III	IV	V	VI	VII
$K^*(892)^0\rho(770)^0$	$\|g\|$	$0.205 \pm 0.019 \pm 0.010$	0.002	0.006	0.003	0.001	0.005	0.006
	$\arg(g)[^o]$	$-8.502 \pm 4.662 \pm 4.439$	0.433	1.272	0.112	0.148	4.150	0.799
	$\mathcal{F}$	$9.617 \pm 1.584 \pm 1.028$	0.134	0.436	0.344	0.069	0.567	0.637
$[K^*(892)^0\rho(770)^0]^{L=1}$	$\|g\|$	$0.390 \pm 0.029 \pm 0.006$	0.002	0.003	0.000	0.001	0.004	0.003
	$\arg(g)[^o]$	$-91.359 \pm 4.728 \pm 4.132$	0.406	0.827	0.128	0.101	3.951	0.766
	$\mathcal{F}$	$8.424 \pm 0.827 \pm 0.573$	0.069	0.091	0.210	0.020	0.458	0.249
$[K^*(892)^0\rho(770)^0]^{L=2}$	$\mathcal{F}$	$10.191 \pm 1.028 \pm 0.789$	0.089	0.130	0.255	0.018	0.658	0.314
$\rho(1450)^0K^*(892)^0$	$\|g\|$	$0.541 \pm 0.042 \pm 0.055$	0.004	0.043	0.018	0.001	0.024	0.016
	$\arg(g)[^o]$	$-21.798 \pm 6.536 \pm 5.483$	0.573	4.532	0.547	0.254	0.254	2.960
	$\mathcal{F}$	$8.162 \pm 1.242 \pm 1.686$	0.107	1.381	0.474	0.031	0.718	0.428
$K_1(1270)^+\pi^-$	$\|g\|$	$0.653 \pm 0.040 \pm 0.058$	0.004	0.017	0.009	0.001	0.049	0.024
	$\arg(g)[^o]$	$-110.715 \pm 5.054 \pm 4.854$	0.481	1.484	0.219	0.056	4.236	1.770
	$\mathcal{F}$	$18.147 \pm 1.114 \pm 2.301$	0.104	0.800	0.423	0.021	1.788	1.125
$K_1(1400)^+\,[K^*(892)^0\pi^+]\,\pi^-$	$\|g\|$	$0.560 \pm 0.037 \pm 0.031$	0.003	0.020	0.011	0.001	0.018	0.010
	$\arg(g)[^o]$	$29.769 \pm 4.220 \pm 4.565$	0.396	4.055	0.211	0.060	1.638	1.227
	$\mathcal{F}$	$26.549 \pm 1.973 \pm 2.128$	0.190	1.715	0.469	0.046	0.940	0.667
$[K^+\pi^-]^{L=0}\,[\pi^+\pi^-]^{L=0}$	$\mathcal{F}$	$20.901 \pm 1.295 \pm 1.500$	0.129	0.328	0.565	0.134	1.246	0.486
$\alpha_{3/2}$	$\|g\|$	$0.686 \pm 0.043 \pm 0.022$	0.004	0.007	0.002	0.002	0.019	0.007
	$\arg(g)[^o]$	$-149.399 \pm 4.260 \pm 2.946$	0.502	0.277	0.181	0.082	2.809	0.651
β_1	$\|g\|$	$0.438 \pm 0.044 \pm 0.030$	0.004	0.006	0.010	0.001	0.026	0.010
	$\arg(g)[^o]$	$-132.424 \pm 6.507 \pm 2.972$	0.618	1.109	0.357	0.200	2.382	1.174
$f_{\pi\pi}$	$\|g\|$	$0.050 \pm 0.006 \pm 0.005$	0.001	0.001	0.001	0.000	0.004	0.002
	$\arg(g)[^o]$	$74.821 \pm 7.528 \pm 5.282$	0.695	0.745	0.149	0.472	5.050	1.058

Bibliography

[1] G. D. Rochester and C. C. Butler, *Evidence for the existence of new unstable elementary particles*, Nature **160** (1947) 855.

[2] H. Yukawa, *On the interaction of elementary particles I*, Proc. Phys. Math. Soc. Jap. **17** (1935) 48, [Prog. Theor. Phys. Suppl.1,1(1935)].

[3] C. M. G. Lattes, H. Muirhead, G. P. S. Occhialini, and C. F. Powell, *Processes involving charged mesons*, Nature **159** (1947) 694.

[4] T. D. Lee and C. N. Yang, *Question of parity conservation in weak interactions*, Phys. Rev. **104** (1956) 254.

[5] C. S. Wu *et al.*, *Experimental test of parity conservation in Beta decay*, Physical Review **105** (1957) 1413.

[6] M. Gell-Mann, *The Eightfold Way: A theory of strong interaction symmetry*, .

[7] G. Zweig, *An* SU(3) *model for strong interaction symmetry and its breaking*, Tech. Rep. CERN-TH-401, CERN, Geneva, Jan, 1964.

[8] Belle collaboration, S. K. Choi *et al.*, *Observation of a narrow charmonium - like state in exclusive $B^{\pm} \to K^{\pm}\pi^{+}\pi^{-}J/\psi$ decays*, Phys. Rev. Lett. **91** (2003) 262001, `arXiv:hep-ex/0309032`.

[9] LHCb, R. Aaij *et al.*, *Observation of $J/\psi p$ resonances consistent with pentaquark states in $\Lambda_b^0 \to J/\psi K^- p$ decays*, Phys. Rev. Lett. **115** (2015) 072001, `arXiv:1507.03414`.

[10] S. L. Glashow, J. Iliopoulos, and L. Maiani, *Weak interactions with lepton-hadron symmetry*, Phys. Rev. D **2** (1970) 1285.

[11] J. J. Aubert *et al.*, *Experimental observation of a heavy particle J*, Phys. Rev. Lett. **33** (1974) 1404.

[12] J. E. Augustin *et al.*, *Discovery of a narrow resonance in e^+e^- annihilation*, Phys. Rev. Lett. **33** (1974) 1406.

[13] J. H. Christenson, J. W. Cronin, V. L. Fitch, and R. Turlay, *Evidence for the 2π decay of the K_2^0 Meson*, Phys. Rev. Lett. **13** (1964) 138.

[14] M. Kobayashi and T. Maskawa, *CP violation in the renormalizable theory of weak interaction*, Prog. Theor. Phys. **49** (1973) 652.

[15] N. Cabibbo, *Unitary symmetry and nonleptonic decays*, Phys. Rev. Lett. **12** (1964) 62.

[16] S. W. Herb *et al.*, *Observation of a dimuon resonance at 9.5-GeV in 400-GeV proton-nucleus collisions*, Phys. Rev. Lett. **39** (1977) 252.

[17] S. Abachi *et al.*, *Search for high mass top quark production in pp collisions at s = 1.8 TeV* , Physical Review Letters **74** (1995) 2422, `arXiv:hep-ex/9411001`.

[18] F. Abe *et al.*, *Observation of Top Quark Production in p p Collisions with the Collider Detector at Fermilab*, Physical Review Letters **74** (1995) 2626, `arXiv:hep-ex/9503002`.

[19] J. Schwinger, *The theory of quantized fields. I*, Phys. Rev. **82** (1951) 914.

[20] A. D. Sakharov, *Violation of CP invariance, C-asymmetry, and baryon asymmetry of the universe*, Soviet Physics Uspekhi **34** (1991), no. 5 392.

[21] G. 't Hooft, *Symmetry breaking through Bell-Jackiw anomalies*, Phys. Rev. Lett. **37** (1976) 8.

[22] CKMfitter group, J. Charles *et al.*, *CP violation and the CKM matrix: Assessing the impact of the asymmetric B factories*, Eur. Phys. J. **C41** (2005), no. 1 1, `arXiv:hep-ph/0406184`, updated results and plots available at.

[23] Heavy Flavor Averaging Group, Y. Amhis *et al.*, *Averages of b-hadron, c-hadron, and τ-lepton properties as of summer 2014*, `arXiv:1412.7515`, updated results and plots available at `http://www.slac.stanford.edu/xorg/hfag/`.

[24] Belle, BaBar collaborations, A. J. Bevan *et al.*, *The physics of the B factories*, Eur. Phys. J. **C74** (2014) 3026, `arXiv:1406.6311`.

[25] BaBar collaboration, B. Aubert *et al.*, *Measurement of time-dependent CP asymmetry in $B^0 \to c\bar{c}K^{*0}$ decays*, Phys. Rev. **D79** (2009) 072009, `arXiv:0902.1708`.

[26] I. Adachi *et al.*, *Precise measurement of the CP violation parameter* $\sin(2\phi_1)$ *in* $B^0 \to c\bar{c}K^0$ *decays*, Phys. Rev. Lett. **108** (2012) 171802, `arXiv:1201.4643`.

[27] LHCb collaboration, R. Aaij *et al.*, *Measurement of CP violation in* $B^0 \to J/\psi K^0_\mathrm{S}$ *decays*, Phys. Rev. Lett. **115** (2015), no. 3 031601, `arXiv:1503.07089`.

[28] LHCb collaboration, R. Aaij *et al.*, *Measurement of the CKM angle* γ *from a combination of LHCb results*, JHEP **12** (2016) 087, `arXiv:1611.03076`.

[29] BaBar collaboration, J. P. Lees *et al.*, *Observation of direct CP violation in the measurement of the Cabibbo-Kobayashi-Maskawa angle gamma with* $B^\pm \to D^{(*)}K^{(*)\pm}$ *decays*, Phys. Rev. **D87** (2013), no. 5 052015, `arXiv:1301.1029`.

[30] LHCb collaboration, *Update of the LHCb combination of the CKM angle* γ *using* $B \to DK$ *decays*, Tech. Rep. LHCb-CONF-2017-004, CERN, 2017.

[31] M. Gronau and D. Wyler, *On determining a weak phase from charged B decay asymmetries*, Phys. Lett. B **265** (1991) 172 .

[32] D. Atwood, I. Dunietz, and A. Soni, *Enhanced CP violation with* $B \to KD^0(\overline{D}^0)$ *modes and extraction of the CKM angle* γ, Phys. Rev. Lett. **78** (1997) 3257, `arXiv:hep-ph/9612433`.

[33] D. Atwood and A. Soni, *Role of a charm factory in extracting CKM-phase information via* $B \to$ DK, Phys. Rev. D **68** (2003) 033003.

[34] Particle Data Group, K. A. Olive *et al.*, *Review of particle physics*, Chin. Phys. **C38** (2014) 090001.

[35] S. Godfrey and N. Isgur, *Mesons in a relativized quark model with chromodynamics*, Phys. Rev. **D32** (1985) 189.

[36] M. Suzuki, *Strange axial-vector mesons*, Phys. Rev. **D47** (1993) 1252.

[37] ACCMOR collaboration, C. Daum *et al.*, *Diffractive Production of* 3π *States at 63* GeV *and 94* GeV, Nucl. Phys. **B182** (1981) 269.

[38] G. W. Brandenburg *et al.*, *Evidence for a new strangeness-one pseudoscalar meson*, Phys. Rev. Lett. **36** (1976) 1239.

[39] ACCMOR collaboration, C. Daum *et al.*, *Diffractive production of strange mesons at* 63 *GeV*, Nucl. Phys. **B187** (1981) 1.

[40] CLEO collaboration, N. Lowrey *et al.*, *Determination of the $D^0 \to K^-\pi^+\pi^0$ and $D^0 \to K^-\pi^+\pi^+\pi^-$ Coherence Factors and Average Strong-Phase Differences Using Quantum-Correlated Measurements*, Phys. Rev. **D80** (2009) 031105, `arXiv:0903.4853`.

[41] J. Libby *et al.*, *New determination of the $D^0 \to K^-\pi^+\pi^0$ and $D^0 \to K^-\pi^+\pi^+\pi^-$ coherence factors and average strong-phase differences*, Phys. Lett. **B731** (2014) 197, `arXiv:1401.1904`.

[42] LHCb collaboration, R. Aaij *et al.*, *First observation of D^0 oscillations in $D^0 \to K^+\pi^-\pi^-\pi^+$ decays and measurement of the associated coherence parameters*, `arXiv:1602.07224`.

[43] T. Evans *et al.*, *Improved determination of the $D \to K^-\pi^+\pi^+\pi^-$ coherence factor and associated hadronic parameters from a combination of $e^+e^- \to \psi(3770) \to c\bar{c}$ and $pp \to c\bar{c}X$ data*, Phys. Lett. **B757** (2016) 520, `arXiv:1602.07430`, [Erratum: Phys. Lett. **B765** (2017) 402].

[44] Heavy Flavor Averaging Group (HFAG), Y. Amhis *et al.*, *Averages of b-hadron, c-hadron, and τ-lepton properties as of summer 2014*, `arXiv:1412.7515`.

[45] CLEO collaboration, J. Libby *et al.*, *Model-independent determination of the strong-phase difference between D^0 and $\bar{D}^0 \to K^0_{S,L}h^+h^-$ ($h = \pi, K$) and its impact on the measurement of the CKM angle γ/ϕ_3*, Phys. Rev. **D82** (2010) 112006, `arXiv:1010.2817`.

[46] BaBar collaboration, B. Aubert *et al.*, *Improved measurement of the CKM angle γ in $B^\mp \to D^{(*)}K^{(*)\mp}$ decays with a Dalitz plot analysis of D decays to $K^0_S\pi^+\pi^-$ and $K^0_SK^+K^-$*, Phys. Rev. **D78** (2008) 034023, `arXiv:0804.2089`.

[47] CLEO collaboration, R. A. Briere *et al.*, *CLEO-c and CESR-c: A new frontier of weak and strong interactions*, Cornell LEPP Report CLNS-01-1742 (2001).

[48] CLEO collaboration, D. Besson *et al.*, *Measurement of $\sigma(e^+e^- \to \psi(3770) \to$ hadrons) at $E_{c.m.}$ = 3773* MeV, Phys. Rev. Lett. **96** (2006) 092002, `arXiv:1004.1358`, [Erratum: Phys. Rev. Lett.104,159901(2010)].

[49] D. J. Lange, *The EvtGen particle decay simulation package*, Nucl. Instrum. Meth. **A462** (2001) 152.

[50] R. Brun *et al.*, *GEANT 3.21, CERN program library long writeup W5013*, unpublished.

[51] CLEO collaboration, G. Bonvicini *et al.*, *Updated measurements of absolute D^+ and D^0 hadronic branching fractions and $\sigma(e^+e^- \to D\overline{D})$ at $E_{\rm cm} = 3774$ MeV*, Phys. Rev. **D89** (2014), no. 7 072002, `arXiv:1312.6775`, [Erratum: Phys. Rev.D91,no.1,019903(2015)].

[52] M. Nayak *et al.*, *First determination of the CP content of $D \to \pi^+\pi^-\pi^0$ and $D \to K^+K^-\pi^0$*, Phys. Lett. **B740** (2015) 1, `arXiv:1410.3964`.

[53] CLEO collaboration, S. Dobbs *et al.*, *Measurement of absolute hadronic branching fractions of D mesons and $e^+e^- \to D\overline{D}$ cross-sections at the $\psi(3770)$* , Phys. Rev. **D76** (2007) 112001, `arXiv:0709.3783`.

[54] C. Elsasser, *$b\bar{b}$ production at the LHCb experiment, provided by the LHCb Speakers' Bureau*, .

[55] LHCb collaboration, R. Aaij *et al.*, *LHCb Detector Performance*, Int. J. Mod. Phys. **A30** (2015), no. 07 1530022, `arXiv:1412.6352`.

[56] R. Aaij *et al.*, *Performance of the LHCb Vertex Locator*, JINST **9** (2014) 09007, `arXiv:1405.7808`.

[57] P. Perret and X. Vilasis-Cardona, *Performance of the LHCb calorimeters during the period 2010-2012*, J. Phys. : Conf. Ser. **587** (2014) 012012. 6 p, see LHCb-TALK-2014-236.

[58] R. Aaij *et al.*, *The LHCb trigger and its performance in 2011*, JINST **8** (2013) P04022, `arXiv:1211.3055`.

[59] V. V. Gligorov and M. Williams, *Efficient, reliable and fast high-level triggering using a bonsai boosted decision tree*, JINST **8** (2013) P02013, `arXiv:1210.6861`.

[60] I. Bird, *Computing for the large hadron collider*, Annual Review of Nuclear and Particle Science **61** (2011), no. 1 99, `arXiv:https://doi.org/10.1146/annurev-nucl-102010-130059`.

[61] T. Sjöstrand, S. Mrenna, and P. Skands, *PYTHIA 6.4 physics and manual*, JHEP **05** (2006) 026, `arXiv:hep-ph/0603175`.

[62] T. Sjöstrand, S. Mrenna, and P. Skands, *A brief introduction to PYTHIA 8.1*, Comput. Phys. Commun. **178** (2008) 852, `arXiv:0710.3820`.

[63] Geant4 collaboration, S. Agostinelli *et al.*, *Geant4: A simulation toolkit*, Nucl. Instrum. Meth. **A506** (2003) 250.

[64] Geant4 collaboration, J. Allison *et al.*, *Geant4 developments and applications*, IEEE Trans. Nucl. Sci. **53** (2006) 270.

[65] L. Breiman, J. H. Friedman, R. A. Olshen, and C. J. Stone, *Classification and regression trees*, Wadsworth international group, Belmont, California, USA, 1984.

[66] B. P. Roe *et al.*, *Boosted decision trees as an alternative to artificial neural networks for particle identification*, Nucl. Instrum. Meth. **A543** (2005) 577, `arXiv:physics/0408124`.

[67] W. D. Hulsbergen, *Decay chain fitting with a Kalman filter*, Nucl. Instrum. Meth. **A552** (2005) 566, `arXiv:physics/0503191`.

[68] BaBar collaboration, P. del Amo Sanchez *et al.*, *Study of $B \to X\gamma$ decays and determination of $|V_{td}/V_{ts}|$*, Phys. Rev. **D82** (2010) 051101, `arXiv:1005.4087`.

[69] L. Anderlini *et al.*, *The PIDCalib package*, Tech. Rep. LHCb-PUB-2016-021. CERN-LHCb-PUB-2016-021, CERN, Geneva, Jul, 2016.

[70] J. Blatt and V. Weisskopf, *Theoretical nuclear physics*, Springer-Verlag New York (1979).

[71] S. U. Chung *et al.*, *Partial wave analysis in K-matrix formalism*, Annalen Phys. **4** (1995) 404.

[72] S. M. Flatte, *Coupled-Channel Analysis of the $\pi\eta$ and $K\overline{K}$ Systems Near $K\overline{K}$ Threshold*, Phys. Lett. **B63** (1976) 224.

[73] V. V. Anisovich and A. V. Sarantsev, *K-matrix analysis of the ($IJ^{PC} = 00^{++}$)-wave in the mass region below 1900 MeV*, Eur. Phys. J. **A16** (2003) 229, `arXiv:hep-ph/0204328`.

[74] S. Weinberg, *Pion scattering lengths*, Physical Review Letters **17** (1966) 616.

[75] FOCUS collaboration, J. M. Link *et al.*, *Dalitz plot analysis of the $D^+ \to K^-\pi^+\pi^+$ decay in the FOCUS experiment*, Phys. Lett. **B653** (2007) 1, `arXiv:0705.2248`.

[76] K. M. Watson, *The effect of final state interactions on reaction cross sections*, Phys. Rev. **88** (1952) 1163.

[77] B. S. Zou and D. V. Bugg, *Covariant tensor formalism for partial wave analyses of ψ decay to mesons*, Eur. Phys. J. **A16** (2003) 537, `arXiv:hep-ph/0211457`.

[78] Mark III collaboration, D. Coffman *et al.*, *Resonant substructure in $\overline{K}\pi\pi\pi$ decays of* D *mesons*, Phys. Rev. **D45** (1992) 2196.

[79] CLEO collaboration, M. Artuso *et al.*, *Amplitude analysis of $D^0 \to K^+K^-\pi^+\pi^-$*, Phys. Rev. **D85** (2012) 122002, `arXiv:1201.5716`.

[80] M. Nauenberg and A. Pais, *Woolly cusps*, Phys. Rev. **126** (1962) 360.

[81] CLEO collaboration, D. M. Asner *et al.*, *Hadronic structure in the decay $\tau^- \to \nu_\tau\pi^-\pi^0\pi^0$ and the sign of the tau neutrino helicity*, Phys. Rev. **D61** (1999) 012002.

[82] E791 collaboration, B. Meadows *et al.*, *Measurement of the $K^-\pi^+$ S-wave system in $D^+ \to K^-\pi^+\pi^+$ decays from Fermilab E791*, AIP Conf. Proc. **814** (2006) 675, `arXiv:hep-ex/0510045`.

[83] E791 collaboration, E. M. Aitala *et al.*, *Model independent measurement of S-wave $K^-\pi^+$ systems using $D^+ \to K\pi\pi$ decays from Fermilab E791*, Phys. Rev. **D73** (2006) 032004, `arXiv:hep-ex/0507099`, [Erratum: Phys. Rev. **D74** (2006) 059901].

[84] P. d'Argent *et al.*, *Amplitude analyses of $D^0 \to \pi^+\pi^-\pi^+\pi^-$ and $D^0 \to K^+K^-\pi^+\pi^-$ decays*, JHEP **05** (2017) 143, `arXiv:1703.08505`.

[85] BES III collaboration, M. Ablikim *et al.*, *Amplitude analysis of $D^0 \to K^-\pi^+\pi^+\pi^-$*, Phys. Rev. **D95** (2017) 072010, `arXiv:1701.08591`.

[86] FOCUS collaboration, J. M. Link *et al.*, *Study of the $D^0 \to \pi^-\pi^+\pi^-\pi^+$ decay*, Phys. Rev. D **75** (2007) 052003.

[87] Particle Data Group, J. Beringer *et al.*, *Review of particle physics*, Phys. Rev. **D86** (2012) 010001, and 2013 partial update for the 2014 edition.

[88] I. I. Bigi, *Charm physics: Like Botticelli in the Sistine chapel*, in *KAON2001: International Conference on CP Violation Pisa, Italy, June 12-17*, 2001. `arXiv:hep-ph/0107102`.

[89] D. Atwood and A. Soni, *Role of charm factory in extracting CKM phase information via $B \to DK$*, Phys. Rev. **D68** (2003) 033003, `arXiv:hep-ph/0304085`.